The University of Nottingham

University Park, NG7 2RD

Nottingham, United Kingdom



UNITED KINGDOM · CHINA · MALAYSIA

Explorative methods for turbulent flow control

Alessio Basso, MEng., MRes.

Thesis submitted to the University of Nottingham for the degree of Master of Philosophy

Supervisors: Prof Choi Kwing-So, Prof Zanchetta Pericle, Prof Morvan Hervé

February 2018

Abstract

Turbulent skin-friction is a matter of importance for the aerospace sector, where the increase in fuel costs is of concern. In view of this consideration, the aircraft aerodynamic efficiency can be increased by reducing turbulent drag. In fact, turbulent drag can up to 45% of the total drag force encountered in subsonic commercial transportation. Four different concepts have been relevant over the last few decades to achieve turbulent skin-friction reduction:

- Fluid suction;
- Tangential gas injections;
- Particle additives applied to main flow stream;
- Compliant walls.

However, all the above methods result in a delay of the turbulence transition point, rather than a disruption of the turbulence self-sustenance mechanism.

Outer coherent motions, often identified in so-called hairpin vortices, are profoundly correlated with the dynamics of turbulence. Therefore, their actuation is considered as a valid approach to interrupt the near-wall cycle and reduce the associated friction drag.
On the basis of the above considerations, the project presented in this dissertation proposes an innovative flow actuator for active control

of turbulent skin friction for subsonic regimes. The key features for this flow actuator are:

1. **A real-time identification of hairpin eddies directly from the near-wall region.** This idea is crucial when considering direct intervention of hairpin eddies as the key method for turbulence control;

2. **Disruption of coherent motions.** Actuators should have a fast response to disrupt hairpins within their persistence time interval;

3. **Response adjustment in real time.** This is to effectively reduce turbulent drag by continuously monitoring the near-wall signal.

In addition, in the specific case of flow control on aircraft wings, the flow actuator should not modify the surface smoothness and aerodynamic.

Therefore, the present work has explored two different methodologies which can be combined together to achieve turbulent skin-friction reduction:

(a) **An approach making use of image processing and pattern recognition to identify outer coherent motions directly from the near-wall region.** This method is interesting, especially for flow control on aircraft wings where hairpin footprints can be read at the wall without affecting the wing aerodynamic shape;

(b) **The use of laser energy deposition (LED) to induce a local remote flow perturbation.** Laser energy deposition

is convenient, especially because of its fast response. Moreover, since no mechanical components are required, the dynamic response of the boundary layer can be shorter than conventional actuators.

In the perspective of producing persistent perturbations which can interfere with hairpin vortices, laser energy deposition is used here to to trigger the ignition of flammable bubbles and the sublimation of carbon-dioxide particles. Particle image velocimetry (PIV) in quiescent air has been performed to measure the effects induced by laser energy deposition. Ignition of bubbles filled with flamable mixtures is found interesting in this work due to the fast and intense jets produced.

Developments presented in this dissertation provide the ground work to develop an active-feedback actuator which can monitor and disrupt the turbulence near-wall cycle, by manipulating outer coherent motions. This technology is helpful to reduce turbulent skin friction on aircraft wings in subsonic transportation.

List of publications

1. **A. Basso, N. Rkiouak and K.-S. Choi,** *On the relation between near-wall skin friction and large-scale coherent motions in turbulent boundary layers.* European Drag Reduction and Flow Control Meeting - EDRFCM 2015, March 23-26, 2015, Cambridge, UK.

Acknowledgments

This work has been funded by the European Commission under the project titled INNOVATE, The systematic Integration of Novel Aerospace Technologies, FP7 project number 608322 which is part of the FP7-PEOPLE-2013-ITN call.

I am grateful to my supervisors for their insights in this research. I would like to thank my wife Kuemju and my family for the support during my study.

Finally, special thanks to my best friends during this three-year long journey: Dr Zaid Janjua, Mr Paul Connolly, Dr Faycal Bahri, Dr Jung-Hoon Kim, Mr Arnold Cheung and Mr Navid Freidoonimehr and the whole INNOVATE Team.

Contents

List of Figures **xi**

List of Tables **xix**

List of Symbols **xx**

1 Motivations and objectives **1**

1.1 Introduction 1

1.2 The role of hairpin eddies in the production of turbulent skin friction 4

1.3 Project Objectives 4

2 Literature review **7**

2.1 Introduction 7

2.2 Description of turbulent boundary layers 9

2.2.1 The near-wall cycle 9

2.2.2 The Logarithmic and Outer Regions 15

2.2.3 Correlation between Inner and Outer Regions 27

2.3 Remote Flow Control 31

2.3.1 Introduction 31

2.3.2 Localised Flow Control by Laser Energy Deposition 34

2.4 Summary 42

3 Recognition of coherent motions by image analysis 45

3.1 Introduction 45

3.2 Image analysis applied to turbulent flows 47

3.2.1 Introduction 47

3.2.2 Median filtering 51

3.2.3 Conversion to Binary Format 53

3.2.4 Binary Morphological Processing 56

3.3 Near-wall regions of interest 59

3.3.1 Introduction 59

3.3.2 Results 60

3.4 Object recognition 61

3.4.1 Introduction 61

3.4.2 Results 62

3.5 Analysis of high-speed motions 65

3.5.1 Introduction 65

3.5.2 Binary Image Processing 66

3.5.3 Two-dimensional image correlation 67

3.6 Summary 69

4 Remote flow control by laser energy deposition 71

4.1 Introduction 71

4.2 Particle image velocimetry 74

4.2.1 Introduction 74

4.2.2 Description of fluid motion 75

4.2.3 PIV parameters 76

4.2.4 Analysis, validation and processing 80

4.3 Laser energy deposition in quiescent air - experimental setup 82

4.3.1 Introduction 82

4.3.2 Setup 83
4.3.3 Time synchronisation 85
4.4 Evolution on time for ignition 88
4.4.1 Introduction 88
4.4.2 Progression of ignition processes 89
4.5 Quantification of LED-induced flow perturbations . . 94
4.5.1 Introduction 94
4.5.2 Air-hydrogen bubbles 96
4.5.3 Air-butane bubbles 100
4.5.4 Sublimation of carbon-dioxide particles . . . 103
4.6 Summary 107

5 Conclusions and future developments **109**
5.1 Concluding remarks 109
5.2 Recommendations for future research 111

Appendices **113**

A Appendix **115**
A.1 Identification of Outer Coherent Motions through Image Processing 115
A.1.1 Binary Morphological Processing 115
A.1.2 Identification of Near-wall Regions of Interest (ROI) 118
A.1.3 Object Recognition in the Logarithmic and Outer Regions 120

References **123**

List of Figures

1.1.1 Skin-friction drag on a wing section. `https://www.skybrary.aero/index.php/Friction_Drag`. 1

1.1.2 Components of parasitic drag for a large commercial aircraft in subsonic regime, `https://goo.gl/VDMVYe`. Source: NATO AGARD. 3

2.2.1 Near-wall streaks across a flat-plate boundary layer - top view (wall-parallel planes). y^+ =2.7 (a), 9.6 (b), 38.0 (c), 82.0 (d) [Kline et al., 1967]. 10

2.2.2 Ideal model of formation of stream-wise counter-rotating vortices [Blackwelder and Eckelmann, 1979]. 11

2.2.3 Physical mechanism for formation of near-wall streaks [Kline et al., 1967]. 11

2.2.4 Sketch of stream-wise counter-rotating vortices and lift-up of streaks and momentum-deficit regions [Blackwelder and Eckelmann, 1979]. 12

2.2.5 Mean value of the streak transverse spacing. Dashed lines indicate a margin equal to $\pm 2\sigma$ [Smith and Metzler, 1983, Schraub and Kline, 1965, Oldaker and Tiederman, 1977, Gupta et al., 1971, Lee et al., 1974, Nakagawa and Nezu, 1981]. 13

2.2.6 Model of inflection of stream-wise velocity profiles due to streak breakup (a) [Kim et al., 1971]. 14

2.2.7 Time interval between consecutive bursts in a flat-plate flow [Runstadler et al., 1963, Schraub and Kline, 1965, Kim et al., 1971]. 14

2.2.8 Top view of isosurfaces of stream-wise vorticity (a); contours of conditionally-averaged, stream-wise vorticity (b) [Kravchenko et al., 1993]. 15

2.2.9 Maps of stream-wise velocity in a plane at $y^+ = 30$. Maps before (a) and after streak filtering (b). Time evolution of the skin friction for channel flow (c); streak-unfiltered (solid line), and streak-filtered wall (dashed line). The initial conditions is a fully developed channel at $Re_\tau = 190$ [Jimenez and Pinelli, 1999]. 16

2.2.10 Geometrical configuration and nomenclature for hairpin structures at different Reynolds numbers [Head and Bandyopadhyay, 1981]. 18

2.2.11 Inclination angle of hairpin structures with Reynolds number. Flow visualisation on a zero-pressure gradient boundary layer. $Re_\theta = 7485$ (a), and 14500 (b) [Bandyopadhyay, 1980]. 18

2.2.12 Hairpin eddies in reattaching flow past circular rod: general (a), and cross-stream (b) illumination [Head and Bandyopadhyay, 1981]. 19

2.2.13 (a) Model for a three-dimensional vortex structure, [Theodorsen, 1952]; (b) Vortex-line model in the near-wall region [Willmarth and Tu, 1967]. 19

2.2.14 Hairpin formation, stretching, and interaction with the near-wall region [Smith, 1984]. 19

2.2.15 Model of interaction of three-dimensional vortex structures with the near-wall region. Time evolution from top to bottom [Praturi and Brodkey, 1978]. 21

2.2.16 Sketch of the cycle of formation and re-generation of hairpin vortices [Choi, 1989]. 22

2.2.17 Formation of a secondary hairpin vortex (SHV) from a primary structure (PHV). Contours of enstropy λ_{ci}^2. Time varies from $t^+ = tu^2/\nu$ =63 (a), 72 (b), 81 (c), 117 (d). DNS simulation of channel flow at $Re_\tau = 180$ [Zhou et al., 1999]. 24

2.2.18 Hairpin signature is accompanied by negative Reynolds stress ($-\overline{uv}$) resulting from intermittent events in the second and fourth quadrant of the u-v plane (a); sketch of hairpin signature (b) and (c) [Adrian, 2007]. 25

2.2.19 Model of interaction between hairpin packets and regions of momentum-deficit [Adrian, 2007]. 25

2.2.20 Signature of hairpin packets from a PIV measurement. Wall-normal, longitudinal plane of velocity data in a turbulent boundary layer at $Re_\tau = 930$. Uniform regions of momentum are labeled as I, II, III respectively [Adrian et al., 2000]. 26

2.2.21 Pre-multiplied energy spectra of stream-wise velocity fluctuations. $Re_\tau = 180$ (a), 395 (b), 640 (c) [Abe et al., 2004]. 28

2.2.22 Contour maps of pre-multiplied energy spectra of stream-wise velocity fluctuations. Re_τ = 1010 (a); 1910 (b); 2630 (c); 7300 (d) [Hutchins and Marusic, 2007a]. 29

2.2.23 Calculation of the superposition coefficient and inclination angle of outer coherent motions, through cross-correlation function [Mathis et al., 2011a]. . . . 30

2.3.1 Three-dimensional image produced as LED-induced air breakdown. Light points are where air is ionised to form plasma [Tilma, 2006]. 35

2.3.2 Control of the Edney IV interaction in front of a sphere at M_∞ = 3.45. Time evolution at: $0\mu s$ (a); $10\mu s$ (b); $20\mu s$ (c); $30\mu s$ (d); $50\mu s$ (e); $70\mu s$ (f) from the triggering laser pulse [Adelgren et al., 2005]. 36

2.3.3 History of stagnation pressure at 1.0 diameters upstream of the sperical model [Adelgren et al., 2005]. . 37

2.3.4 Phase-average Schlieren visualisation of the interaction between a blast shock produced through lased energy deposition and the normal shock train in a compression inlet; M_∞ = 2.0. Time evolution at: (a) $10\mu s$; (b) $40\mu s$; (c) $80\mu s$; (d) $200\mu s$ from the triggering laser pulse [Knight and Yan, 2007]. 38

2.3.5 Evolution of plasma roll-up. $\hat{t} = t/t^*$ = 0.36 (a); 0.54 (b); 0.72 (c); 0.90 (d); 0.126 (e); 1.80 (f). t^* = 15.9μs, based on measurement of the sound speed [Ghosh and Mahesh, 2008]. 39

2.3.6 A blast shock wave induced by LED. Pressure contours at $\hat{t} = t/t^*$ =0.0 (a), 0.04 (b), 0.36 (c), 0.99 (d) [Ghosh and Mahesh, 2008]. 40

2.3.7 Flow shadowgraph (left) and numerical simulation - density gradients (rigth) of blast-shock interaction over a blunt body at $M_\infty = 2$. Snapshots at t= 30 (a), 97 (b), 130 (c), 163 (d), 297 (e) μs from the laser pulse [Schulein and Zheltovodov., 2008]. 41

3.2.1 Schematic of the principle of median filtering. `https://goo.gl/qbSaq8`. 52

3.2.2 Stream-wise velocity fluctuations at $y^+ = 1.4$. $Re_\tau = 1025$. Original DNS data (a); median filtered data (b). Filter size, $\lambda_x^+ \times \lambda_z^+ \approx 700 \times 60$. 53

3.2.3 Conversion of stream-wise velocity fluctuations into binary format at $y^+ = 1.4$ (a, b), 49.7 (c, d), 180.0 (e, f). $Re_\tau = 1025$. 55

3.2.4 Morphological Image Processing. Original and processed image pairs, $y^+ = 1.4$ (a, b), 13.5 (b, c), 49.7 (d, e), 180.0 (f, g). $Re_\tau = 1025$. 57

3.2.5 Morphological Image Processing. Original and processed image pairs, $y^+ = 2.0$ (a, b), 30.0 (c, d), 120.0 (e, f), 400.0 (g, h). $Re_\tau = 1600$. 58

3.3.1 Identification of near-wall hairpin imprints. Original velocity fluctuations (a), and processed binary samples (b) at $y^+ = 1.4$. $Re_\tau = 1025$. 60

3.3.2 Identification of near-wall hairpin imprints. Original velocity fluctuation (a), and processed binary samples (b), $y^+ = 2.0$. $Re_\tau = 1600$. 60

3.4.1 Object recognition. Near-wall samples at $y^+ = 1.4$ (a); Two-dimensional correlation at $y^+ = 13.5$ (b), 49.7 (c), and 180.0 (d). $Re_\tau = 1025$. 63

3.4.2 Object recognition. Near-wall samples at $y^+ = 2.0$ (a); Two-dimensional correlation at $y^+ = 60.0$ (b), 120.0 (c), and 200.0 (d). $Re_\tau = 1600$. 64

3.5.1 Image analysis for high-speed motions. Unprocessed binary image (a) and processed with removal of skeletonisation and branching (b) at $y^+ = 1.4$. $Re_\tau = 1025$. 66

3.5.2 Image analysis for high-speed motions. Unprocessed binary image (a) and processed image (with removal of skeletonisation and branching) (b) at $y^+ = 2.0$. $Re_\tau = 1600$. 67

3.5.3 Object recognition for high-speed motions. Near-wall sampling at $y^+ = 1.4$ (a) and object recognition at $y^+ = 13.5$ (b), 49.7 (c), 180.0 (d). $Re_\tau = 1025$. 68

4.1.1 Sketch of a potential application of a energy deposition in aviation. 73

4.2.1 General PIV setup in a wind tunnel. [Grant, 1997]. . 75

4.2.2 Lagrangian (a) and Eulerian (b) descriptions. 76

4.2.3 Resolution (a) and interrogation (b) cells, [Grant, 1997]. 77

4.2.4 Cross-correlation performed by convolution(a) and FFT(b) approaches [Stamhuis, 2006]. 81

4.3.1 Experimental setup for laser energy deposition in quiescent air. 84

4.3.2 Synchronisation of the PIV system with the pulsed laser for flow control. 87

4.4.1 LED-induced ignition of static butane bubbles. $t = 0$ (a), 15 (b), 21 (c), 35 (d), 65 (e), 90 (f), 140 (g), 205 (h), 220 (i), 260 (j) milliseconds. Acquisition rate: 1kHz. 90

4.4.2 LED-induced ignition of static air-hydrogen bubbles. $t = 0$ (a), 1.4 (b), 1.8 (c), 3.8 (d), 5.4 (e), 6.2 (f), 8.0 (g), 12.0 (h), 14.0 (i), 20.0 (j) milliseconds. Aquisition rate equal to 5 kHz. 92

4.5.1 LED-induced bursting of hydrogen bubbles. t= 0.0 (a), 2.0 (b), 3.0 (c), 11.5 (d), 13.0 (e), 16.5 (f), 17.0 (g), 18.0 (h), 18.5 (i), 20.0 (j) milliseconds. Acquisition rate equal to 2 kHz. 97

4.5.2 LED-induced bursting of hydrogen bubbles. Snapshots of instantaneous horizontal (left) and vertical (right) velocity components. t= 0 (a, b), 2.5 (c, d), 5.0 (e, f), 7.5 (g, h) milliseconds. 99

4.5.3 LED-induced ignition of air-butane bubbles. Flow visualisation. t=0.0 (a), 12.5 (b), 25.0 (c), 37.5 (d), 50.0 (e), 62.5 (f), 75.0 (g), 87.5 (h) milliseconds. . . . 101

4.5.4 LED-induced ignition of butane bubbles. Snapshots of instantaneous horizontal (left) and vertical (right) velocity. t = 20.0 (a, b), 40.0 (c, d), 65.0 (e, f), 85.0 (g, h) milliseconds. 102

4.5.5 LED-induced sublimation of CO_2 ice. t = 0.0 (a), 5.0 (b), 15.0 (c), 25.0 (d), 40.0 (e), 45.0 (f) milliseconds. Aquisition rate: 1kHz. 104

4.5.6 LED-induced sublimation of dry ice. Snapshots of instantaneous horizontal (left) and vertical (right) velocity. t = 0.0 (a, b), 10.0 (c, d), 20.0 (e, f), 30.0 (g, h) milliseconds. 105
4.5.7 LED-induced sublimation of dry ice. Snapshots of instantaneous vorticity maps. t = 0.0 (a), 10.0 (b), 20.0 (c), 30.0 (d) milliseconds. 106

List of Tables

3.1 DNS datasets used to develop a new methodology for recognition of outer coherent motions. Dataset no. 1 from IC London [Agostini and Leschziner, 2014, Agostini et al., 2014a]; dataset no. 2 from Warwick University, [Hurst et al., 2014]. 47

List of Symbols

Acronyms

AM	Amplitude modulation
CLT	Central limit theorem
DBD	Dielectric barrier discharge (Plasma actuator)
DNS	Direct numerical simulation
EMD	Empirical mode decomposition
FFT	Fast fourier transform
FM	Frequency modulation
GMM	Gaussian mixture models
HPIV	Holographic particle image velocimetry
IA	Interrogation area
LED	Laser energy deposition
LSM	Large scale motions
M_s	Mach number of shock wave
NOD	Number of objects detected
PDF	Probability density function
PIV	Particle image velocimetry
POD	Proper orthogonal decomposition
PSJ	Plasma synthetic jets
RFD	Roughness fractal dimension
ROI	Regions of interest
SE	Standard error
SPIV	Stereoscopic particle image velocimetry
SJ	Synthetic jets
SNR	Signal-to-noise ratio
UV	Ultra-violet
VLSM	Very large scale motions

Roman symbols

δ	Displacement thickness
$\delta_v = \nu/u_\tau$	Viscous length
Δt_p	Persistence time of streaks
Δx^+	Non-dimensional longitudinal extension of streaks
$\lambda^+ = \lambda u_\tau/\nu$	Transverse streak spacing
$\lambda_x^+ = \lambda_x u_\tau/\nu$	Longitudinal streak extension
$\lambda_z^+ = \lambda_x u_\tau/\nu$	Transverse streak extension
ν	Kinematic Viscosity $[m^2/s]$
$Re_\tau = hu_\tau/\nu$	Reynolds number based on the channel half-height
$Re_\theta = u\theta/\nu$	Reynolds number based on the momentum thickness
$\tau_l = \mu\partial u/\partial y$	Laminar shear stress
$\tau_t = -\rho\overline{u'v'}$	Turbulent shear stress
θ	Momentum thickness
$\overline{T_B}$	Non-dimensional bursting time
$u^+ = u/u_\tau$	Non-dimensional stream-wise velocity fluctuation
$u_\tau = \sqrt{\tau_w/\rho}$	Friction velocity
u_L^+	Longitudinal velocity fluctuation of large-scale motions
$y^+ = yu_\tau/\nu$	Distance from the wall of a turbulent flow

Chapter 1

Motivations and objectives

1.1 Introduction

Aerodynamic drag has been one of the most intriguing problems in Fluid Mechanics over the last decades, especially for air transportation. When an object travels in a viscous fluid (e.g. air) it can encounter a resistance action opposing its motion, as a result of the formation of a *turbulent boundary layer*. This *fluid reaction* is proportional to the surface area in consideration, the square of free-stream velocity and the surface roughness. Viscous actions can delay the motion of fluid particles near the wall, for example the wet surface of aircraft (Fig. 1.1.1).

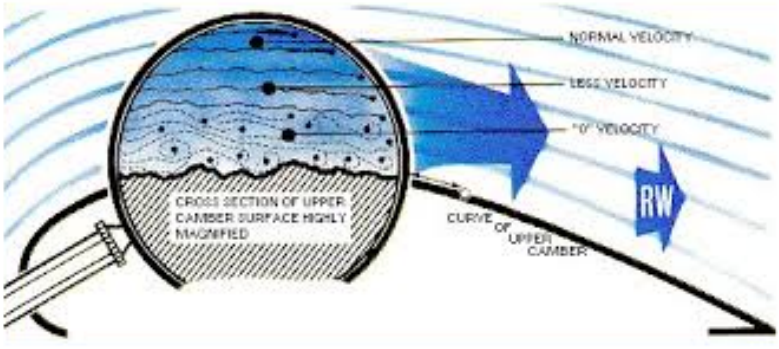


Figure 1.1.1: Skin-friction drag on a wing section. `https://www.skybrary.aero/index.php/Friction_Drag`.

In the case of airplanes, the main force components in straight-uniform horizontal flight are:

- *Weight,* which is due to Earth's gravitational field;
- *Aerodynamic lift,* is produced essentially by wings, which can deflect the airflow and produce unbalance between pressure distributions on the upper and lower surfaces;
- *Aerodynamic Drag,* which mainly results from fluid viscosity;
- *Thrust,* which is provided by engines, through propellers or jets, to counteract the overall drag.

Aerodynamic drag has also its own contributions, which are listed below:

1. **Form or Pressure Drag,** which is due to pressure distributions associated with separation of the turbulent boundary layer from the aircraft surface. This contribution depends on the overall aircraft shape, including wings, fuselage, tails, landing gears, etc.;
2. **Interference Drag,** which occurs especially at the junctions between fuselage and wings or fuselage and tails, or wings and engine pylons, etc.;
3. **Skin-friction Drag,** produced by a turbulent boundary layer developing over the whole aircraft *wet* surface. This component is generated by the velocity difference, hence friction, between the aircraft surface and surrounding airflow;
4. **Roughness Drag,** which is due to the material roughness and other manufacturing imperfections, e.g. the step between panels on wing surfaces.

The above items are part of the so-called *Parasitic Drag*. By contrast *Lift-induced Drag* is related to the circulation on aircraft wings, particularly an airflow downwash which produces an additional force component in opposite direction to the free-stream wind.

Turbulent skin friction is the largest contribution encountered by aircraft. Recent studies[1] have demonstrated that turbulent drag can amount to 45% or more of the overall resistance in subsonic air transportation (Fig. 1.1.2). This result means that aircraft normally consume a significant percent of fuel to only counteract turbulence.

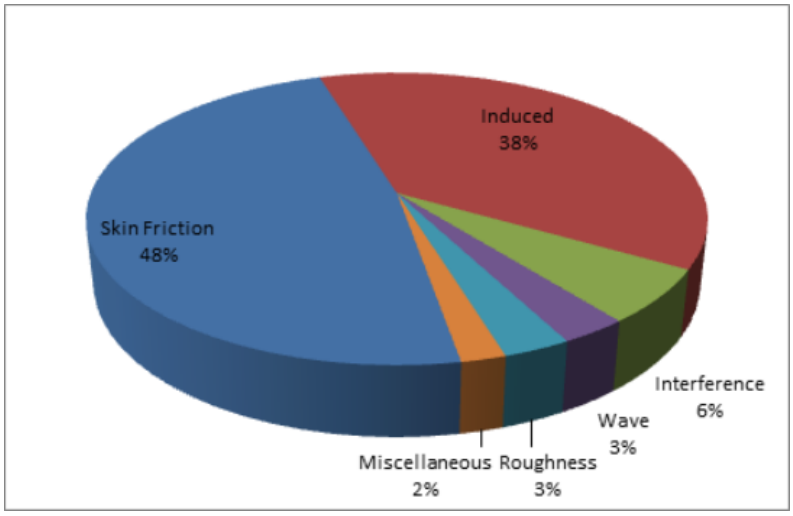


Figure 1.1.2: Components of parasitic drag for a large commercial aircraft in subsonic regime, `https://goo.gl/VDMVYe`. Source: NATO AGARD.

Furthermore, a recent increase in fuel costs has induced deep concerns about how to reduce the aerodynamic losses, save fuel and reduce noise. Some solutions have looked at delaying the transition to turbulent flows by reducing the surface roughness and by keeping the aircraft clean from any airborne particles, especially dust. By contrast, there is a growing interest in disrupting the physical mechanism responsible for high levels of turbulent drag.

[1] `https://www.sto.nato.int/Pages/agard-history.aspx`.

1.2 The role of hairpin eddies in the production of turbulent skin friction

In the context of turbulent skin-friction reduction, hairpin vortices have attracted the attention of research, due to their involvement in the *near-wall cycle*, responsible for the turbulence self-sustenance. Direct numerical simulations (DNS) and experimental measurements have identified hairpins characteristic signature and have reinforced the idea of an inner-outer correlation. Hairpin vortices are *coherent motions* in the sense that they can persist for sufficient time to affect flow statistics. In this perspective, hairpins can be exploited to disturb the physical mechanism inducing high skin friction at the wall.

1.3 Project Objectives

For the reasons explained in Sect. 1.2, the work presented in this dissertation is aimed at developing a novel flow actuator which can reduce turbulent skin friction in a subsonic flow through real-time identification and direct intervention of hairpin vortices. The flow actuator should be able to:

(a) **Identify outer coherent motions in real-time by making use of the near-wall information.** Image processing and pattern recognition are valid candidates for real-time identification of hairpin eddies;

(b) **Produce a localised flow perturbation which can disrupt hairpin vortices, without affecting the surrounding flow field.** Laser energy deposition (LED) is the most

convenient choice due to its fast response, ease of installation on a wing surface and the fact that it does not require any configuration which can perturb the flow field. For example, in the specific case of aircraft wings, laser beams can be fired directly from the wall and focalised on hairpin vortices above the boundary layer.

A combined implementation of the methods above can be the ground for an active-feedback actuator which can adjust its action, i.e. location and intensity of laser spots, by continuously monitoring the dynamic response of the turbulent boundary layer.

Chapter 2

Literature review

2.1 Introduction

Turbulence remains one of the most intriguing problems in physics. It is well known that the kinetic energy of free-stream flows can be converted into velocity fluctuations through turbulence. In this process of momentum-transfer, kinetic energy is conveyed from large to small scales of fluctuation, down to the Kolmogorov's length, where energy is dissipated by fluid viscosity. This self-sustained process is primarily induced by the *wall no-slip condition*, which applies to viscous flows.

Coherent motions, especially hairpin eddies, play a key role in the cycle of production and dissipation of turbulence. Their persistence through the boundary layer has been proved by flow visualisation [Kline et al., 1967, Corino and Brodkey, 1969, Head and Bandyopadhyay, 1981, Smith and Metzler, 1983, Kim et al., 1971], hot-wire measurements [Blackwelder and Eckelmann, 1979, Choi, 1989, Wallace et al., 1972] and numerical simulations [Kim, 1983, Del Alamo and Jimenez, 2003, Jimenez et al., 2004]. As suggested by Choi [Choi,

1989], hairpin vortices can control the near-wall cycle, especially the turbulence production, *bursting* and wall shear stress. Furthermore, their energetic signature and influence on the near-wall region has been demonstrated through the discovery of a second peak in the pre-multiplied energy spectra of stream-wise velocity fluctuations [Hutchins and Marusic, 2007a, Hutchins and Marusic, 2007b]. As a result of all these observations, a model has been built [Mathis et al., 2009, Mathis et al., 2011a, Mathis et al., 2011b] to reconstruct the inner shear stress from measurements of velocity fluctuation in the logarithmic region.

Therefore, it is fundamental to disrupt outer coherent motions to control skin friction. An ideal actuator should have the following characteristics:

(a) A fast real-time response to flow changes. This is fundamental since coherent motions can appear, disappear or be convected down-stream over time;

(b) The ability to produce a local perturbation. Hairpin loops can be disrupted through their heads;

(c) Be implementable for active feed-back control. In other words, the action of the flow actuator should be adjusted in real time by monitoring the near-wall shear stress distribution.

Such a system can be applied to aircraft wings where turbulent skin friction can be equal to 45% of the total drag force. For this purpose, a real-time system can predict and destroy hairpin eddies, while the turbulence near-wall cycle can be temporarily interrupted.

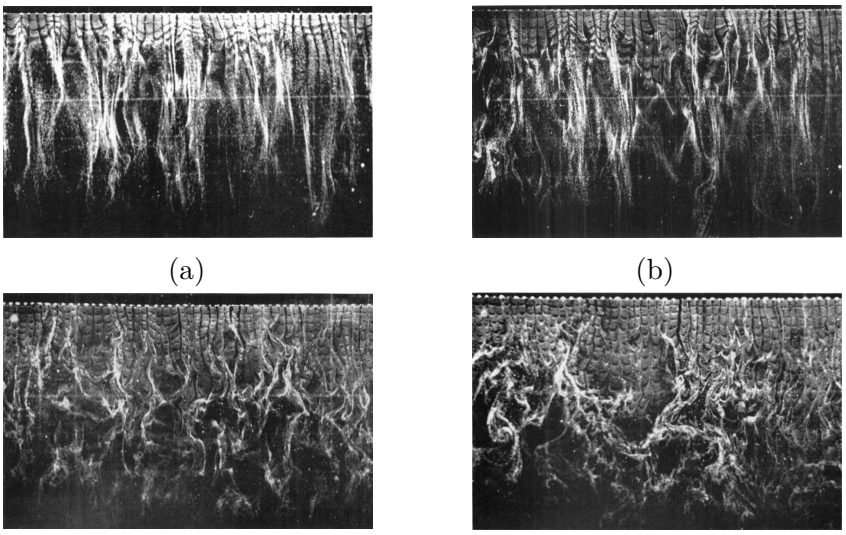
This chapter will provide a detailed description of the near-wall cycle and the involvment of outer coherent motions (Sect. 2.2).

Moreover, Sect. 2.3 will present some flow control applications which have been the starting point for the development of the present work.

2.2 Description of turbulent boundary layers

2.2.1 The near-wall cycle

The turbulence near-wall cycle has been described through a physical mechanism involving long meandering regions of stream-wise momentum deficit named *streaks*. Streaks have been observed in turbulent channels, flat-plate and pipe flows. One of the pioneering investigations has been the hydrogen-bubble visualisation by Kline [Kline et al., 1967], which has proved the existence of long streaky filaments of fluid originating from the distortion of the wall mean-shear stress. These motions are time-persistent, as they can continuously regenerate where previous streaks have disappeared. Streaks are ordered flow structures in the viscous sublayer, where viscosity is dominant over inertial effects. However, they can become chaotic away from the wall, in the buffer and logarithmic regions (Fig. 2.2.1). An explanation for the formation of near-wall streaks has firstly been proposed [Lighthill, 1963] through a three-dimensional mechanism that can induce quasi-periodic inwards and outwards motions, and span-wise vorticity. In fact, when flow is directed towards the wall, span-wise vortex lines are stretched; whereas outwards motions induce transversal compression. Eventually, stretching and compression of vortex lines can cause span-wise gradients of velocity components and the formation of pairs of longitudinal counter-rotating vortices



(a) (b) (c) (d)

Figure 2.2.1: Near-wall streaks across a flat-plate boundary layer - top view (wall-parallel planes). y^+ =2.7 (a), 9.6 (b), 38.0 (c), 82.0 (d) [Kline et al., 1967].

(Fig. 2.2.2). These vortices can pump low-speed fluid away from the viscous sub-layer (Figs. 2.2.3 and 2.2.4). A peculiar feature of streaks is their span-wise spacing, which seems to assume a constant value independent from Reynolds number. To support this idea, Smith and Metzler [Smith and Metzler, 1983] compared results from several studies at different Reynolds numbers (Fig. 2.2.5). They have concluded that the mean value of the streaks transversal spacing is equal to $\overline{\lambda^+} = \bar{\lambda} u_\tau/\nu \approx 100 \pm 20$, being $u_\tau = \sqrt{\tau_w/\rho}$ the friction velocity and ν the kinematic viscosity. $\overline{\lambda^+}$ is nearly constant in the viscous sublayer, whereas it increases above $y^+ = 5.0$ and tends to the asymptotic value of $\overline{\lambda^+} \approx 2y^+$, for $y^+ > 100$ [Nakagawa and Nezu, 1981]. This trend might be related to intermittent merging and disconnection between pairs of existing streaks. Streaks can be persitent for long time (e.g. $\Delta t_p^+ = \Delta t_p u_\tau^2/\nu \approx 485 - 2500$ at $Re_\theta = u\theta/\nu = 1490$[1] [Smith and Metzler, 1983]). As a result, low-

[1] θ is the momentum thichness of the boundary layer.

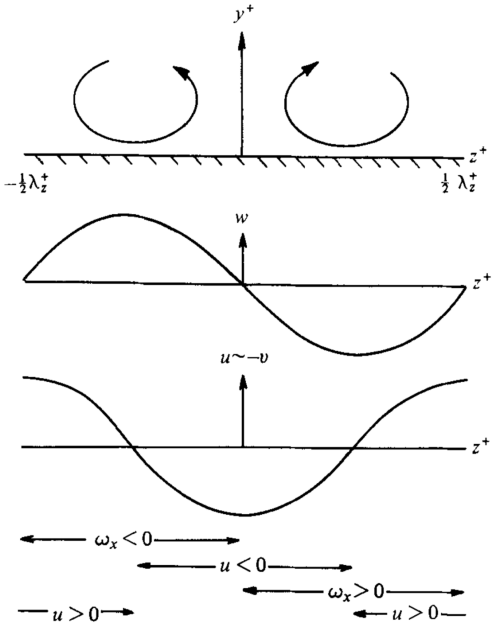


Figure 2.2.2: Ideal model of formation of stream-wise counter-rotating vortices [Blackwelder and Eckelmann, 1979].

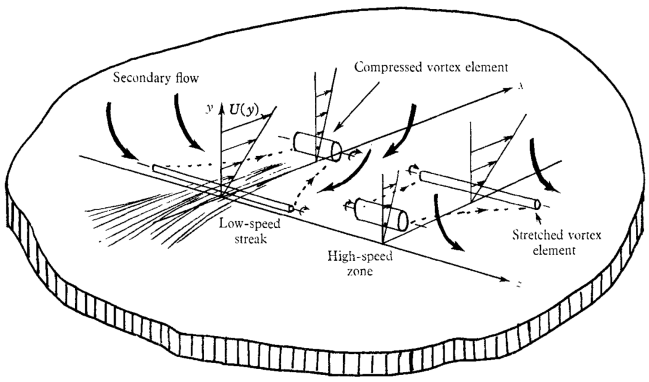


Figure 2.2.3: Physical mechanism for formation of near-wall streaks [Kline et al., 1967].

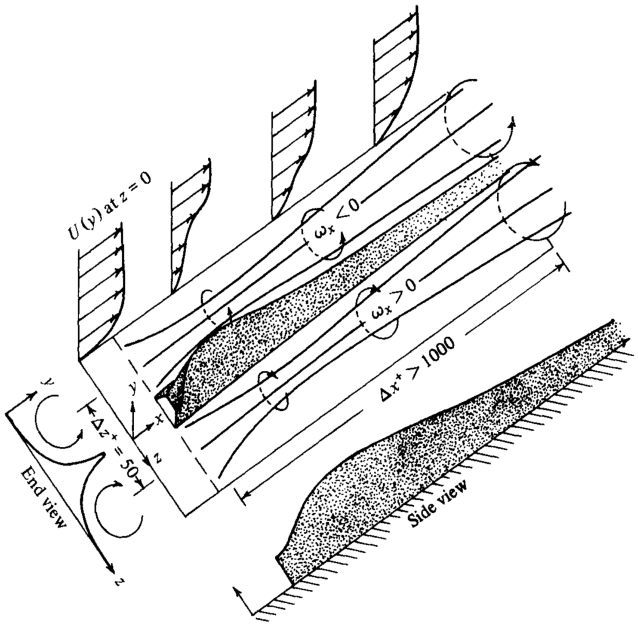


Figure 2.2.4: Sketch of stream-wise counter-rotating vortices and lift-up of streaks and momentum-deficit regions [Blackwelder and Eckelmann, 1979].

speed regions of fluid have been observed to extend longitudinally for several thousands of wall units ($\Delta x^+ > 1000$, [Blackwelder and Eckelmann, 1979, Kreplin and Eckelmann, 1979, Oldaker and Tiederman, 1977]). These results are also confirmed by DNS data of turbulent channels [Jimenez et al., 2004].

Streaks are important for turbulence self-sustainment and momentum transfer between inner and outer regions. In support of this thesis, Kline and later Kim [Kline et al., 1967, Kim et al., 1971] have observed a streak cycle, named *bursting*. Streak bursting is described in the following sequence:

1. **Streak are lifted up away from the wall and are convected down-stream, due to stream-wise, counter-rotating vortices;**

2. **Streak oscillate at a specific distance from the wall**

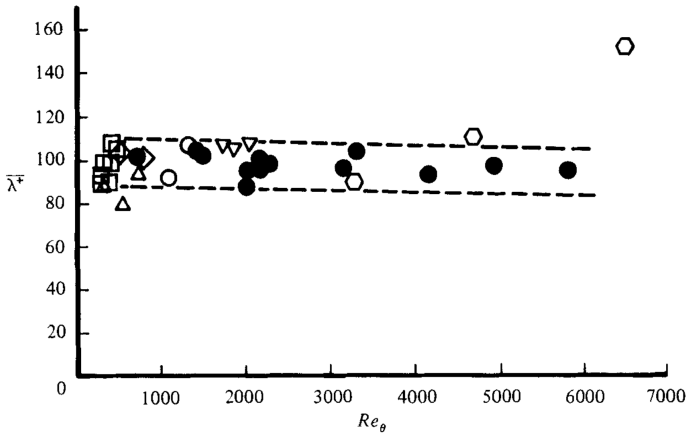


Figure 2.2.5: Mean value of the streak transverse spacing. Dashed lines indicate a margin equal to $\pm 2\sigma$ [Smith and Metzler, 1983, Schraub and Kline, 1965, Oldaker and Tiederman, 1977, Gupta et al., 1971, Lee et al., 1974, Nakagawa and Nezu, 1981].

$(8 < y^+ < 13)$**.** This occurrence is due to the interaction with regions of high momentum. Oscillations are amplified in the buffer region at $10 < y^+ < 30$;

3. **Streak break-up.** Normally, break-up occurs after 3-10 cycles due to wave-number transfer, and consists of violent eruptions of fluid.

As a result of streak break-up, low-speed fluid is ejected towards the outer region. By contrast, high-speed regions are impinged on the wall, producing high shear stress. For these reasons, streak break-up is believed to be the key mechanism for production and maintenance of turbulence [Runstadler et al., 1963].

In the same way, through a combination of hydrogen-bubble visualisation and constant temperature anemometry (CTA) in open-channel flow, Kim [Kim et al., 1971] has noticed that streak lifting and break-up are the symptom of inflection of instantaneous profiles of stream-wise velocity (Figs. 2.2.6). Auto-correlation measurements

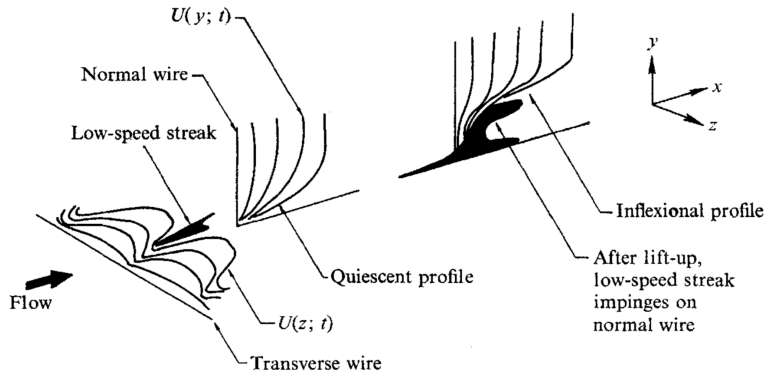


Figure 2.2.6: Model of inflection of stream-wise velocity profiles due to streak breakup (a) [Kim et al., 1971].

[Runstadler et al., 1963, Schraub and Kline, 1965, Kim et al., 1971] have suggested a link between the mean time interval between consecutive bursts, namely $\overline{T_B}$, and the friction velocity, $u_\tau = \sqrt{\tau/\rho}$ (Fig. 2.2.7). All the above considerations support the idea that streak break-up can affect skin friction through large fluid inrushes named as *sweeps*.

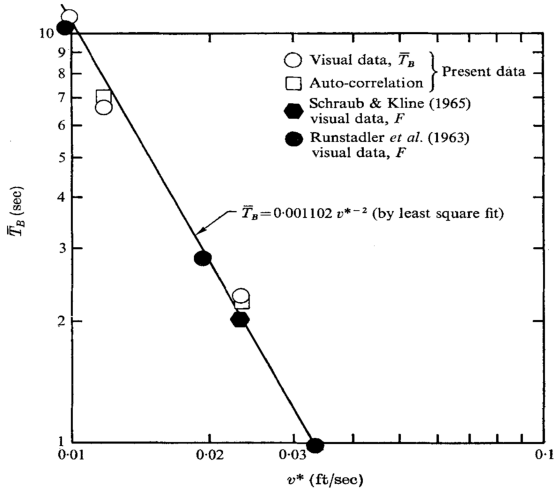
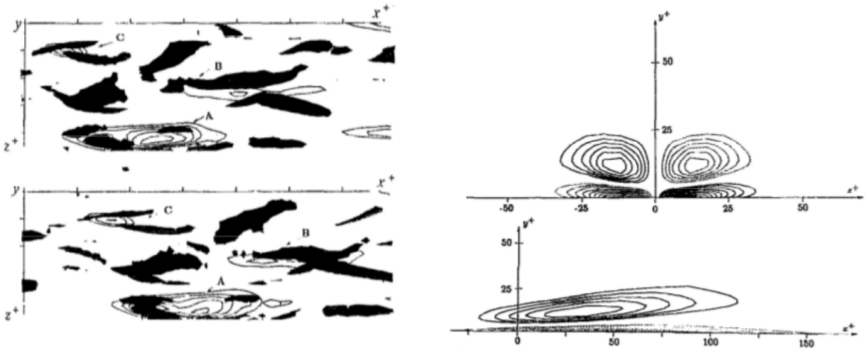


Figure 2.2.7: Time interval between consecutive bursts in a flat-plate flow [Runstadler et al., 1963, Schraub and Kline, 1965, Kim et al., 1971].

This idea is further proposed by Kravchenko and co-workers [Kravchenko et al., 1993], who have demonstrated a correlation between regions of high skin-friction at the wall and longitudinal counter-rotating vortex pairs. As a result of two-point correlation measurements, iso-surfaces of stream-wise vorticity have been observed right above high skin-friction regions ($13 < y^+ < 30$, Fig. 2.2.8).



(a) (b)

Figure 2.2.8: Top view of isosurfaces of stream-wise vorticity (a); contours of conditionally-averaged, stream-wise vorticity (b) [Kravchenko et al., 1993].

Studies above have demonstrated the importance of streaks in the dynamics of near-wall turbulence. However, as illustrated later in Sect. 2.2.2, streak bursting and stream-wise vortices actually seem to be part of a large three-dimensional mechanism controlled by the outer flow dynamics.

2.2.2 The Logarithmic and Outer Regions

As detailed in Sect. 2.2.1, the near-wall cycle includes formation, lifting, and break-up of persistent regions of low-speed fluid named *streaks*. In addition, longitudinal counter-rotating vortex pairs can produce persistent fluid ejections away from the wall. This process is

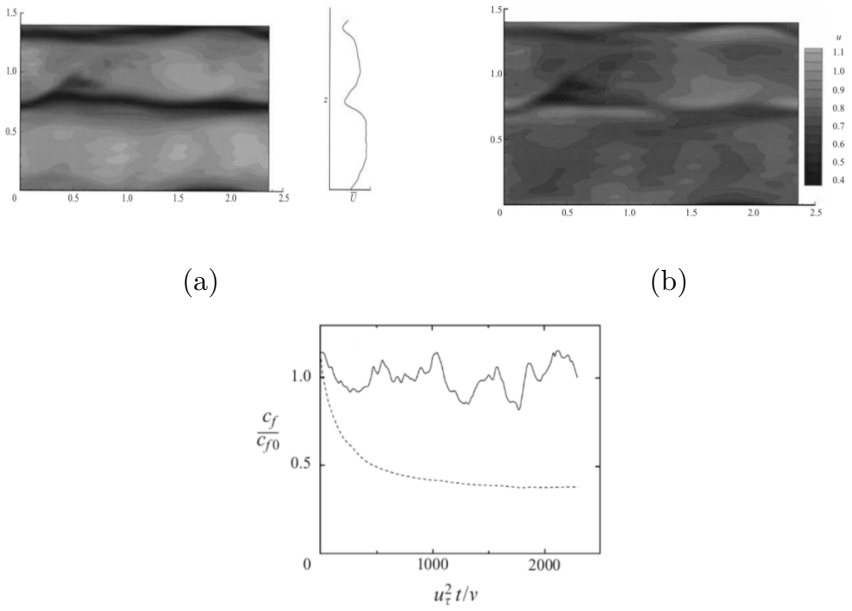


Figure 2.2.9: Maps of stream-wise velocity in a plane at $y^+ = 30$. Maps before (a) and after streak filtering (b). Time evolution of the skin friction for channel flow (c); streak-unfiltered (solid line), and streak-filtered wall (dashed line). The initial conditions is a fully developed channel at $Re_\tau = 190$ [Jimenez and Pinelli, 1999].

coupled with violent, intermittent, fluid eruptions or *sweep-ejection events* which come from break-up of oscillating near-wall streaks. Some authors, such as Jimenez and Pinelli [Jimenez and Pinelli, 1999] have suggested that the near-wall cycle is autonomous. In other words, the cycle is primarily due to streak bursting and there is no involvment of the outer dynamics. To prove this thesis, they filtered low-speed streaks up to $y^+ = 100$, at moderate Reynolds numbers ($Re_\tau \approx 200$) from their DNS simulations. In this way, they have been able to disrupt the near-wall cycle, responsible for high friction at the wall (Fig. 2.2.9).

However, despite the apparent self-sustenance of the near-wall cycle [Jimenez and Pinelli, 1999], some other investigations [Head and Bandyopadhyay, 1981] are suggesting the involvement of three-

dimensional vortex structures extending from the inner buffer layer up to the outer region. These motions are produced from a combination of stretching, compression and roll-up of transverse vortical lines and have largely been observed through flow visualisations (Fig. 2.2.12). Size and morphology of these organized motions can vary significantly. For example, some vortices can attain twelve to fourteen times the radius of pipes [Hutchins and Marusic, 2007a, Kim and Adrian, 1999], or twenty times the half-height of turbulent channels [Del Alamo and Jimenez, 2003, Jimenez and Pinelli, 1999] in the longitudinal direction. As a result of the above observations, Head et al. [Head and Bandyopadhyay, 1981] have formulated a model where hairpin eddies have their own characteristic signature:

(a) **A span-wise vortex named *Head* or *Arch* produced by transverse roll-up.** This vortex can generate persistent fluid ejections in the outer region;

(b) **A pair of stream-wise counter-rotating vortices named *Legs*.** Legs are the main mechanism through which hairpin eddies can induce streak lift-up [Robinson, 1991] (Fig. 2.2.13);

(c) ***Necks*, i.e. regions of connection between arches and legs;**

(d) ***Sweep-ejection events.*** This mechanism results directly from streak bursting and is coupled with the formation of an inclined shear layer.

In addition, hairpins are distiguished from horseshoes, based on:

1. **Their inclination with respect to the stream-wise direction,** which is constant with Reynolds number (Fig. 2.2.11);

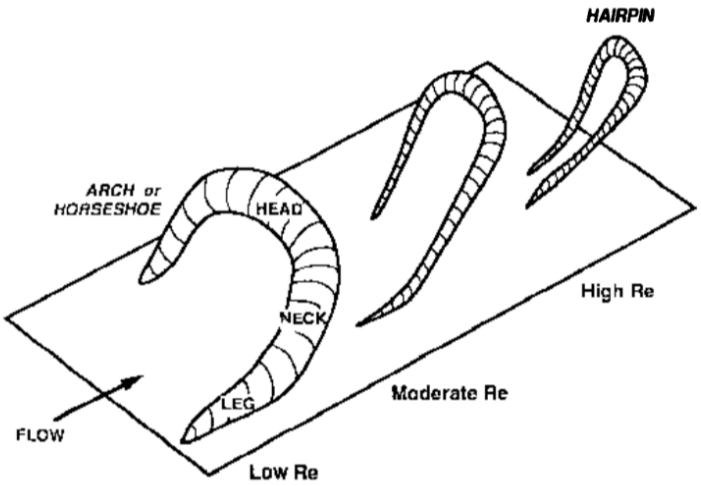
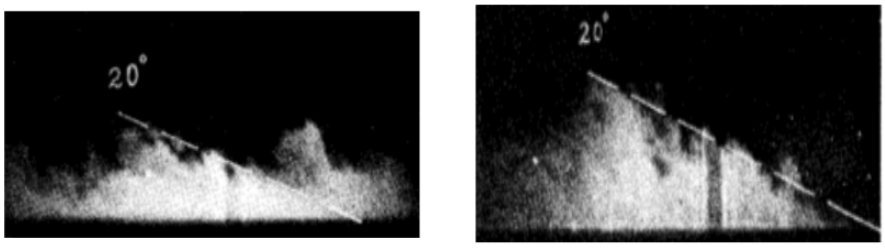


Figure 2.2.10: Geometrical configuration and nomenclature for hairpin structures at different Reynolds numbers [Head and Bandyopadhyay, 1981].



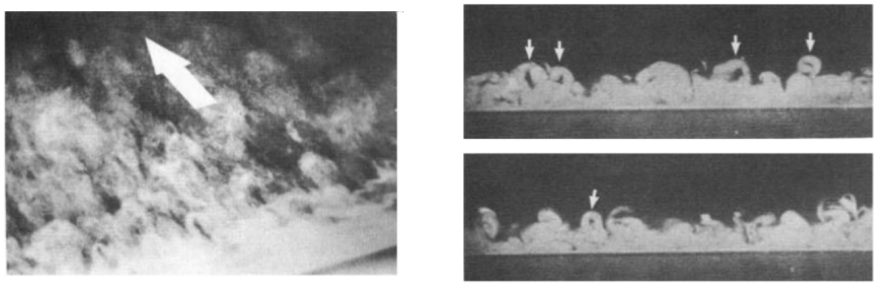
(a) (b)

Figure 2.2.11: Inclination angle of hairpin structures with Reynolds number. Flow visualisation on a zero-pressure gradient boundary layer. $Re_\theta = 7485$ (a), and 14500 (b) [Bandyopadhyay, 1980].

2. **Their distortion and elongation,** which can vary with the Reynolds number. As Reynolds number increases, vortices are stretched more and more (Fig. 2.2.10);

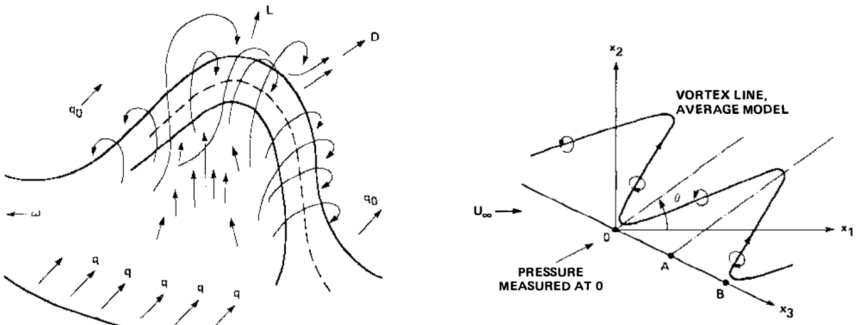
3. **Their extension through the boundary layer thickness.**

As further suggested by Hussain [Husssain, 1986], hairpins can exert a dual influence on the near-wall region by means of their heads and legs, which can produce persistent localised fluid ejections from the near-wall region (Fig. 2.2.14). This concept is in agreement with a



(a) (b)

Figure 2.2.12: Hairpin eddies in reattaching flow past circular rod: general (a), and cross-stream (b) illumination [Head and Bandyopadhyay, 1981].



(a) (b)

Figure 2.2.13: (a) Model for a three-dimensional vortex structure, [Theodorsen, 1952]; (b) Vortex-line model in the near-wall region [Willmarth and Tu, 1967].

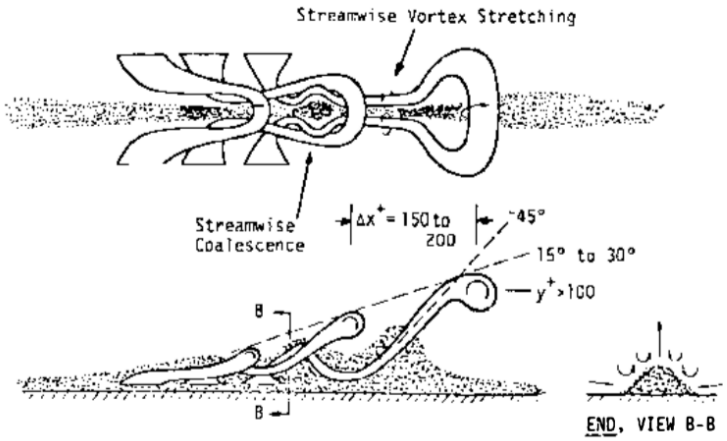


Figure 2.2.14: Hairpin formation, stretching, and interaction with the near-wall region [Smith, 1984].

comprehensive model by Praturi [Praturi and Brodkey, 1978] who has described the physical interaction of three-dimensional motions with the near-wall region in the form of *flow entrainment* from the outer layer (Fig. 2.2.15).

In a similar way, Choi and Orlandi [Choi, 1986, Choi, 1989, Orlandi and Jimenez, 1994] have argued evidence of large, three-dimensional vortex structures developing above streak bursts. Later on, Schoppa and Hussain [Schoppa and Hussain, 2002] have supported this idea after making use of linear perturbation analysis for DNS data of Poiseuille channel flow. According to this model, hairpin eddies belong to a closed-loop cycle which is resumed in the following points and illustrated in Fig. 2.2.16:

1. **The wall no-slip condition produces shear stress,** which results in the formation of span-wise vortex lines;

2. **Transverse vortex lines are strained longitudinally,** due to impingement of high-speed regions of fluid on the wall;

3. **Hairpin loops are formed and convected downstream,** as a result of vortex stretching and transverse roll-up. Stream-wise, counter-rotating vortices are hairpin legs;

4. **Hairpin legs come close one to another,** since hairpins are convected and strained down-stream at a specific angle with respect to the longitudinal direction. In this phase, streaks and low-speed fluid are persistently ejected from the near-wall region;

5. **Streaks are lifted up and their motion becomes unstable until breakup occurs.** This process induces sweep-

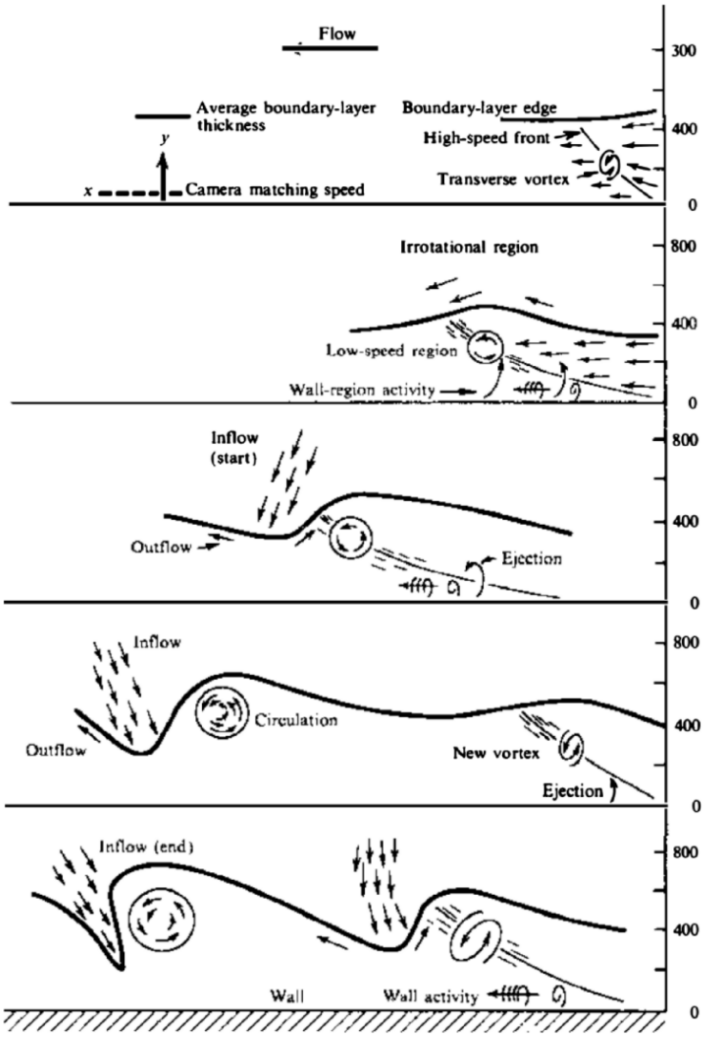


Figure 2.2.15: Model of interaction of three-dimensional vortex structures with the near-wall region. Time evolution from top to bottom [Praturi and Brodkey, 1978].

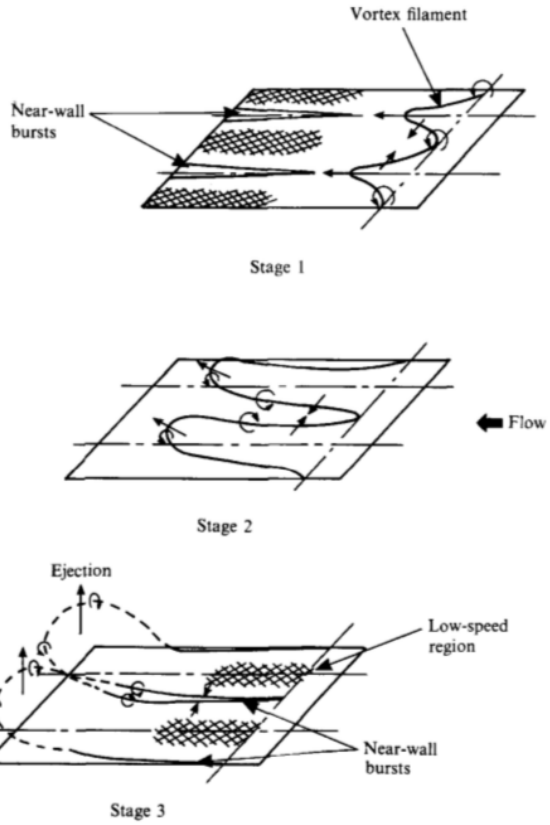


Figure 2.2.16: Sketch of the cycle of formation and re-generation of hairpin vortices [Choi, 1989].

ejection events, causing high-speed fluid regions to impinge on the wall[2];

6. **A new cycle for the formation of a hairpin vortex has started.**

Further investigations have suggested that hairpins can form in packets. This has firstly been observed by Zhou [Zhou et al., 1996, Zhou et al., 1999] through the analysis of DNS data of channel flow at $Re_\tau = 180$, where an initial isolated vortex was superimposed on the mean flow. Evolution over time has shown that vortices can turn into a package of sequential hairpin eddies, through connection of stream-

[2]Sweep-ejection events are associated with negative Reynolds stress, $\overline{u'v'} < 0$, i.e. wall-normal v' and stream-wise u' velocity fluctuations have opposite sign.

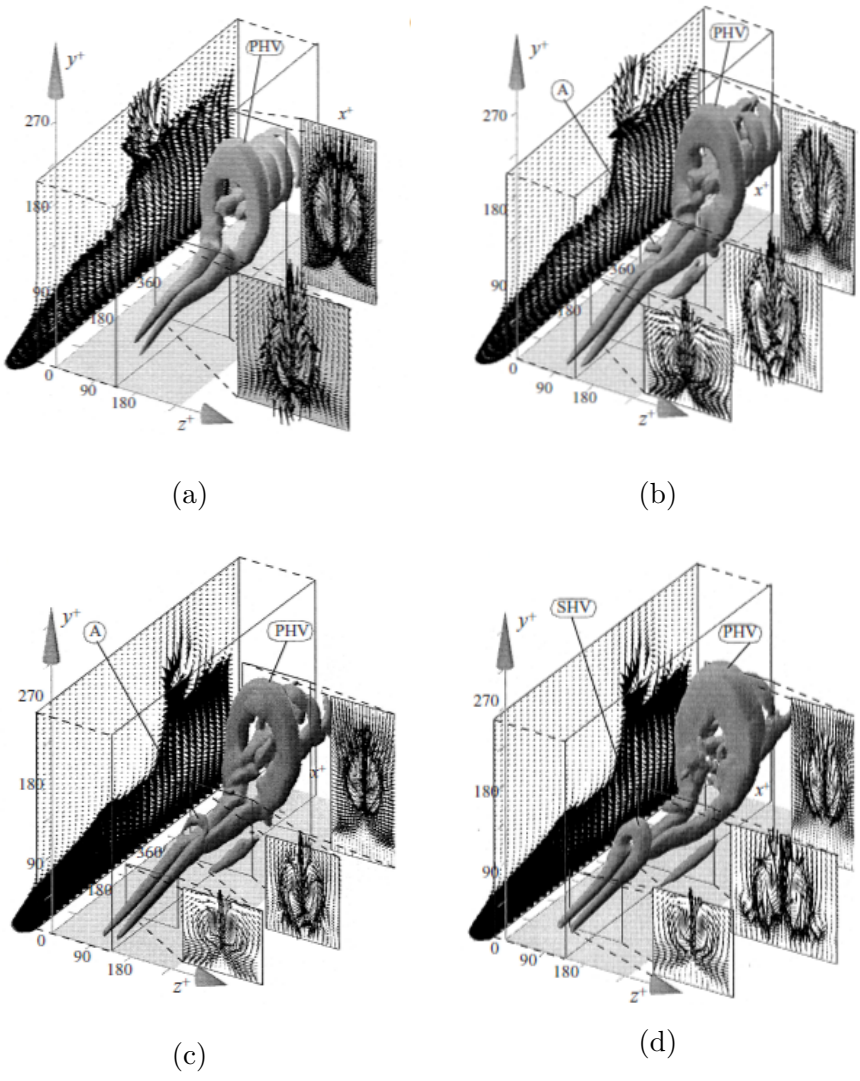
wise vortices with transverse arches. Whenever a primary hairpin is sufficiently stronger than the mean velocity gradient, it can induce further stream-wise vortices. This process results in the formation of a series of *hairpin children* (Fig. 2.2.17), which can slowly decay after 500 viscous time units or extend for more than 10000 space units. Transverse roll-up is induced by sweeps and ejections through an inclined shear layer (Fig. 2.2.18) which is the velocity deficit between free stream and the convection of hairpin vortices.

In Sect. 1.3 it has been explained that one of the requirements of the flow actuator for skin-friction reduction is the identification of hairpin vortices. In this context, low-speed regions of fluid are matter of primary importance. In fact, several studies [Tomkins and Adrian, 2003, Adrian et al., 2000, Ganapathisubramani et al., 2003, Kim and Adrian, 1999] have suggested that low-speed streaks can be flanked by agglomerations of hairpin packets (Fig. 2.2.19). This conjecture has further been supported through two-dimensional PIV measurements [Adrian et al., 2000] showing that hairpin heads are typically located along the border between different zones of uniform momentum (Fig. 2.2.20)[3]. Based on the above considerations about the interaction of hairpin vortices and regions of low-speed fluid, wall-parallel regions of momentum deficit are the key to identify outer coherent motions. This approach will be put into practice and presented in Chapt. 3.

In summary, hairpin eddies can play a key role for active feedback control of turbulent skin friction. In fact, they are involved in the near-wall cycle through:

(a) Induction of streak lift-up and bursting;

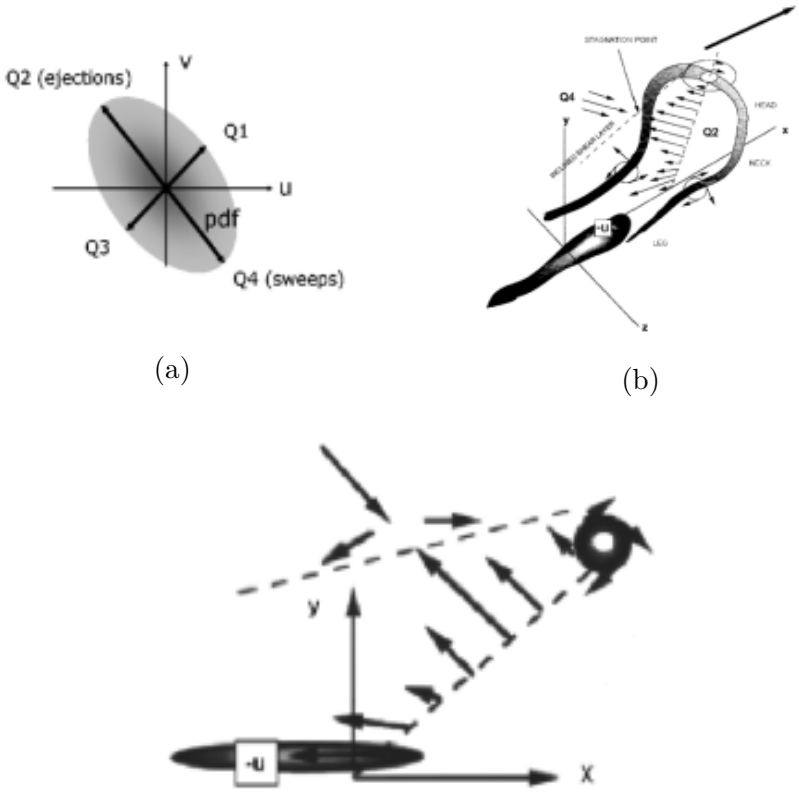
[3]The border between these zones of uniform momentum shows a series of inflections near local regions of high span-wise vorticity, which are believed to be sections of hairpin heads, [Adrian et al., 2000, Adrian, 2007].



(a) (b)

(c) (d)

Figure 2.2.17: Formation of a secondary hairpin vortex (SHV) from a primary structure (PHV). Contours of enstropy λ_{ci}^2. Time varies from $t^+ = tu^2/\nu$ =63 (a), 72 (b), 81 (c), 117 (d). DNS simulation of channel flow at $Re_\tau = 180$ [Zhou et al., 1999].



(a) (b)

(c)

Figure 2.2.18: Hairpin signature is accompanied by negative Reynolds stress ($-\overline{uv}$) resulting from intermittent events in the second and fourth quadrant of the u-v plane (a); sketch of hairpin signature (b) and (c) [Adrian, 2007].

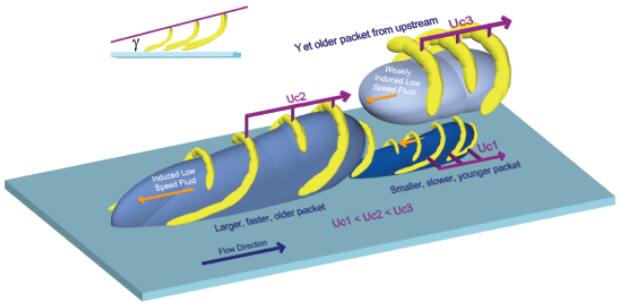


Figure 2.2.19: Model of interaction between hairpin packets and regions of momentum-deficit [Adrian, 2007].

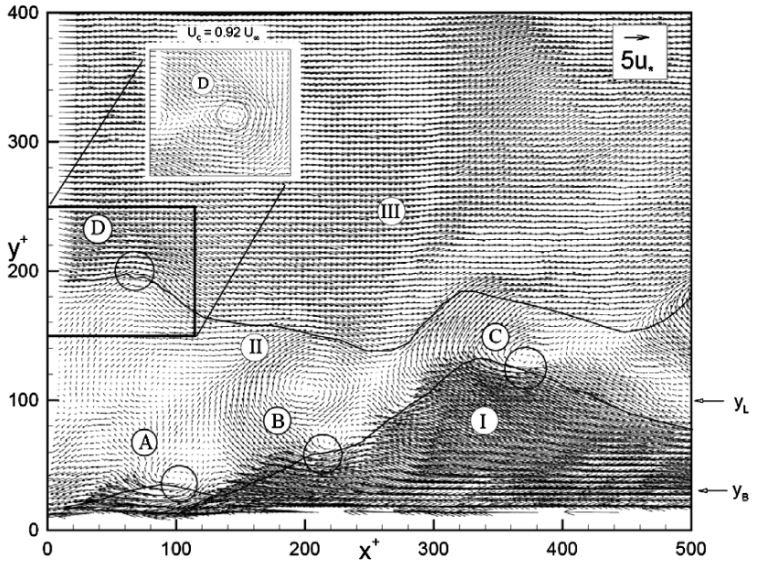


Figure 2.2.20: Signature of hairpin packets from a PIV measurement. Wall-normal, longitudinal plane of velocity data in a turbulent boundary layer at $Re_\tau = 930$. Uniform regions of momentum are labeled as I, II, III respectively [Adrian et al., 2000].

(b) Formation of secondary and tertiary vortices;

(c) Interaction with low-speed regions of fluid, which suggests a new approach to detect hairpin heads.

Numerical simulations [Zhou et al., 1996] and experimental measurements [Kang et al., 2008] have demonstrated that disruption of hairpin arches can temporally interrupt the near-wall cycle and reduce fluid inrushes responsible for high friction at the wall. These considerations reinforce the approach which makes use of hairpin eddies to reduce turbulent drag.

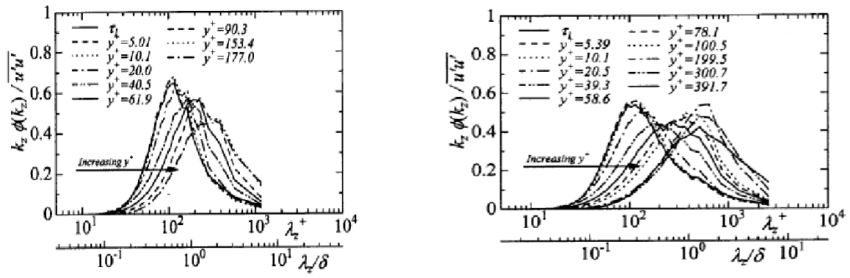
2.2.3 Correlation between Inner and Outer Regions

The interaction between outer coherent motions and the near-wall cycle has been largely debated over the last few decades. One of the first speculations [Choi, 1986, Choi, 1989] has suggested a mutual induction between near-wall bursts, upward fluid ejections and hairpin loops.

A similar description has been given by Robinson [Robinson, 1991], and further supported by Aubri and co-workers [Aubri et al., 1988], through proper orthogonal decomposition (POD) applied to the governing Navier-Stokes equations. As a result, the outer layer can exert pressure excitation to affect the frequency of near-wall bursts. This result is in contrast with works from Jimenez [Jimenez and Pinelli, 1999, Jimenez et al., 2004] who has demonstrated that the near-wall cycle is autonomous.

Evidence of the influence of outer coherent motions on the near-wall region has also been provided by Abe [Abe et al., 2004], through the analysis of pre-multiplied energy spectra of stream-wise velocity fluctuations, and Baars [Baars et al., 2015], by making use of wavelet transforms. As a result, a bimodal behavior was observed, especially at high Reynolds numbers (Fig. 2.2.21).

A similar trend has been confirmed through hotwire measurements by Hutchins, Marusic and Mathis [Hutchins and Marusic, 2007a, Hutchins and Marusic, 2007b, Mathis et al., 2009], who supported the idea of an *outer peak* in the pre-multiplied energy spectrum of streamwise fluctuations ($k_z\Phi_{uu}/u_\tau^2$). This peak is the energetic signature of outer coherent motions (Fig. 2.2.22) and can be scaled with the boundary layer thickness ($y/\delta \approx 0.06$, $\lambda_x/\delta \approx 6.0$). Outer



(a) (b)

Figure 2.2.21: Pre-multiplied energy spectra of stream-wise velocity fluctuations. $Re_\tau = 180$ (a), 395 (b) [Abe et al., 2004].

motions can maintain their near-wall *footprints* especially in the buffer layer $y^+ \approx 15$ with length scales of the order of $\lambda^+ = \lambda u_\tau/\nu \approx 1000$.

Based on the above considerations, although Morrison [Morrison, 2007] has argued that the interaction between the near-wall cycle and outer motions is non-linear, Mathis and colleagues [Mathis et al., 2011a, Mathis et al., 2013] have proposed a linear semi-empirical model, where the inner signal is a function of modulation and superposition of outer motions. In this way, longitudinal fluctuations in the inner region, namely u_p^+, have been reconstructed from measurements in the logarithmic and outer regions. The model (Eq. 2.1) relies upon the assumption of an *inner universal* signal, u^u which is statistically independent from Reynolds number; α and β represent respectively the superposition and amplitude modulation induced by outer coherent motions; whereas θ_L is the mean inclination angle of large-scale motions, calculated based on cross-correlation of stream-wise fluctuations in the near-wall ($y^+ \approx 30$) and logarithmic regions ($y_O^+ = 3.9Re_\tau^{1/2}$)[4] (Fig. 2.2.23). As a result, the inclination angle of the outer coherent motions is estimated of the order of $\theta_L \approx 12.5^o$.

[4]For further details, readers are referred to the respective literature [Mathis et al., 2011a, Mathis et al., 2013].

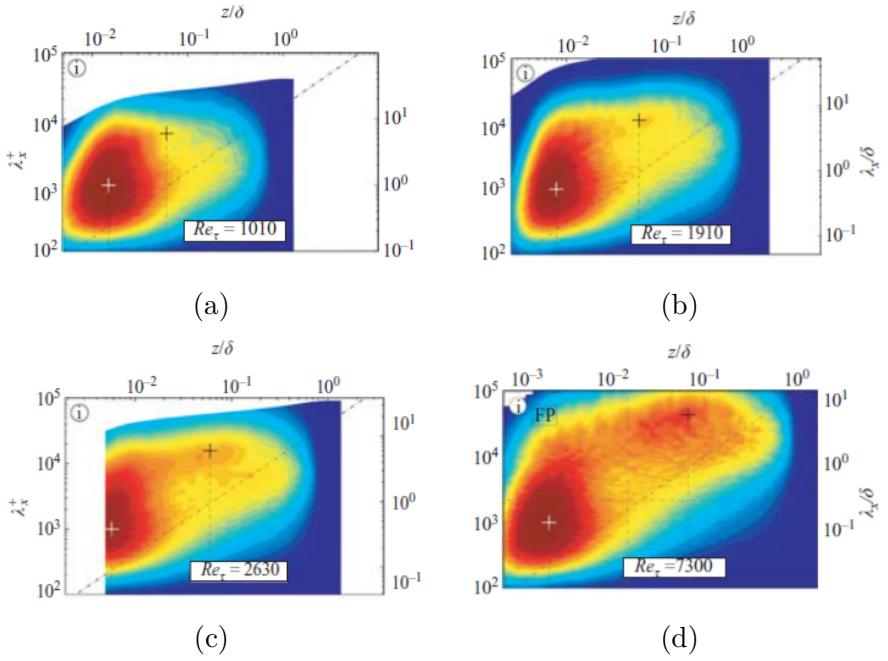


Figure 2.2.22: Contour maps of pre-multiplied energy spectra of stream-wise velocity fluctuations. Re_τ = 1010 (a); 1910 (b); 2630 (c); 7300 (d) [Hutchins and Marusic, 2007a].

$$u_p^+(y^+) = u^u(y^+)[1 + \beta u_{OL}^+(y_O^+, \theta_L)] + \alpha u_{OL}^+(y_0^+, \theta_L) \qquad (2.1)$$

The correlation in Eq. 2.1 has been challenged by Agostini [Agostini and Leschziner, 2014], who questioned the imposition of a pre-defined filter to separate large and small scales of turbulence. By contrast, Agostini and Leschziner made use of the Huang-Hilbert Empirical

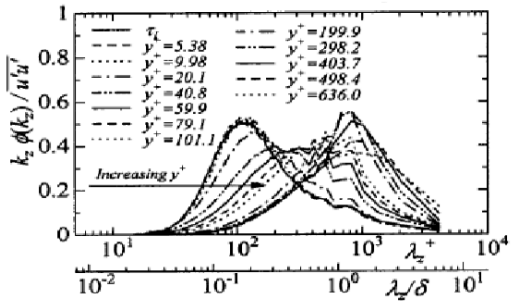


Figure 2.2.23: Calculation of the superposition coefficient and inclination angle of outer coherent motions, through cross-correlation function [Mathis et al., 2011a].

Mode Decomposition (EMD) to extract near-wall footprints, based on the velocity signal itself. Therefore, an improved method has been proposed to predict the near-wall shear stress which takes into account:

1. **Superposition;**
2. **Modulation;**
3. **Distorsion induced by sweep-ejection events.**

In other words, the universal inner signal is actually dependent on near-wall distortion effects which are indirectly induced by outer coherent motions.

In brief, there is consolidate evidence of interaction between outer coherent motions and turbulence near-wall cycle. A closed-loop mechanism has been identified in the maintenance of turbulence production, which invokes streaks instability, sweep-ejection events, and formation of hairpin packets. In addition, hairpin vortices are believed to be interfaced with low-speed regions of fluid. This thought makes it possible to identify outer coherent motions based on momentum-deficit regions of fluid.
All the above considerations suggest that hairpin vortices are the key for a novel approach to control turbulent skin friction trough manipulation of the outer dynamics.

2.3 Remote Flow Control

2.3.1 Introduction

Over the past few decades, flow control has been widely investigated for reduction of turbulent drag. For example, passive devices

such as riblets and vane-type vortex generators [Choi, 1989] or sharp-edged flaps [Lumley and Blossey, 1998] have been quite convenient, since they require no additional energy to disrupt the near-wall cycle. However, despite their handiness, passive actuators cannot adapt their response to flow transients; indeed, they can be a parasitic loss. For this reason, active flow control is beneficial for unsteady flows, especially in aeronautical applications.

Different approaches have been proposed for active flow control, and include:

(a) **Dielectric Barrier Discharge (DBD).** A high-voltage current is applied between two electrodes separated by a dielectric material. As a result, air can be ionised, with the production of a plasma jet. Practical applications have regarded control of flow separation and friction drag reduction [Feng et al., 2012, Jukes, 2007, Jukes, 2015]);

(b) **Laser Energy Deposition (LED).** Air break-down is artificially induced by focusing a pulsed laser beam into a small volume. As a result, a spherical shock can form within few tens of microseconds from the laser pulse. Due to the very short time scales, LED has successfully been applied to flow control in supersonic flows [Adelgren, 2003, Adelgren et al., 2005, Ghosh and Mahesh, 2008, Schulein and Zheltovodov., 2008];

(c) **Synthetic Jets.** This technique makes use of small orifices through which periodic suctions and ejections of fluid occur. This method has largely been implemented for control of flow separation [Glezer and Amitay, 2002, Santhanakrishnan and Jacob, 2007, Smith, 1984];

(d) **Wall span-wise oscillations.** This method has successfully been applied by Agostini and co-workers [Agostini et al., 2014a, Agostini et al., 2014b] to disrupt the bursting process and reduce turbulent drag in wall-bounded flows.

Most of the methodologies above differ from remote-flow-control, where flow disturbances are locally introduced in the flow field.
Only Kang [Kang et al., 2008] was able to demonstrate that direct intervention of hairpin eddies in flat-plate flows can produce a friction drag reduction equal to 35%. This was done by producing a jet from the outer region to counteract upward fluid ejections induced by hairpin heads.

Inspired by Kang's results, the research presented in this dissertation aims at exploring alternative methods for remote flow control based on direct intervention of hairpin eddies. An effective disruption of hairpin vortices on aircraft wings can be achieved if the flow actuator can satisfy the following requirements:

1. **A fast time response, so that hairpins can be destroyed before being convected down-stream;**
2. **A response persistence coherent with time scales of hairpin vortices;**
3. **The actuator should be able to produce a local flow expansion large enough to affect hairpin vortices;**
4. **The geometrical configuration should not affect the surrounding flow field.**

On the given grounds, laser energy deposition (LED) is one of the most promising techniques, since it can be re-designed for turbulent

subsonic flows - typical of commercial transportation - and does not require any geometrical arrangements, which is a good point to preserve the wing aerodynamic performance.

2.3.2 Localised Flow Control by Laser Energy Deposition

As explained in Sect. 2.3.1, laser energy deposition (LED) has been identified as a valid method for turbulent drag reduction in subsonic flows. In this view, focused laser beams can produce a local flow disturbance which does not interfere with the surrounding flow field. Laser light is convenient for the following reasons:

(a) Spatial coherence, which can be used to focus laser beams;

(b) Temporal coherence, i.e. light can travel in a fluid at specific wavelenght and energy content;

(c) No mechanical devices are required. Therefore, the dynamic response of the boundary layer is not affected by the displacement of mechanical devices, e.g. flaps, slats, spoilers, etc.

Recent studies have explored the benefits resulting from *dielectric break-down* of air induced by laser energy deposition[5]. For example, laser energy deposition (LED) has been used to produce three-dimensional displays [Saito et al., 2008, Ochiai et al., 2016, Tilma, 2006], where the laser focal point is displaced through specific algorithms to generate three-dimensional images in real time (Fig. 2.3.1). However, the most relevant application for laser energy deposition

[5]As a result of breakup of its dielectric strength, air can become electrically conductive and result in the formation of plasma.

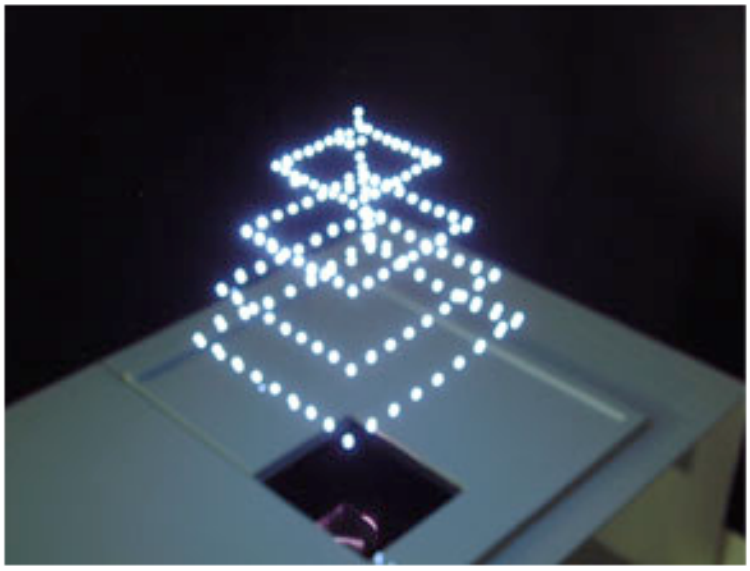


Figure 2.3.1: Three-dimensional image produced as LED-induced air breakdown. Light points are where air is ionised to form plasma [Tilma, 2006].

is flow control. Thanks to its fast-time response, LED has been successful to disrupt shock waves, responsible of sharp heat fluxes on bodies immersed in supersonic flows. A practical example is the manipulation of Edney IV interactions [Adelgren et al., 2005]. This phenomenon is produced by the impingement of an oblique shock wave on the bow shock in front of a spherical model. A pulsed laser with power of the order of 283mJ/pulse has been used to produce a blast shock able to disrupt the *shock lensing effect* (Fig. 2.3.2). As a result, a reduction in the maximum pressure coefficient (order of 30%) has been achieved. From measurements of total pressure at one diameter upstream of the model (Fig. 2.3.3), the overall actuation response time has been estimated to be of the order of 50-200μs. This result is helpful to assess the interaction between laser energy deposition (LED) and coherent motions.

Further applications in flow control [Knight and Yan, 2007] making use of laser energy deposition are:

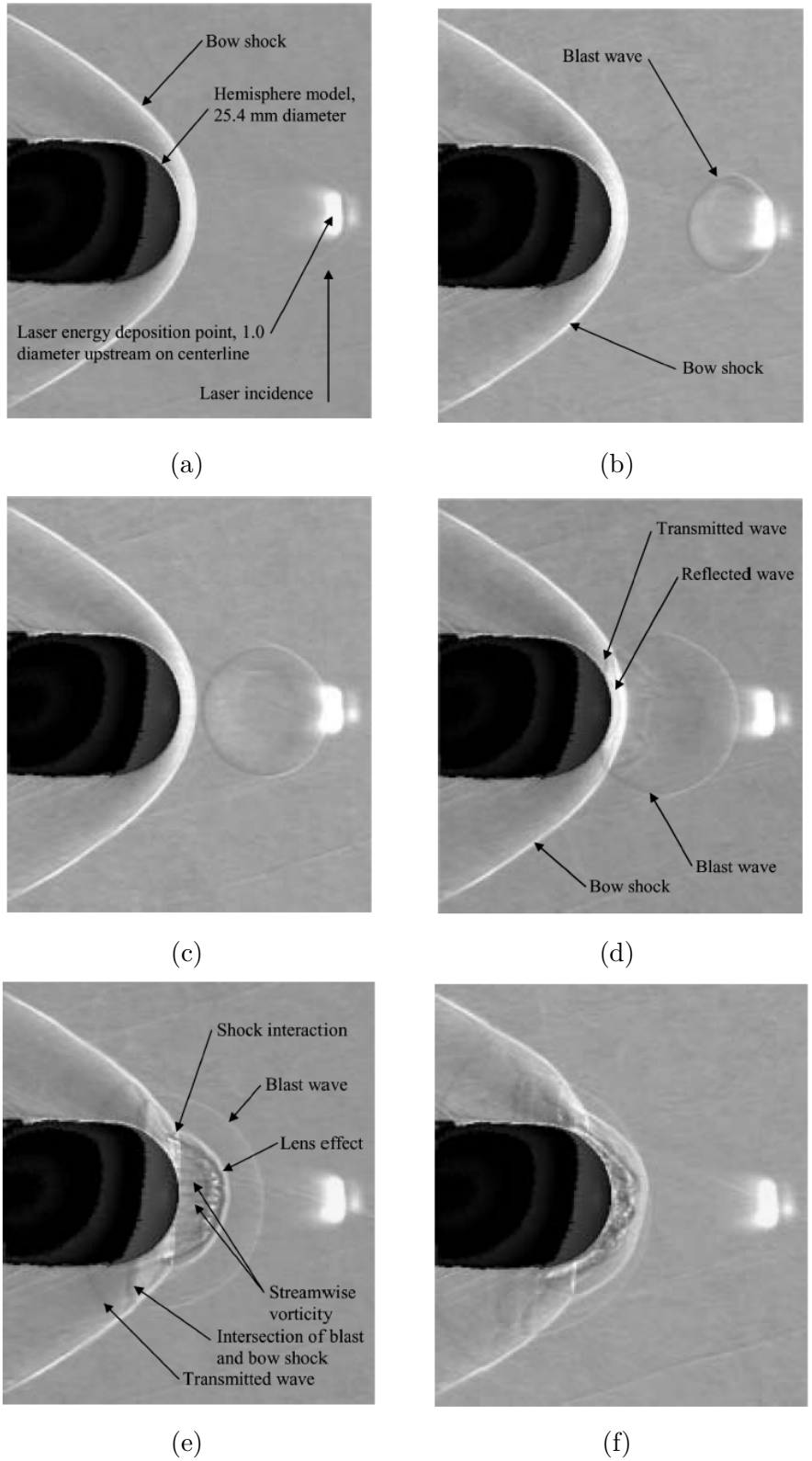


Figure 2.3.2: Control of the Edney IV interaction in front of a sphere at $M_\infty = 3.45$. Time evolution at: $0\mu s$ (a); $10\mu s$ (b); $20\mu s$ (c); $30\mu s$ (d); $50\mu s$ (e); $70\mu s$ (f) from the triggering laser pulse [Adelgren et al., 2005].

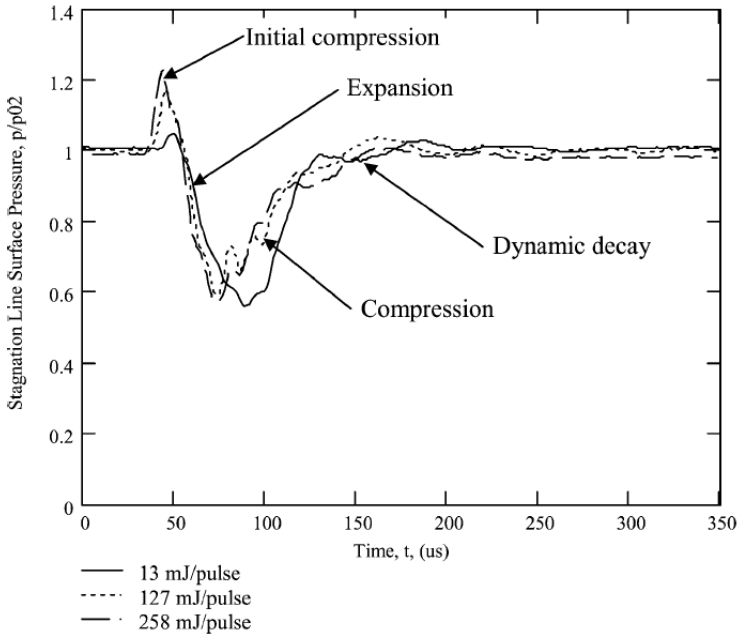


Figure 2.3.3: History of stagnation pressure at 1.0 diameters upstream of the sperical model [Adelgren et al., 2005].

(a) Control of the shear layer in three-dimensional cavities;

(b) Control of vortex breakdown in supersonic transportation. In fact, vortex breakdown can result in roll-moment unbalance in a supersonic aircraft;

(c) Control of normal shocks in an engine compression inlet. Laser energy deposition can enhance the system stability against acoustic disturbances which can compromise the engine start (Fig. 2.3.4).

Physical mechanisms induced by LED in air have also been investigated through numerical simulations. An example is the work by Ghosh [Ghosh and Mahesh, 2008], who analysed the dynamic effects of laser energy deposition at different energy levels in quiescent air. Simulations have shown three physical effects:

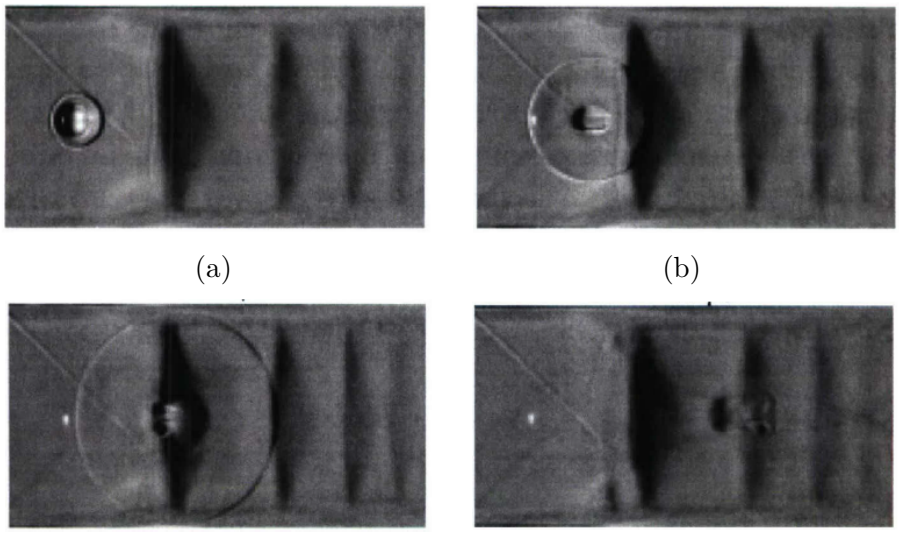


Figure 2.3.4: Phase-average Schlieren visualisation of the interaction between a blast shock produced through lased energy deposition and the normal shock train in a compression inlet; $M_\infty = 2.0$. Time evolution at: (a) $10\mu s$; (b) $40\mu s$; (c) $80\mu s$; (d) $200\mu s$ from the triggering laser pulse [Knight and Yan, 2007].

1. **An internal, high-enthalpy, tear-drop-shaped core of ionised air,** named *plasma*;

2. **A blast shock wave,** which initially expand in the normal direction with respect to the core symmetry axis, due to high pressure gradients;

3. **A more uniform propagation of the blast shock,** accompanied by roll-up of the plasma core.

Plasma roll-up is attributed to baroclinic effects, i.e. the misalignment between pressure and density gradients in the governing vorticity equation (Fig. 2.3.5).

The presence of a blast shock near the plasma core has been witnessed by pressure contours (Fig. 2.3.6) through an initial tear-drop shape. Over time, blast shocks become spherical, due to transverse advection of the temperature gradient.

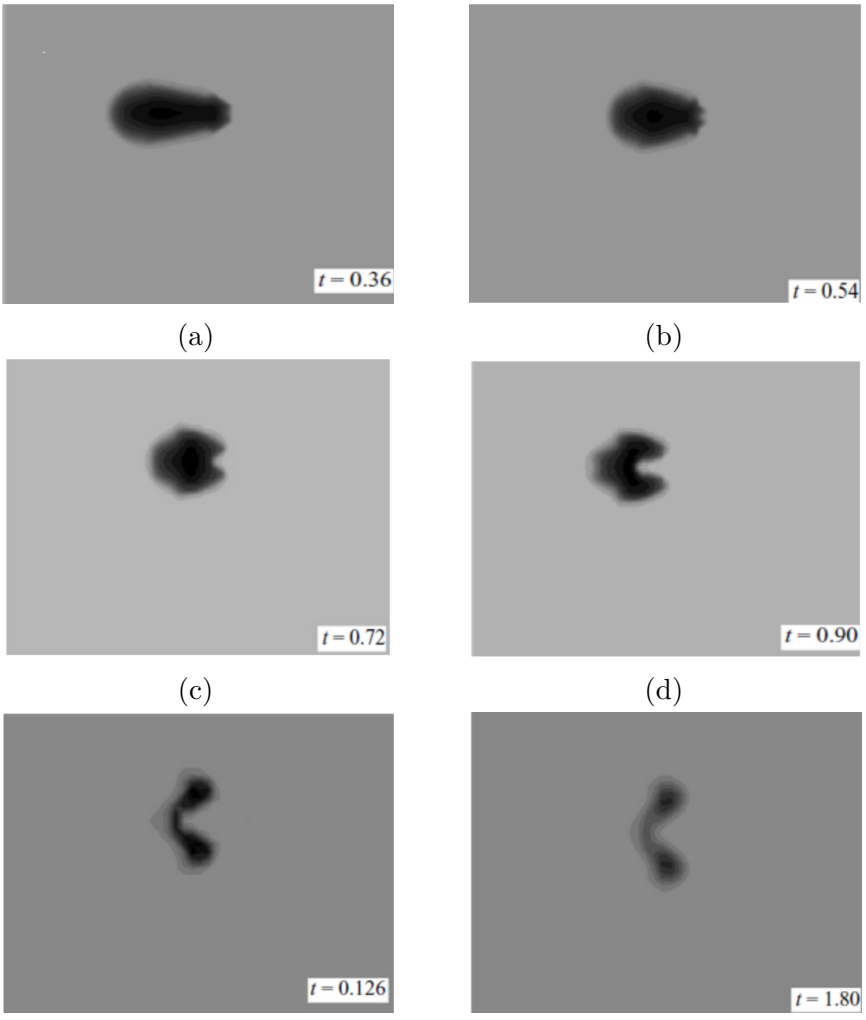


Figure 2.3.5: Evolution of plasma roll-up. $\hat{t} = t/t^* = 0.36$ (a); 0.54 (b); 0.72 (c); 0.90 (d); 0.126 (e); 1.80 (f). $t^* = 15.9\mu$s, based on measurement of the sound speed [Ghosh and Mahesh, 2008].

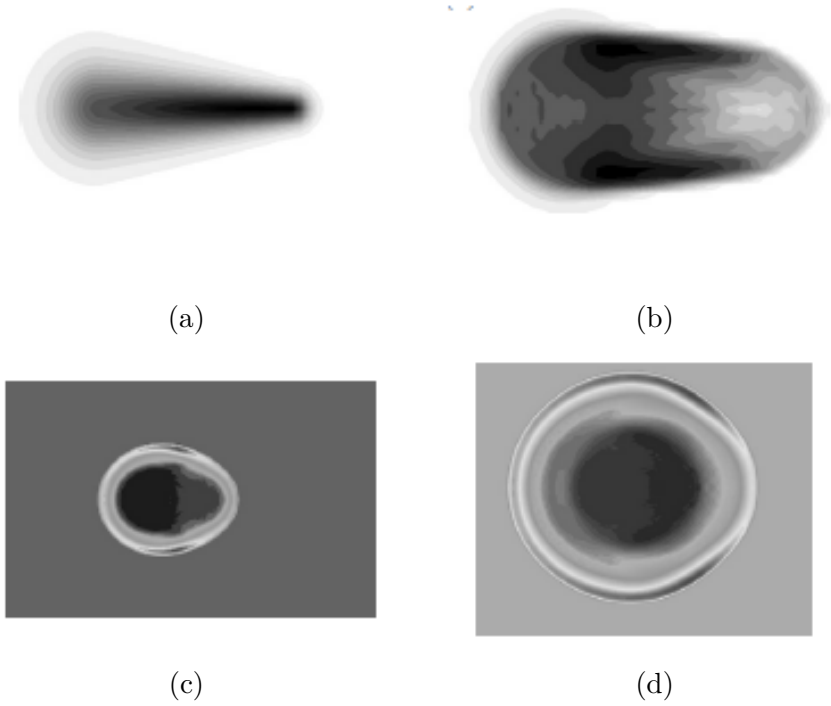


Figure 2.3.6: A blast shock wave induced by LED. Pressure contours at $\hat{t} = t/t^*$ =0.0 (a), 0.04 (b), 0.36 (c), 0.99 (d) [Ghosh and Mahesh, 2008].

All the above processes have further been confirmed by Schulein [Schulein and Zheltovodov., 2008], who has investigated the lensing effect in front of blunt bodies at M_∞ =2 (Fig. 2.3.7). This was done by varying:

- Distance between the laser focal point and the model;
- Deposition energy level;
- Laser beam pulsed mode (single/double);
- Time delay between the laser pulses when in double mode.

In summary, all the above experiments and numerical simulations have shown that laser energy deposition (LED) is beneficial for supersonic applications, where the actuation response should lie within few tens of microseconds.

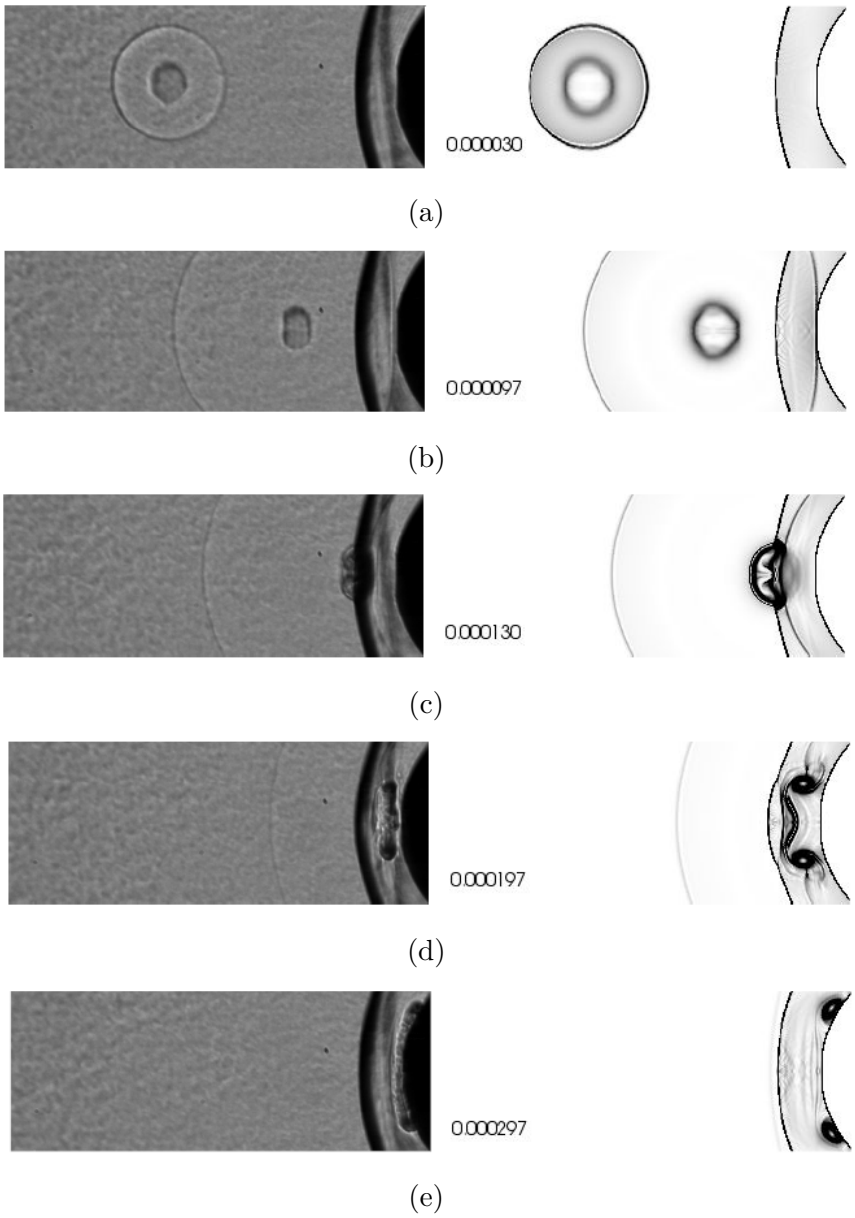


Figure 2.3.7: Flow shadowgraph (left) and numerical simulation - density gradients (rigth) of blast-shock interaction over a blunt body at $M_\infty = 2$. Snapshots at t= 30 (a), 97 (b), 130 (c), 163 (d), 297 (e) μs from the laser pulse [Schulein and Zheltovodov., 2008].

However, in view of the actuation of hairpin vortices in turbulent *subsonic* regimes, the work presented in this dissertation proposes a different approach; i.e. to make use of laser energy deposition to trigger instead other physical mechanisms, whose effects can sufficiently persist to influence coherent motions. More details will be given in Chapt. 4.

2.4 Summary

To summarise, the goal of the project presented in this dissertation is to develop a new concept for flow control where hairpin vortices can actively be manipulated to achieve turbulent skin-friction reduction. This actuator can be assembled for aerospace applications, especially for flow control over aircraft wings.
The strategy for flow control has been built on the basis of some *tool-kit* concepts grabbed from the existent literature. This review has shown that:

(a) **The near-wall cycle comprises formation, lift-up and breakup of low-speed regions of fluid denominated streaks;**

(b) **Streak break-up results in violent eruptions of fluid called sweep-ejection events;**

(c) **Sweeps and ejections appear in the form of high and low speed regions of fluid which are respectively pushed towards and away from the wall;**

(d) **Impingement of high-speed fluid on the wall results in large shear stress and skin friction;**

(e) **Hairpin vortices can induce persistent ejections of fluid through their legs and heads away from the wall.**

(f) **Hairpin packets can flank and surround low-speed regions of fluid.**

Therefore, hairpin vortices play a major role in the dynamics of turbulent boundary layers and can be helpful in the disruption of the near-wall cycle.

Thus far, hairpin motions have been identified through two-point correlation measurements and characterised by making use of mathematical criteria (e.g. the λ_2, swirling strength and Q criteria [Lee et al., 1974, Dubief and Delcayre, 2000, Jeong and Hussain, 1995]). However, current methods might not be suitable for a real-time actuator which should continuously adjust its response to efficiently maintain low shear stress at the wall.

In view of developing the actuator in a practical way, laser energy deposition (LED) has been found to have an outstanding relevance in flow control, due to:

1. **A fast time response,** since laser beams can travel at the speed of light;

2. **Small persistence in time.** In other words, flow perturbations can evolve over short time;

3. **It requires no mechanical devices which could potentially affect flow field (e.g. flaps, slats, spoilers).** This peculiarity is important particularly for aerospace applications where the wing aerodynamic performances can be affected.

Up to this point in research, laser energy deposition has been successful for control of supersonic flows, due to fast flow perturbations

which can evolve within few tens of microseconds from the laser pulse (Sect. 2.3.2). Therefore, this method might apparently not be suitable for subsonic flow control and disruption of coherent motions.

However, this work aims at assembling the above toolkit from the literature to build a new flow-control system capable of actuating turbulent subsonic flows. The novelty encompassed in the work is proposed below:

1. **A methodology to detect outer coherent motions in real-time, which is based on image analysis and pattern recognition of low-speed regions of fluid (Chapt. 3);**

2. **A process making use of laser energy deposition to induce flow disturbances which can persist for sufficient time to affect coherent motions (Chapt. 4).** The flow perturbation should be fast enough to target hairpin loops within their persistence time. This objective can be attained by considering the ignition of flammable bubbles and sublimation of carbon-dioxide particles.

Chapter 3

Recognition of coherent motions by image analysis

3.1 Introduction

As explained in Sects. 1.3, 2.4, the work in this dissertation proposes a method to identify hairpin vortices in real time for turbulent skin friction reduction in subsonic flows. In fact, hairpins disruption is the key to maintain a low shear stress at the wall.

Previous works [Smith and Metzler, 1983, Blackwelder and Eckelmann, 1979] have highlighted the importance of hairpin footprints in the near-wall region. Hutchins et al. [Hutchins and Marusic, 2007a, Hutchins and Marusic, 2007b, Mathis et al., 2009, Mathis et al., 2013, Mathis et al., 2011a, Mathis et al., 2011b] have suggested that some footprints result from modulation and superposition exerted by outer coherent motions. Therefore, in order to target hairpin eddies through a flow actuator, the near-wall information can be used to identify outer coherent motions.

In relation to the hairpin footprints, several other studies [Tomkins

and Adrian, 2003, Adrian et al., 2000, Ganapathisubramani et al., 2003, Kim and Adrian, 1999], have argued that near-wall low-speed fluid regions are flanked by conglomerates of hairpin packets. Therefore, it is reasonable to consider low-momentum regions as a way to detect hairpin vortices.

On the basis of the above thoughts, this work suggests a methodology founded on the analysis and correlation of wall-parallel planes of stream-wise velocity fluctuations. Particular attention is paid to two-dimensional regions of low-speed fluid for the reasons explained above. Analysis is performed on the output of a direct numerical simulation (DNS) of turbulent channel flow at $Re_\tau = 1025$ and $Re_\tau = 1600$ [1].

The approach here proposed is divided in three main stages:

(a) Image processing, to smooth contours of large-scale regions of fluid and remove small scales of turbulence (Sect. 3.2);

(b) Selection of near-wall regions of interests (ROIs), i.e. regions which can potentially be associated with hairpin footprints based on their topology (Sect. 3.3);

(c) Two-dimensional correlation and pattern recognition, with the outer region of the boundary layer (Sect. 3.4).

The work presented in this chapter is the ground for development of an active feedback actuator which can continuously identify and disrupt hairpin eddies, by only using the near-wall information.

[1] The two databases have been respectively provided by Professor M. Leschziner, Imperial College, London [Agostini and Leschziner, 2014, Agostini et al., 2014a] and Dr Y.M. Chung, University of Warwick, [Hurst et al., 2014].

3.2 Image analysis applied to turbulent flows

3.2.1 Introduction

Image processing is crucial for effective object recognition[2]. In fact, models based on two-dimensional correlation are particularly successful on regular contours.

Analysis has been performed on DNS datasets of turbulent channel flow at $Re_\tau = u_\tau h/\nu = 1025$ and $Re_\tau = 1600$, being h the channel half-height. Some more details are provided in Tab. 3.1.

Table 3.1: DNS datasets used to develop a new methodology for recognition of outer coherent motions. Dataset no. 1 from IC London [Agostini and Leschziner, 2014, Agostini et al., 2014a]; dataset no. 2 from Warwick University, [Hurst et al., 2014].

	Wall-normal distance, $y^+ = u_\tau y/\nu$	Streamwise grid length, $\lambda_x^+ = \lambda_x u_\tau/\nu$	Spanwise grid length, $\lambda_z^+ = \lambda_x u_\tau/\nu$
Dataset 1, $Re_\tau = u_\tau h/\nu = 1025$	1.4, 2.9, 4.6 6.4, 8.2, 10.1 12.0, 13.5, 49.7 180.0, 750.0	12,865	6,447
Dataset 2 $Re_\tau = u_\tau h/\nu = 1600$	0.2, 2.0, 5.0 10.0, 15.0, 30.0 60.0, 120.0, 200.0 400.0, 800, 1600	19,200	6,400

[2]For clarification, *objects* are the components corresponding to both high and low speed regions of fluid, obtained after conversion to binary format.

Image processing includes a series of so-called morphological operations [Haralick and Shapiro, 1992, Pratt, 1978], which, on a specific sequence, allow extracting contours of large-scale turbulent structures:

(a) **Spatial median filtering.** This operation is capable of removing impulse noise, while preserving large-scale contours [Sun and Neuvo, 1992];

(b) **Morphological area opening.** It is a filter to remove binary objects whose area is smaller than a certain threshold. Other practical applications include pixel scanning, segmentation and image filtering [Vincent, 1993, Vincent, 1994];

(c) **Morphological skeletonisation.** This operation - normally implemented in data compression for pattern recognition [Lam et al., 1992] and detection of abnormal blood cells, [Izzo and Coles, 1962, Preston, 1961] - consists of deleting pixels from borders of binary components, while their connectivity is preserved. As a result, thickness of binary objects is reduced;

(d) **Morphological branching.** This operation is helpful to remove artificial protrusions or *branches* produced as a result of skeletonisation. In this way, the overall image topology is preserved. Branching algorithms are based on the number of black-neighbour pixels surrounding binary objects [Kong and Rosenfeld, 1996].

Operations described above are repeated in a specific order to finely remove small turbulence scales, while contours of large scales and the overall image topology are preserved.

Numerical parameters for each operation have been determined on the basis of previous observations on near-wall streaks:

(a) **The transverse spacing between near-wall streaks is equal to** $\Delta z^+ \approx 100 \pm 20$ **[Kline et al., 1967, Smith and Metzler, 1983];**

(b) **Near-wall streaks can stretch in the longitudinal direction for many viscous units, namely** $\Delta x^+ \approx 1000$ **[Blackwelder and Eckelmann, 1979, Kreplin and Eckelmann, 1979].**

Therefore, the following sequence is proposed here:

1. **Coarse median filtering.** Applied to two-dimensional maps of streamwise velocity fluctuation, this function can blur small scales of turbulence, while preserving large-scale contours. Regions of the order of $\lambda_x^+ \geqslant 8000$ are considered. A good compromise between effective signal smoothing and shape preservation has been achieved for filter sizes of the order of $\lambda_x^+ \approx 600 - 1000$ and $\lambda_z^+ \approx 50 - 120$;

2. **Conversion of velocity fluctuations to binary format.** This operation can separate high and low speed fluid regions. Furthermore, binary objects can be characterised in terms of contour, perimeter, and centroid [Haralick and Shapiro, 1992, Pratt, 1978];

3. **Coarse morphological area opening.** In this phase, only the smallest objects are removed, especially those whose area is smaller than 1250 square pixels - which corresponds to $\lambda_x^+ \times \lambda_z^+ \approx 400 \times 200$. These values have been selected from

observations of near-wall structures ($y^+ \leqslant 80$) having size of the order of $\lambda_x^+ \times \lambda_z^+ \approx 400 \times 100$ [Robinson, 1991, Jimenez et al., 2004].

4. **Morphological skeletonisation.** Skeletonisation is relevant to compensate thickening effects ($\Delta\lambda_z^+ \approx 250$) in the viscous sublayer which resulted from median filtering. A good compromise between shape preservation and object thinning was achieved by applying a value of 3 to 5 for the two-dimensional, spatial-gradient, edge detector, namely the *Sobel operator*[3];

5. **Morphological branching.** Normally, this operation is coupled with skeletonisation, and can reduce the number of unwanted protrusions which can compromise the image-recognition stage;

6. **Fine median filtering in binary-format images.** Compared to coarse filtering, the filter cell is small to finely smooth large-scale contours. A reasonable compromise between smoothing and shape preservation was achieved by using windows of the order of $\lambda_x^+ \times \lambda_z^+ \approx 180 \times 90$;

7. **Fine area opening.** This operation consists of a final clean-up from large connected components which are significantly smaller than actual regions of interest. More precisely, objects whose length is smaller than $\lambda_x^+ \leqslant 3000$ have been discarded. As a result, only few large connected objects are preserved;

[3]Sobel algorithms are used to detect binary edges and contours, based on high-spatial frequency, [Gonzalez and Woods, 1992, Boyle and Thomas, 1988, Davies, 1990]. When the algorithm threshold is set to an infinite value, the binary component is reduced to its own skeleton. A binary skeleton is more rigorously defined as the locus of all the bi-tangent circles centres, being included within a foreground region, in a given binary image, [Haralick and Shapiro, 1992].

8. **Characterisation of near-wall footprints.** Large-scale binary objects in the viscous sublayer are classified according to their contour coordinates, centroids, and perimeters. This operation was performed through Gaussian mixture models. As a result, near-wall sub-images, each containing a large-scale object, are produced. These sub-images are samples implemented for two-dimensional correlation with wall-parallel planes in the logarithmic and outer regions;

9. **Image correlation and object recognition in the logarithmic and outer regions.** Two-dimensional normalised correlation is applied here[4].

The above sequence was tested on high and low speed fluid regions in the near-wall, logarithmic and outer regions. Presumably, due to their typical streakiness and the fact that they are documented to be flanked directly by agglomerates of hairpins, momentum-deficit regions are more suitable for image analysis than their high-speed counterparts.

3.2.2 Median filtering

As widely recognised in the literature, median filters represent the best practice for signal smoothing, image analysis [Pratt, 1975, Frieden, 1976], and reduction of random impulse noise [Huang et al., 1979, Sun and Neuvo, 1992]. Normally, median-filtered images are blurred compared to their original counterparts. This comes from the definition of two-dimensional median filter, which is illustrated in Fig. 3.2.1. Consider a window size equal to 2M+1 × 2N+1 and

[4] `https://uk.mathworks.com/help/images/ref/normxcorr2.html`.

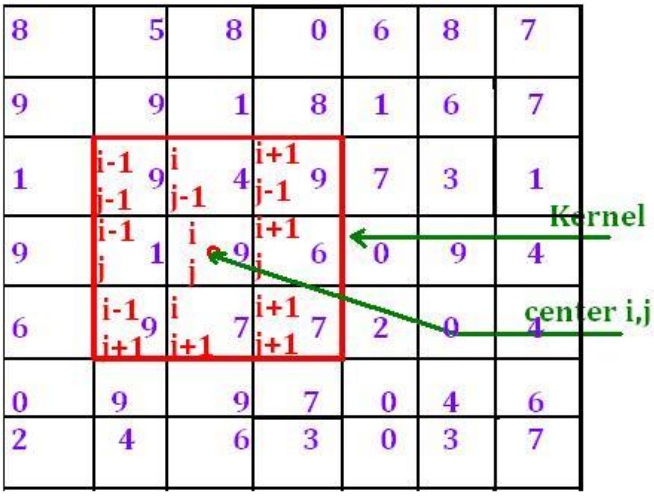
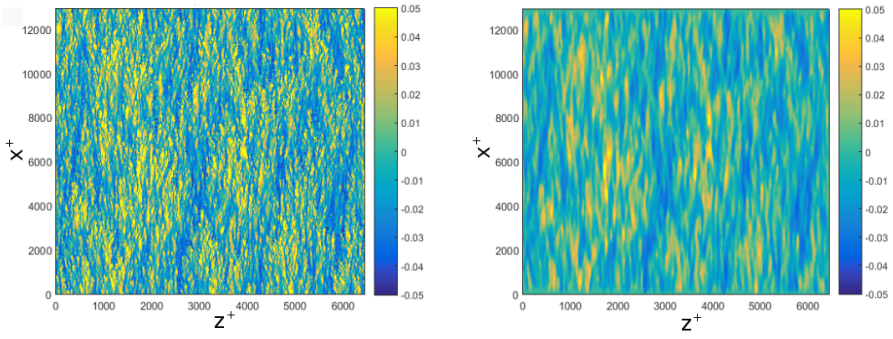


Figure 3.2.1: Schematic of the principle of median filtering. `https://goo.gl/qbSaq8`.

median filter located at the position (i,j), and a set of input samples of size 2M+1 × 2N+1, namely $x_{i-M,j-N}$,..., $x_{i,j}$,..., $x_{i+M,j+N}$. The output of the median filter is given by y_{med} = Med($x_{i-M,j-N}$,..., $x_{i,j}$,..., $x_{i+M,j+N}$), being Med a function calculating the median value among the given samples. The above definition suggests that all image pixels are replaced by respective median values, which are calculated by spanning the filter window in both directions across the target image.

The size of the filter window is one of the most relevant parameters to control which scales of fluctuation are kept in the final processed image. A rectangular window was considered in this study, on the basis of the inclination angle of low-speed motions with respect to the longitudinal direction across a wall-parallel plane, which is physically explained with merging and disconnections of near-wall streaks [Smith and Metzler, 1983, Kline et al., 1967, Blackwelder and Eckelmann, 1979, Kreplin and Eckelmann, 1979]. Preliminary sizes in the stream-wise and span-wise directions have been chosen, namely $\lambda_x^+ \approx 600 - 1000$ and $\lambda_z^+ \approx 50 - 120$ (Fig. 3.2.2).



(a) (b)

Figure 3.2.2: Stream-wise velocity fluctuations at $y^+ = 1.4$. $Re_\tau = 1025$. Original DNS data (a); median filtered data (b). Filter size, $\lambda_x^+ \times \lambda_z^+ \approx 700 \times 60$.

In fact, the above size range is a good compromise between effective filtration of small scales and preservation of large-scale contours. This work is the base to develop an optimisation algorithm, where accurate values of setup parameters can be determined by taking into account the cross-correlation coefficient.

3.2.3 Conversion to Binary Format

Conversion of intensity images to binary format is important to perform image analysis and object recognition. This operation is helpful to:

(a) **Implement morphological operations,** such as area opening, skeletonisation, and branching, relevant to smooth the contour of large-scale objects while removing smaller components;

(b) **Select near-wall regions of interest (ROIs),** i.e. binary objects which can be associated with the footprint of hairpin vortices in the viscous sublayer. In this way, binary images can

be read and binary objects selected, on the basis of the values for λ_x^+ and λ_z^+;

(c) **Identify outer coherent motions,** through two-dimensional cross-correlation.

Binary conversion involves the choice of a fluctuation range, based on correlation between intensity maps and corresponding binary images. Maximum and minimum thresholds in binary conversion, here named as A_{min} and A_{max}, are normally used so that all local values lower than A_{min} are set equal to 0.0, whereas values larger than A_{max} become equal to 1.0. For the present study, reasonable non-dimensional values scaled with the channel friction velocity are identified with A_{min}=-0.025, and A_{max}=+0.025. This separation ensures that high and low speed regions of fluid can be distinguished each other. Results of conversion to binary format are shown in Fig. 3.2.3, at several distances from the wall. The above settings have provided clear contours in binary format.

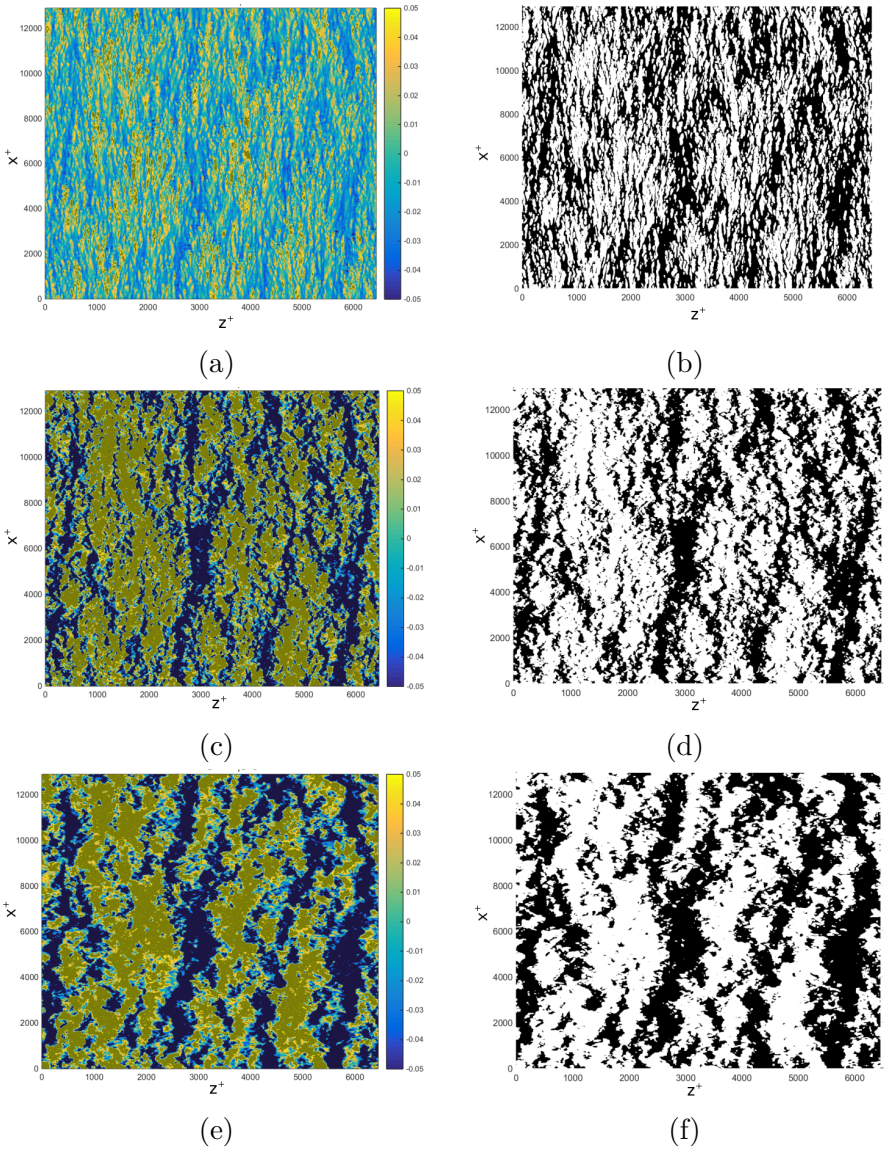


Figure 3.2.3: Conversion of stream-wise velocity fluctuations into binary format at $y^+ = 1.4$ (a, b), 49.7 (c, d), 180.0 (e, f). $Re_\tau = 1025$.

3.2.4 Binary Morphological Processing

Binary morphological operations are performed to finely smooth contours of large-scale objects, while removing smaller components. This was done to enhance two-dimensional correlation of image pairs between the near-wall and outer regions. The author includes as *morphological processing* all those operations such as area opening, skeletonisation, branching, and median filtering which are applied to binary images. The operational sequence has already been mentioned and detailed on Sect. 3.2.1, while the full Matlab code is reported in Sect. A.1.1. Results are shown on Figs. 3.2.4 and 3.2.5, where original and post-processed images are compared. It is observed that only large-scale, connected components remain after the image-processing stage, while small-scale objects are removed.

In summary, this section has introduced a procedure to analyse wall-parallel planes of stream-wise velocity fluctuations in turbulent channel flows. Morphological operations, such as area opening, skeletonisation, branching and median filtering are combined together in a specific sequence and parametrical setup to extract contours of large binary objects from maps of stream-wise velocity fluctuation. In this way, correlation between the viscous sublayer on one side, and logarithmic and outer regions, on the other side, is enabled which allows for real-time identification of outer coherent motions.

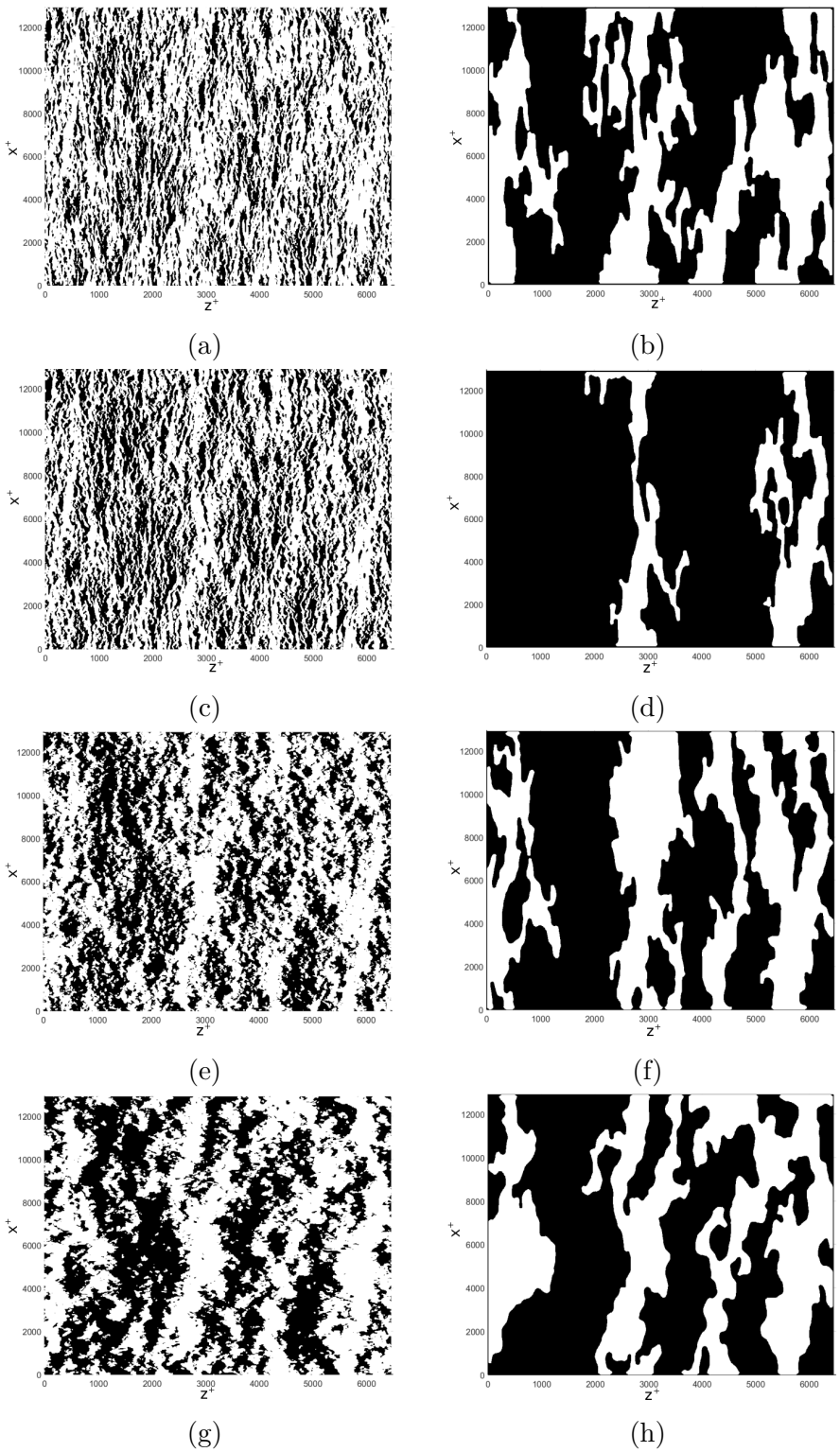


Figure 3.2.4: Morphological Image Processing. Original and processed image pairs, $y^+ = 1.4$ (a, b), 13.5 (b, c), 49.7 (d, e), 180.0 (f, g). $Re_\tau = 1025$.

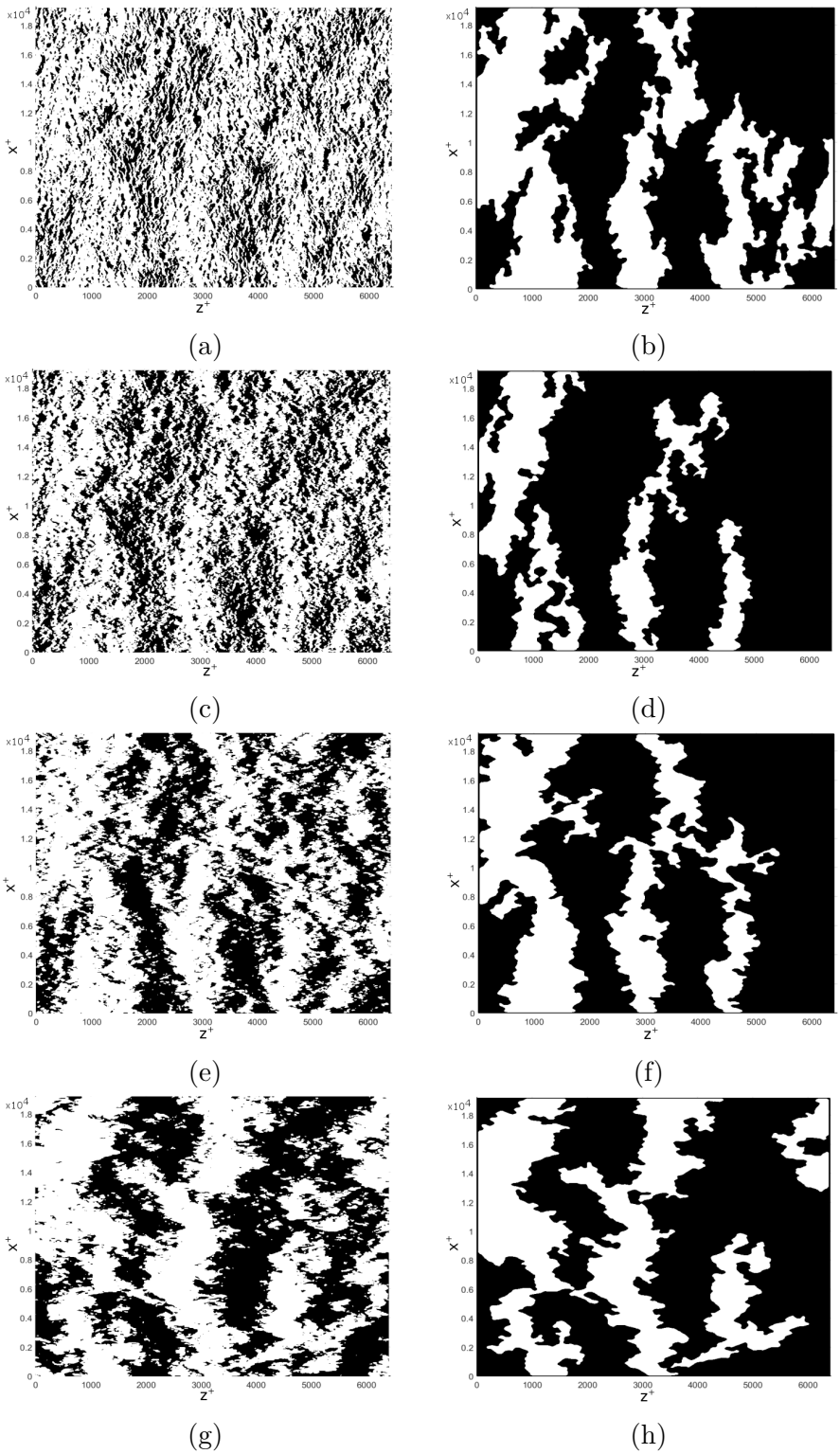


Figure 3.2.5: Morphological Image Processing. Original and processed image pairs, $y^+ = 2.0$ (a, b), 30.0 (c, d), 120.0 (e, f), 400.0 (g, h). $Re_\tau = 1600$.

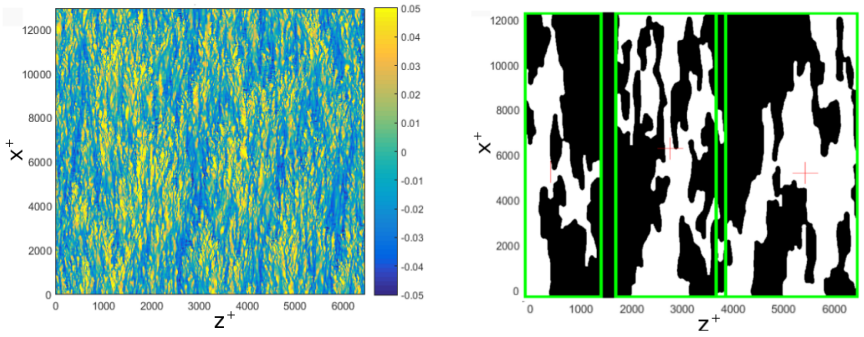
3.3 Near-wall regions of interest

3.3.1 Introduction

Near-wall regions of interest (ROIs) are all those binary objects corresponding to large scales of velocity fluctuation in the viscous sublayer. Based on observations of streaky filaments of fluid in the viscous sublayer [Kline et al., 1967, Smith and Metzler, 1983], the above regions can potentially be hairpin footprints. Regions of interest have been extracted in the previous image-processing step (Sect. 3.2.1), based on their size and morphology, in accordance with experimental observations by Blackwelder and Kreplin [Blackwelder and Eckelmann, 1979, Kreplin and Eckelmann, 1979].

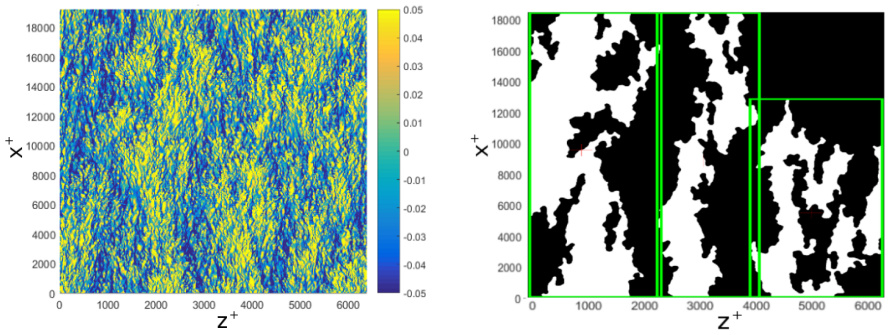
Each binary object resulting from image processing is characterised in terms of centroid, perimeter, and contour coordinates. This information is relevant to determine sub-images which can be used as samples for two-dimensional correlation with wall-parallel planes in the logarithmic and outer regions. Calculation of morphological properties is performed through Gaussian mixture models (GMMs) for each binary component. GMM is defined as parametric probability function coinciding with a weighted sum of Gaussian densities [Reynolds, 2000]. GMMs are helpful in modelling the probability distribution of continuous measurements, such as contours of binary components in image processing or properties related to the vocal-tract spectrum [Reynolds and Rose, 1995, Reynolds et al., 2000, McLachlan, 1988][5].

[5]Readers are referred to Sect. A.1.2 for further details on the Matlab code produced to generate near-wall regions of interest.



(a) (b)

Figure 3.3.1: Identification of near-wall hairpin imprints. Original velocity fluctuations (a), and processed binary samples (b) at $y^+ = 1.4$. $Re_\tau = 1025$.



(a) (b)

Figure 3.3.2: Identification of near-wall hairpin imprints. Original velocity fluctuation (a), and processed binary samples (b), $y^+ = 2.0$. $Re_\tau = 1600$.

3.3.2 Results

As a result of the application of Gaussian mixture models (GMMs), existing binary objects are fully defined in terms of their perimeter, contour, and location of their centroid. This allows producing sub-samples in the viscous sub-layer which can be correlated with full two-dimensional data further away from the wall. Sub-images are produced and shown in green rectangles tangent to contours of each large scale binary object (Figs. 3.3.1 and 3.3.2) and very few large-scale objects are extracted as samples for two-dimensional correlation.

In summary, the present section has introduced the use of Gaussian Mixture Models (GMMs) to characterise large-scale objects resulting from the image processing. Near-wall regions of interest have been statistically identified in terms of perimeter, contour coordinates, and centroid. The above information is crucial to generate the near-wall samples for two-dimensional correlation with the logarithmic and outer regions[6].

3.4 Object recognition

3.4.1 Introduction

As previously reported in Chapt. 2, correlation between the near-wall and outer regions of turbulent layers has been demonstrated through a physical model [Choi, 1989, Orlandi and Jimenez, 1994], according to which a large three-dimensional structure can induce a persistent ejection of near-wall streaks and low-speed fluid away from the wall. Near-wall streaks are particularly relevant for the sustenance of the turbulence cycle, due to their instability and break-up processes which result in intermittent eruptions of fluid, named as sweep-ejection events. In this context, sweeps are regions of high-speed fluid which produce large skin friction while impinging on the wall. As a result of the model described above, Mathis and co-workers [Mathis et al., 2009, Mathis et al., 2011a, Mathis et al., 2013] have produced a correlation to predict the near-wall shear stress on the basis of modulation and superposition effects from the outer region.

As mentioned in Chapt. 1, this work is aimed at developing a methodology for real-time correlation between viscous sublayer and

[6]For details on the related Matlab code, readers are referred to Sect. A.1.2.

the outer region of a turbulent boundary layer, for which image processing and object recognition are believed to be the appropriate candidates.

Object recognition was implemented by making use of two-dimensional correlation, applied to binary images through the boundary layer thickness.

Following the image-processing stage described in Sect. 3.2 near-wall samples were extracted and compared with wall-parallel planes in the outer region, through two-dimensional normalised correlation function. This approach, is based on previous investigations suggesting that outer regions of low-speed fluid are flanked by agglomerations of hairpin vortices [Tomkins and Adrian, 2003, Adrian et al., 2000, Ganapathisubramani et al., 2003, Kim and Adrian, 1999].

3.4.2 Results

The procedure presented was preliminarily applied to low-momentum regions of fluid, or regions of negative velocity fluctuation, due to their characteristic streakiness being particularly appealing for image correlation.

This approach has been successful, since near-wall samples are univocally identified in the logarithmic and outer regions. Therefore, given a sample in the viscous sublayer, there will be only one homologous counter-part correlating further away from the wall. In this way, the methodology is helpful to detect hairpin vortices and their footprints.

In Fig. 3.4.1 it can be observed that three large-scale connected objects are identified in the viscous sublayer at $y^+ = 1.4$. Some of them are partially recognised, especially in the logarithmic ($y^+ = 49.7$) and outer regions ($y^+ = 180.0$). A minimum value for the two-

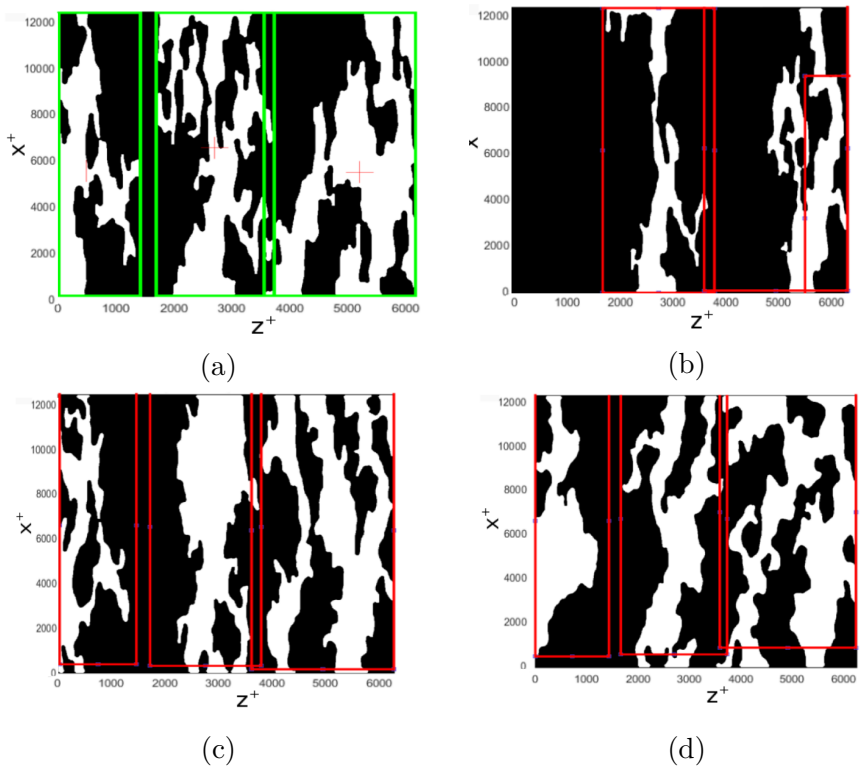


Figure 3.4.1: Object recognition. Near-wall samples at $y^+ = 1.4$ (a); Two-dimensional correlation at $y^+ = 13.5$ (b), 49.7 (c), and 180.0 (d). $Re_\tau = 1025$.

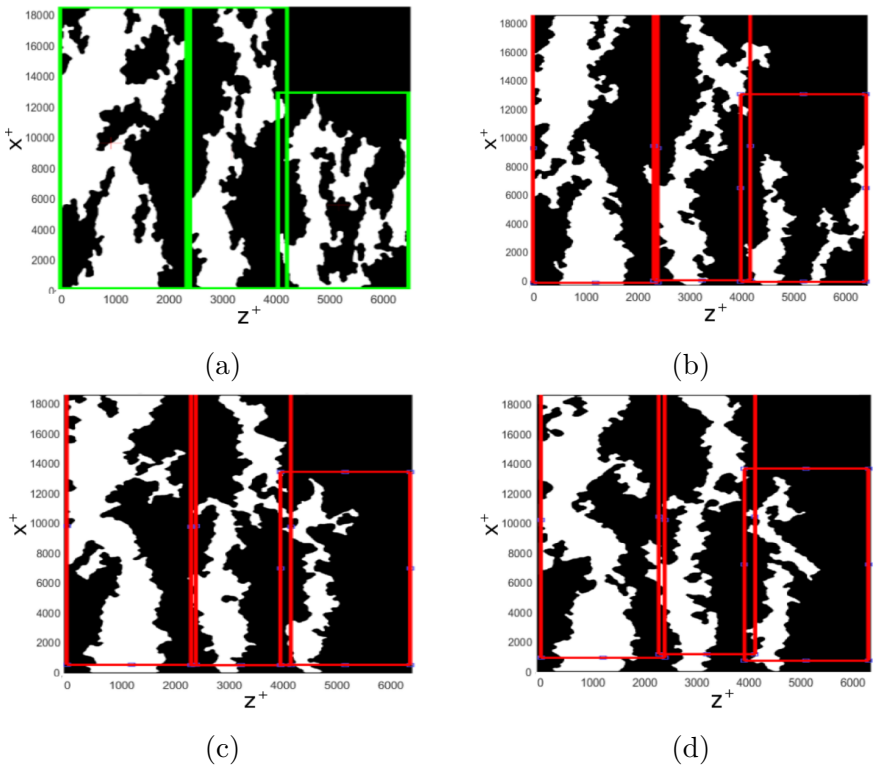


Figure 3.4.2: Object recognition. Near-wall samples at $y^+ = 2.0$ (a); Two-dimensional correlation at $y^+ = 60.0$ (b), 120.0 (c), and 200.0 (d). $Re_\tau = 1600$.

dimensional correlation coefficient has been chosen equal to 0.25, as a good compromise between robustness and rejection of regions whose contours are significantly different from their respective footprints. Therefore, outer objects with correlation lower than the prescribed value are discarded. Similar conclusions are confirmed at $Re_\tau = 1600$, as shown in Fig. 3.4.2. Additionally, as Reynolds number increases, binary contours seems to become rougher for given processing setup, this occurrence making image correlation more difficult.

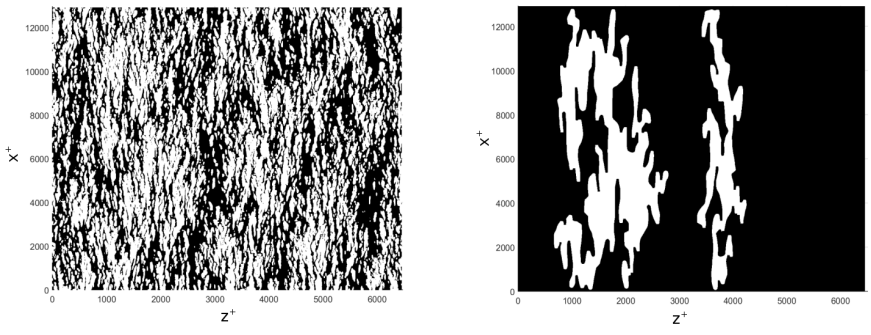
Therefore, in a future development of this work, the author suggests to refine the parametrical setup for median filtering, skeletonisation and morphological area opening, through an iterative algorithm which is based on the two-dimensional cross-correlation coefficient. In this way, the methodology can be applied to different Reynolds numbers.

In summary, this section has presented a method to potentially recognise hairpin vortices through two-dimensional correlation.
The approach was successfully applied to negative velocity fluctuations, due to their characteristic streakiness which makes them particularly suitable for pattern recognition, and their close relationship with hairpin vortices, which has been widely been demonstrated in the previous literature.

3.5 Analysis of high-speed motions

3.5.1 Introduction

The same methodology described in Sects. 3.2-3.4 was tested on high-speed regions of fluid. This is done to assess whether the image-processing approach is still applicable and whether the procedure detailed in Sect. 3.2.1 needs modifications to successfully detect outer coherent motions. Moreover, since high and low speed regions are normally next to each other, the former can still be used for detection of hairpin vortices.
From turbulence point of view, sweeps (associated with high-speed fluid) and ejections (associated with low-speed fluid) differ in their auto-correlation time. This evidence, firstly observed by Corino and Brodkey [Corino and Brodkey, 1969] and later supported by Wallace [Wallace et al., 1972], might explain the reason why momentum-deficit regions are streakier compared to their high-speed counterparts. This difference in morphology is evident especially in the near-wall region. Therefore, adjustments to the image-processing method described in Sect. 3.2 are needed when analysing regions of positive velocity fluctuation.

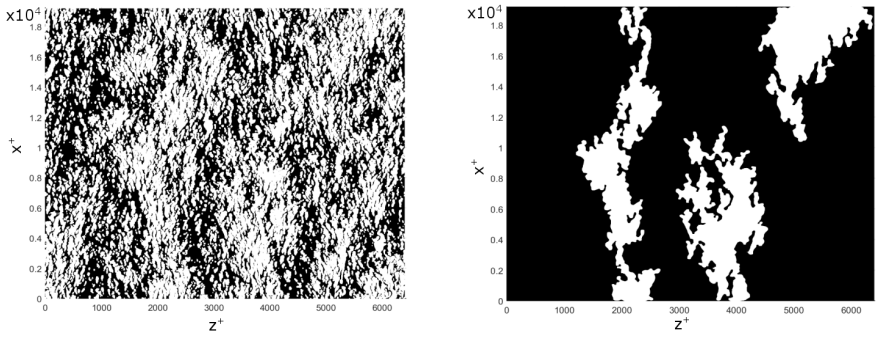


(a) (b)

Figure 3.5.1: Image analysis for high-speed motions. Unprocessed binary image (a) and processed with removal of skeletonisation and branching (b) at $y^+ = 1.4$. $Re_\tau = 1025$.

3.5.2 Binary Image Processing

As anticipated in Sect. 3.5.1, due to a different morphology between high and low speed regions of fluid, the method for image processing and pattern recognition need to be modified when considering high-speed motions. From a careful investigation, it emerged that skeletonisation and branching can compromise the overall method, especially pattern recognition. This is suggested from initial image-processing results, where small binary objects in the near-wall region - extending longitudinally over less that 1000 wall units - have been extracted. In this context, it is inferred that skeletonisation and branching can induce disaggregation of near-wall binary components. Adjustment of skeletonisation and branching parameters lead to large-scale objects in the viscous sublayer, as shown in Figs. 3.5.1-b, 3.5.2-b.



(a) (b)

Figure 3.5.2: Image analysis for high-speed motions. Unprocessed binary image (a) and processed image (with removal of skeletonisation and branching) (b) at $y^+ = 2.0$. $Re_\tau = 1600$.

3.5.3 Two-dimensional image correlation

Two-dimensional correlation was performed to identify outer coherent motions, based on large-scale samples in the viscous sublayer. Results have demonstrated that there is correlation for high-speed regions of fluid (Fig. 3.5.3). In fact, two large-scale connected objects, stretching all along the longitudinal direction, result from near-wall sampling; similar objects are recognised in the buffer, logarithmic and outer regions. However, the methodology developed and presented in this chapter needs parametrical modification when performed on high or low speed regions of fluid.

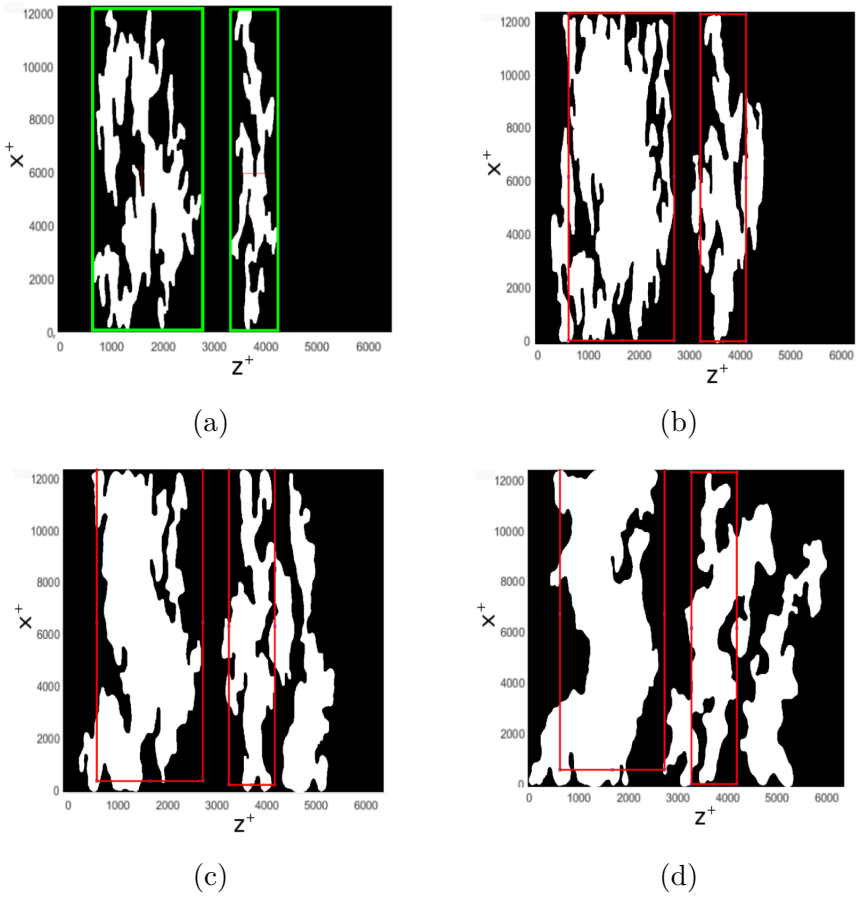


Figure 3.5.3: Object recognition for high-speed motions. Near-wall sampling at $y^+ = 1.4$ (a) and object recognition at $y^+ = 13.5$ (b), 49.7 (c), 180.0 (d). $Re_\tau = 1025$.

3.6 Summary

In summary, a novel strategy, based on image processing and two-dimensional correlation of wall-parallel planes of stream-wise velocity fluctuation, has been proposed to detect outer coherent motions in turbulent channels. The method makes use of velocity fluctuation maps inside the viscous sub-layer to directly correlate with the outer region.

From this investigation it emerged that:

1. **The methodology is particularly successful on large-scale low-speed regions of fluid.** This result might be due to the characteristic streakiness of regions of momentum deficit;

2. **The procedure needs adjustments when varying the turbulence regime.** In fact, large-scale binary objects seem to have rougher contours as Reynolds number increases;

3. **The procedure needs adjustments when treating high-speed regions of fluid.** In this way, image-correlation stage and the overall flow topology can be preserved.

The approach presented in this section can be further improved through an optimisation algorithm to automatically adjust the parametrical setup - based on comparison of image pairs and subsequent cross-correlation coefficient. In this way, the method presented in this chapter can be applied to a wide range of flow applications and turbulent regimes, including (as also mentioned in Chapt. 1) boundary layers on aircraft wings. In this view, image processing can be utilised for real-time recognition and disruption of outer coherent motions, finalised to turbulent drag reduction.

Chapter 4

Remote flow control by laser energy deposition

4.1 Introduction

As previously mentioned in Chapt. 1, the objective of the present work is to introduce a novel methodology in flow control to reduce turbulent skin friction drag. The above motivation is of great concern in aerospace applications, especially in subsonic air transportation, where turbulent drag can reach up to 45% of the overall aircraft resistance force. In this perspective, Sect. 2.3.1 has remarked the importance of hairpin vortices for remote disruption of the near-wall turbulence cycle.

In view of the above considerations, laser energy deposition (LED) is attractive, due to the following reasons:

1. **Laser radiation can travel in air at the speed of light.** This feature ensures a fast response;

2. **Laser light is space-coherent.** Therefore, the laser beam can be focused into a small volume of interest. This property is

fundamental for energy deposition to create a desired localised flow perturbation;

3. **Laser light is time-coherent.** This characteristic allows tuning the energetic content of a laser beam through its wavelength.

As earlier detailed in Sect. 2.3.2 laser energy deposition has been particularly successful for flow control in supersonic flows. In fact, the physical effect of LED a blast shock wave which is followed by formation of plasma and fluid roll-up [Jiang et al., 1998, Ghosh and Mahesh, 2008, Schulein and Zheltovodov., 2008]. These phenomena can effectively interrupt Edney IV interactions in front of blunt bodies [Adelgren, 2003, Adelgren et al., 2005] which are responsible for sharp heat fluxes at the wall. Normally, the flow disturbance produced by energy deposition evolves over a time slot of few tens of microseconds, which is helpful in supersonic and hypersonic regimes. However, this fact can represent a limit in subsonic flows, where hairpin vortices can persist longer than the characteristic time of flow actuator.

In view of the above considerations, this work explores laser energy deposition as a trigger to induce:

(a) **Local ignition of bubbles filled with flammable mixtures.** Air-butane and air-hydrogen mixtures are compared;

(b) **Localised sublimation of carbon-dioxide solid particles.**

At present time, this research has not been investigated elsewhere. Therefore, the preliminary study which is presented in this dissertation consists of a test rig where the effects on the local flow field are observed in quiescent air. However, developments of this approach can find application in aerospace industry, especially in flow control

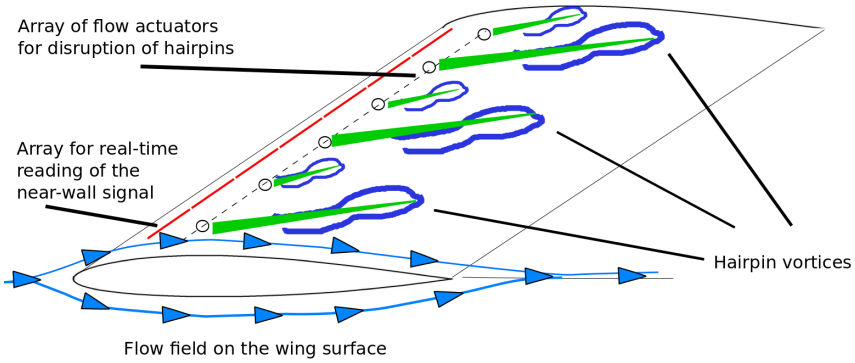


Figure 4.1.1: Sketch of a potential application of a energy deposition in aviation.

over a wing surface in subsonic regime. In fact, as a further comparison of energy deposition with other methods, flow actuators can be placed along the wing span inside its own structure (Fig. 4.1.1). Therefore, a dual advantage consists of not having moving parts and the absence of a physical body which would interfere with the flow field (e.g. the thickness of a DBD plasma actuator fixed across a surface).

By contrast, a challenging point is the controllability of laser beams. However, this problem seems it has already been solved by some researchers [Saito et al., 2008, Ochiai et al., 2016] through the use of three-dimensional scanning systems for real-time control of the laser focus location[1]. Another question is the location of injection of bubbles or carbon-dioxide particles in a real aircraft, to be actuated at the wing surface. Therefore, the above considerations give food for mind before a real commercial development of such a remote flow actuator can be put into practice.

An additional consideration is the way how hairpin vortices change

[1]Three-dimensional scanning systems are used for image display [Saito et al., 2008, Ochiai et al., 2016].

at high Reynolds numbers, such as on aircraft wings in subsonic flow. Recent studies shown in Chapt. 2 infer that a turbulent boundary layer at high Reynolds number presents hairpins widely spread across, while their typical signature at low regimes is not confirmed. All the above considerations suggest that there are significant obstacles before this novel technology can be practically applied on a aircraft wing.

This investigation of energy deposition makes use of particle image velocimetry (PIV) in quiescent air (Sect. 4.5) to demonstrate that ignition of flammable bubbles and sublimation of carbon-dioxide particles induced by laser energy deposition are promising for manipulation of coherent motions.

4.2 Particle image velocimetry

4.2.1 Introduction

Particle Image Velocimetry (PIV) is one of the most common optical techniques in fluid mechanics to quantify velocity, vorticity and pressure fields in two and three dimensional flows. Compared to other methods, such as hotwire anemometry (HWA), PIV is non-intrusive since it does not introduce any perturbations in the flow field. In fact, the flow field is locally illuminated through laser sheets (Fig. 4.2.1). Seeding particles are used as a medium to scatter laser light towards the camera sensor.
In order to achieve a good PIV acquisition, tracers should:

1. **Be neutrally buoyant.** Indeed, buoyancy can prevent particles to sink;

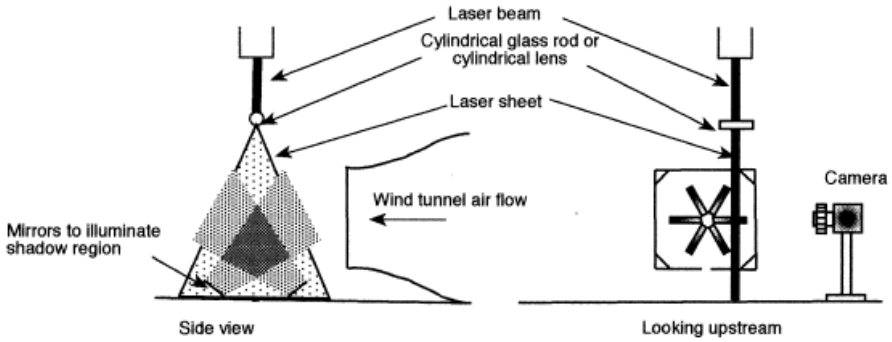


Figure 4.2.1: General PIV setup in a wind tunnel. [Grant, 1997].

2. Have a high scattering efficiency.

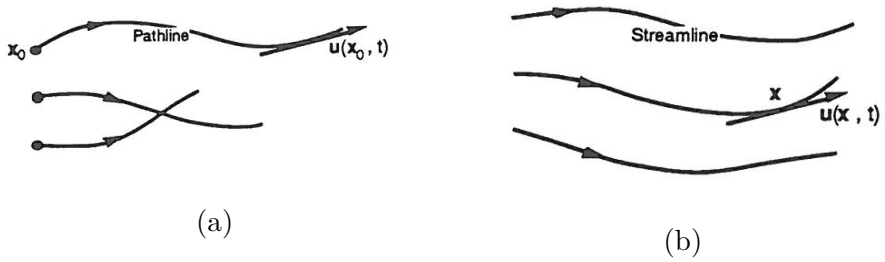
Therefore, flow visualisation is processed to extract information about the local flow field. Lasers are of particular interest to quantify particle displacements, since they are a source of stroboscopic light[2].

4.2.2 Description of fluid motion

Tracers motion is modeled based on Quantum mechanics theory, according to which fluid particles are infinitesimally small, but can be big enough to include a large number of molecules within their boundaries. Microscopic characteristics, such as number of moles and molar mass, define the fluid macroscopic properties, e.g. temperature, pressure, and density. Two approaches are available to describe the motion of fluid particles (Fig. 4.2.2):

(a) Lagrangian method. A single fluid particle is followed on its own motion. In other words, the local macroscopic properties depend on time t and initial position x_0 from where each single particle is released. Loci of fluid particles are termed

[2]In fact, light can be determined in terms of both repetition frequency and pulse duration.



(a) (b)

Figure 4.2.2: Lagrangian (a) and Eulerian (b) descriptions.

as *pathlines*. Since two different particles can be in the same position at different instants in time, pathlines can intersect each other.

(b) Eulerian description. Flow field properties are measured at fixed locations in space. Therefore, velocity and density are function of both time and space ($u = u(x,t)$, $\rho = \rho(x,t)$). The velocity field is differentiable, hence can be characterised by *streamlines*. Compared to pathlines, streamlines cannot intersect each other - except in presence of fluid sinks or sources.

Particle image velocimetry makes use of the lagrangian representation, as it is equivalent to a sensor grid acquiring the velocity field globally over time.

4.2.3 PIV parameters

Particle image velocimetry requires several parameters to be considered ahead of the experimental measurement, in order to reduce any biases during data processing:

(a) Seeding density, which can affect the overall flow behaviour. In order to assess the correct amount of particles per unit of volume, two characteristic volumes are defined (Fig. 4.2.3):

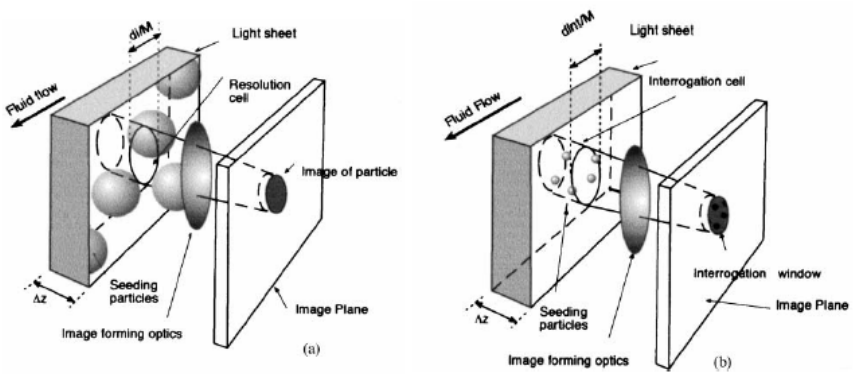


Figure 4.2.3: Resolution (a) and interrogation (b) cells, [Grant, 1997].

- The *resolution cell*, defined as the cylindrical volume achieved from the intersection between the light sheet and the cylinder obtained from the projection of a single particle in the image plane.
- The *interrogation cell*, which is the intersection between the illuminating sheet and the cylinder obtained as a projection of the interrogation area (IA) in the image plane. Cross correlation of interrogation areas is helpful to reconstruct the local flow field.

As a result, the number of tracers contained inside the resolution cell defines the *source density* (Eq. 4.1); whereas the number of particles inside the interrogation cell defines the *image density* (Eq. 4.2)[3].

$$N_s = \rho \Delta z \pi [d_I/2M]^2 \tag{4.1}$$

$$N_I = \rho \Delta z \pi [d_{int}/2M]^2 \tag{4.2}$$

(b) Image density, which determines the signal-to-noise ratio

[3]In Eqs. 4.1 and 4.2 ρ denotes the number of particles per unit volume and M is the magnification factor.

(SNR) in the peak of the cross-correlation function. A high number of particles per unit volume results in high SNR. However, speckle patterns can form, as a result of interference of scattered light. This occurrence ($N_I \gg 1$) is named *speckle image velocimetry*. By contrast, particle image velocimetry applies when $N_I \ll 1$.

(c) Spatial resolution, which is a function of the camera aperture f" and the laser wavelength λ, through the cone vertex angle α. The Rayleigh criterion determines longitudinal and transversal resolutions, respectively defined as $d_l \cong \lambda/\alpha^2$ and $d_t \cong \lambda/\alpha$.

(d) The depth of field (DOF), which is characteristic of the sensor lens and is defined as the thickness of the in-focus plane, i.e. the region where tracers are measured. Ideally, the light sheet and the in-focus plane should coincide for a good PIV acquisition. DOF can be approximated by $2F(1+1/M)^2 f"^2/10^6 M$ or $4(1+1/M)^2 f"^2\lambda$, being M the magnification factor and F the focal length [Grant, 1997].

(e) The image size, which is a function of the actual particle diameter d_P and the lens magnification factor M. In other words, when particles lie inside the depth of field, their geometrical diameter is given by $d_G = M \times d_P$.

The size of tracers should be a reasonable compromise between visibility, distribution and ability to follow the fluid along its motion. In other words, particles should be large to be visible, but not too large, as they might interact with the flow field through their mass, and induce velocity bias.

Stoke's number, St_v, is used to indicate whether particles can influ-

ence the flow field or vice versa; it is defined as the ratio between the particle response and flow characteristic times. Therefore, when $St_v \ll 1$, particles and fluid are in equilibrium; whereas the condition $St_v \gg 1$ suggests that particles will barely be influenced by fluid motion. Stoke's number can be determined from the dynamic equation of the motion of a spherical particle in a fluid, in the assumption that inertial forces can be neglected (Eq. 4.3)[4].

$$\frac{\pi d_P^3}{6}\rho_P\dot{\nu} = 0.5C_D\frac{\pi d_P^2}{4}\rho_F U^2 \tag{4.3}$$

Velocity bias are crucial, especially in shear and swirling flows, where external actions (e.g. centripetal forces) can prevent particles to follow the flow. In order to reduce bias and avoid particles to fall outside the illumination region within two exposures, the following criteria have been proposed [Grant, 1997]:

1. **High image density,** $(N_I > 10 - 20)$;

2. **In-plane displacements below one fourth of the size of the interrogation area.** In other words, $(u^2 + v^2)^{1/2}\Delta t < d_{int}/4M$ being u and v the two planar velocity components, Δt the time interval between the two exposures, d_{int} a characteristic dimension of the interrogation region, and M the magnification factor;

3. **Out-of-plane displacements below one fourth of the laser sheet thickness.** Displacement can be expressed by $w\Delta t < \Delta z/4$, being w the out-of-plane velocity component, and Δz the laser sheet thickness;

[4] d_P is the particle diameter, U is the relative velocity between the particle and fluid, ρ_P is the particle density and $\dot{\nu}$ is the particle acceleration.

4. **The ratio** $|\Delta u|/|u| < 0.2$**,** where Δu the velocity variation due to spatial gradients.

4.2.4 Analysis, validation and processing

Particle image velocimetry (PIV) is based on correlation of image pairs, acquired from the same plane of illumination. PIV analysis is composed of:

1. **Selection of the interrogation windows and image correlation;**

2. **Calculation of the displacement peak;**

3. **Computation of the resulting velocity field.**

The procedure above is repeated for each sub-image included in the field of view.

Some overlapping between adjacent sub-images can be expected. However, a satisfactory compromise between density of information and over-sampling can be achieved for a maximum overlapping equal to 50% [Hinsch, 1993]. Image correlation between interrogation pairs can be performed through convolution filtering or fast Fourier transform (FFT) (Fig. 4.2.4). In both cases the result is a probability density function map whose peak is a direct measurement of the particle displacement, hence its velocity[5].

The FFT approach precludes the transformation of each sub-image from real to complex domains, where a conjugate multiplication of the two frames is calculated and transformed back to the real domain through inverse FFT.

[5]Particle displacement is preliminarily obtained in pixels; after calibration, pixel displacement can be converted in spatial dimension (e.g. millimetres).

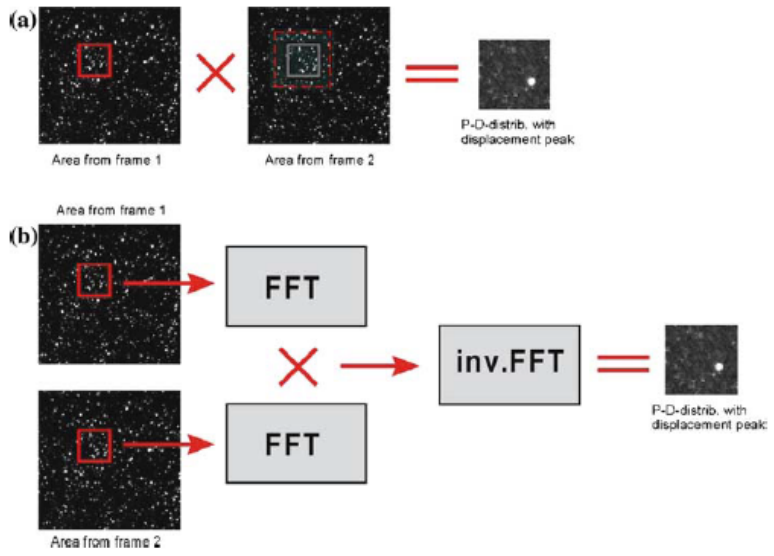


Figure 4.2.4: Cross-correlation performed by convolution(a) and FFT(b) approaches [Stamhuis, 2006].

By contrast, convolution describes more directly the image overlapping of different snapshots at the same location.

Finally, PIV processing includes validation, where wrong vectors (due to local variation in density seeding, over-illumination, or out-of-plane flows) are detected through standard deviation and substituted with local average values.

In summary, particle image velocimetry (PIV) has been presented in this section. Compared to other methods, such as hot-wire anemometry and pitot-tube, PIV is convenient as it does not introduce any perturbations in the flow field. Data are organised in the form of square (two-dimensional PIV) or three-dimensional matrices (e.g. tomographic PIV).

This technique has been implemented in Sect. 4.5 to measure the local flow expansion induced by laser energy deposition, when targeting flammable bubbles and carbon-dioxide particles in quiescent air.

4.3 Laser energy deposition in quiescent air - experimental setup

4.3.1 Introduction

This section presents the experimental setup prepared to demonstrate that laser energy deposition (LED) can successfully be implemented for disruption of hairpin vortices in subsonic flows. In more detail, LED has been used to trigger ignition of flammable bubbles and to induce sublimation of carbon-dioxide particles in quiescent air.

With regard to ignition, Morsi and co-workers [Morsy et al., 1999] have identified four physical mechanisms which can produce a flame kernel as a result of laser deposition:

- Thermal heating;
- Photo-dissociation;
- Resonant breakdown;
- Non-resonant breakdown;

This work has investigated *spark-induced ignition* which is regarded as non-resonant breakdown.

By contrast, sublimation of carbon-dioxide (CO_2) particles induced by LED has been explored, due to interesting flow expansion ratios of the order of 800 [Spur et al., 1999, Uhlmann et al., 2006]. Moreover, CO_2 particles are abundant in aircraft engines, in the form of exhaust gases, and safer than flammable chemicals. Therefore, CO_2 gas can be extracted and cooled down to -80^o Celsius (at atmospheric pressure) to obtain solid particles.

In summary, three different mechanisms induced by laser energy deposition have been explored in this research:

1. Ignition of bubbles filled with air-hydrogen mixture;

2. Ignition of bubbles filled with air-butane mixture;

3. Sublimation of carbon-dioxide particles.

4.3.2 Setup

Setup is resumed in Fig. 4.3.1. Tests in quiescent air have been conducted in a chamber of size equal to 200×200×100mm. A support is placed inside the chamber, where bubbles filled with flammable mixtures or carbon-dioxide particles are placed.

Bubbles have been produced by blowing flammable mixtures directly inside the test chamber near the focal point of the pulsed laser beam. The same consideration applies to CO_2 particles.

The experimental setup included:

(a) LDY-302 PIV Litron system. This laser is used to generate a green laser sheet at 532 nano-meters for PIV measurements. A good compromise in terms of light intensity and safety of the camera sensor is represented by setting the power level equal to 55%. This applied especially in the case of carbon-dioxide particles which are characterised by a high surface reflection coefficient;

(b) Quantel pulsed Nd:YAG laser, Twins and Brilliant model. This laser, reaching an energy level up to 160 milli-Joules per pulse and running at a repetition rate of 10 Hertz, has produced

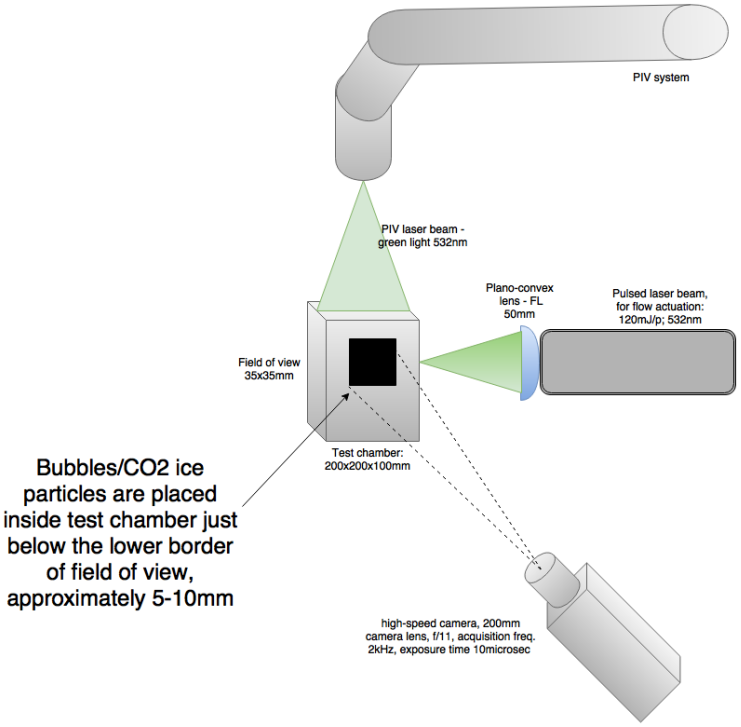


Figure 4.3.1: Experimental setup for laser energy deposition in quiescent air.

green coherent light at 527 nanometers. Furthermore, a 50 millimiter plano-convex lens has been used to focus the pulsed laser beam in a small spot and to facilitate energy deposition;

(c) **Speed-Sense 9060 camera sensor, for high-speed PIV recording.** Acquisitions were taken in a range of frequencies between 1 and 5×10^3 Hertz. In order to prevent sharp light intensity towards the sensor, the camera aperture can be set at f"/11, coupled with a 200 millimiter lens.

(d) **BNC-575 pulse generator.** This device is used to synchronise the PIV system, which includes camera sensor and laser, with the pulsed laser for flow control. Pulsed generator is used for two main reasons:

- To determine the time evolution of flame kernels from the

first laser pulse responsible of ignition;

- To protect the camera sensor from unwanted reflections from the pulsed laser, during PIV acquisitions. In fact, lasers Q-switch and flash-lamp times, and PIV synchronisation time can be adjusted for this purpose.

Furthermore, the pulsed laser is set in external mode[6]. For details on how to adjust flash-lamp and Q-switch triggering signals, readers are referred to the manufacturer[7].

PIV analysis has been conducted by using Dynamic Studio software[8]. Adaptive PIV methods are implemented to optimise size and shape of each interrogation area (IA), for a better correspondence with local seeding density and flow gradients. The minimum and maximum values for interrogation areas have been set to 8×8 and 64×64 pixels. Signal-to-noise ratio has been fixed to the default value of 4.0 to validate the correlation peak in each interrogation area.
In addition, moving average validation (MAV) method has been applied to data obtained from Adaptive PIV. MAV consists of substituting invalid vectors with the averages computed from the surrounding cell. For this study, a cell of 5×5 elements has been chosen as a reasonable compromise between spatial resolution and discrepancy of the bias vector from surrounding neighbours.

4.3.3 Time synchronisation

Synchronisation between PIV system and pulsed laser is fundamental to regulate the camera shutter and assess the initial point in

[6]For further clarification, the author uses the term '*pulsed laser*' to indicate the system used for flow control.

[7]`https://www.quantel-laser.com/en/customer-support-faq.html`.

[8]`https://www.dantecdynamics.com/dynamicstudio`

time where the pulsed laser beam is fired.

Three key parameters are identified to control the synchronisation of PIV and pulsed laser systems:

(a) **PIV acquisition rate,** which regulates the time gap between two consecutive peaks of the signal triggering the PIV system. An increment in the acquisition frequency results in an increase of the number of peaks per unit of time, hence a greater number of images acquired per second;

(b) **Camera exposure time,** which should be small enough to avoid the camera shutter to be open while the pulsed laser is fired (usually this parameter is set to 10 microseconds);

(c) **Time delay between flashlamp and Q-switch signals of the pulsed laser.** This parameter regulates the power output, since it controls the time interval during which laser light is amplified inside the resonating cavity. This value has been tuned between 160 and 180 milliseconds.

The pulse generator is fundamental to drive:

- PIV timer box;
- Laser flashlamp (pulsed laser);
- Q-switch signal from the pulsed laser.

A sketch on the implementation of the pulse generator is shown in Fig. 4.3.2.

In summary, this section has presented the experimental setup to quantify the ignition of bubbles filled flammable mixtures, and sublimation of carbon-dioxide particles. Synchronisation is crucial to

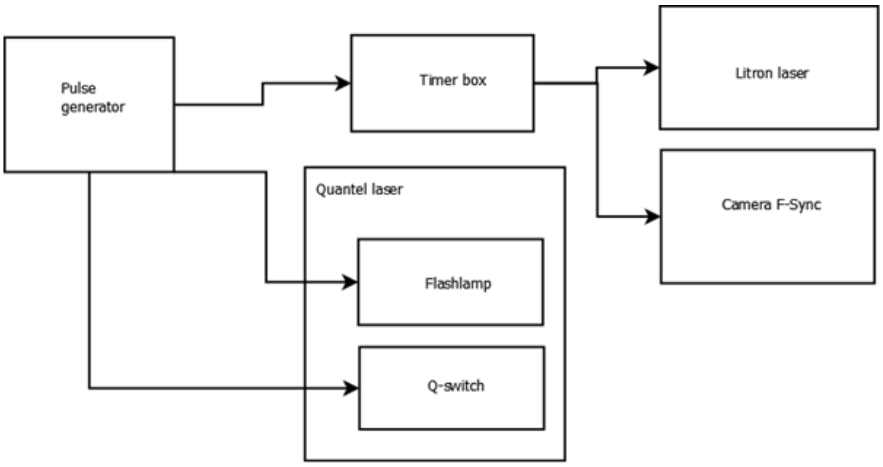


Figure 4.3.2: Synchronisation of the PIV system with the pulsed laser for flow control.

determine the timescale of the physical phenomena involved, hence the actuator response.

4.4 Evolution on time for ignition

4.4.1 Introduction

The aim of this section is to understand the physics of ignition triggered by laser energy deposition (LED) in quiescent air. A key parameter is the time interval between the laser pulse and the formation of a flame kernel. In other words, the response of the flow actuator here considered (LED) is assessed through instantaneous measurements of the flow field to determine whether hairpin vortices can actually be targeted and disrupted.
Kernels of flammable bubbles placed near the laser focus are observed. High-speed recordings support the idea of three different time slots describing the evolution of flames:

- t_{kern}, i.e. the time gap between the laser pulse and the appearance of the flame kernel;

- t_{exp}, i.e. the point where the kernel has achieved its maximum size;

- t_{ign}, i.e. the overall ignition time, until the flame kernel is completely extinguished.

Repeated measurements show that the overall ignition time for bubbles filled with air-butane mixtures is at least one order of magnitude larger than air-hydrogen bursting time. Furthermore, flow visualisation underlines a different pattern in the flame kernel during ignition, attributed to their chemical composition.

4.4.2 Progression of ignition processes

As explained in Sect. 4.4.1, the assessment of the evolution in time of flame kernels is relevant for the development of a remote flow actuator. In this way, the actuator time response can be estimated to achieve effective disruption of hairpin vortices.
For the purpose above, the following considerations about setup apply:

(a) **PIV system and pulsed laser for flow control are synchronised.** In this way, the camera sensor can catch any spots produced by the pulsed laser;

(b) **The time delay between the pulsed Q-switch signal and PIV timer-box trigger is set to 0 milliseconds; whereas camera exposure is fixed to 500 milliseconds**[9]. Therefore, the initial point in time for ignition - i.e. when pulsed laser has been fired - is known;

(c) **A green-light filter is placed in front of the camera sensor.** This is done in order to reduce the laser light intensity;

(d) **No PIV seeding is introduced in the flow field.** In fact, the only purpose here is to observe the evolution of flame kernels.

As a result, high-speed recordings show that the total ignition time is of the order of 260 milliseconds for air-butane mixtures (Fig. 4.4.1). The ignition process is explained in the following points:

- At t = 0 milliseconds the laser is fired and a small spot corresponding to the laser focus is visible for 2 milliceconds;

[9]The time gap between two consecutive pulses is equal to 100 milliseconds. This is because the repetition frequency of the pulsed laser is equal to 10Hz.

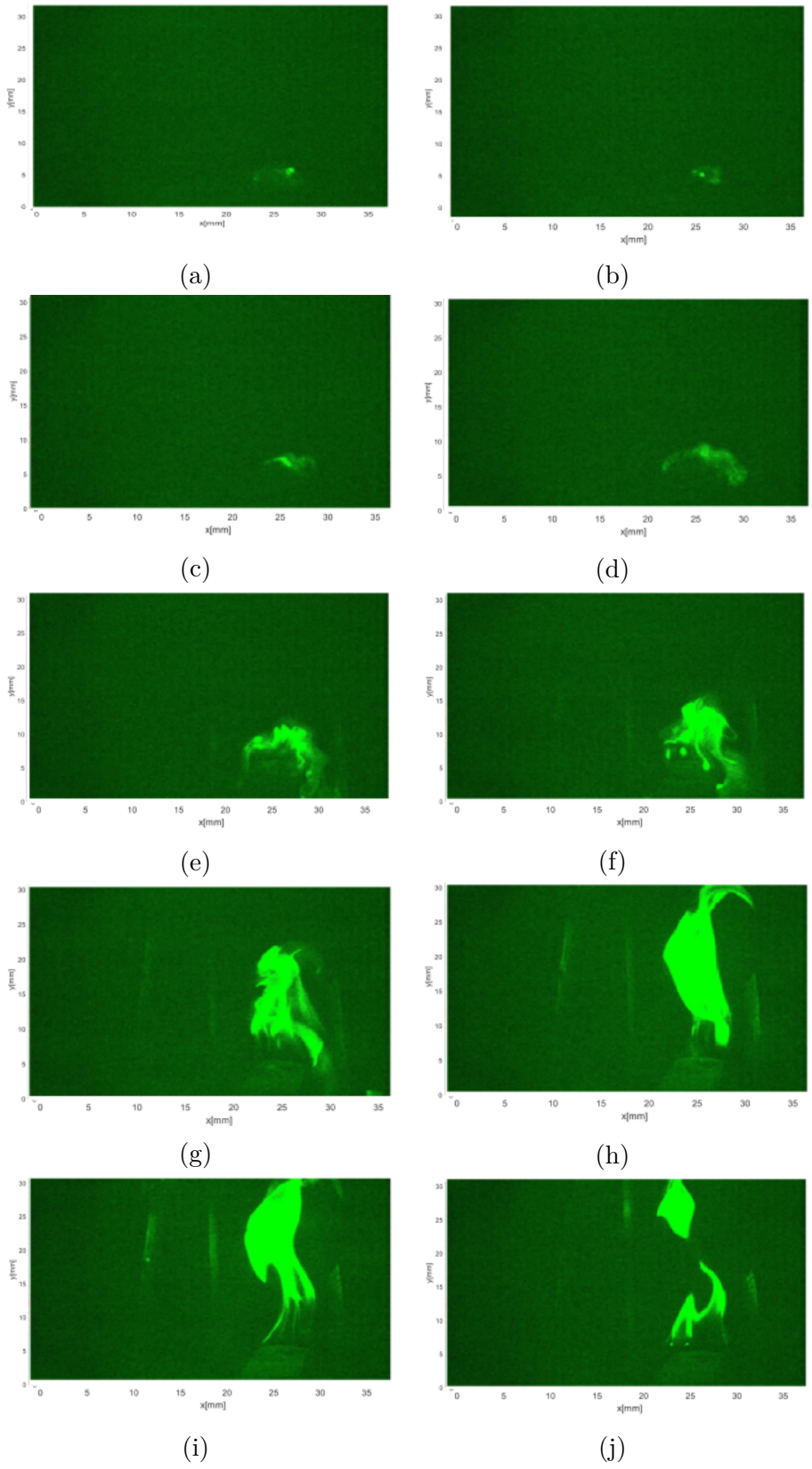


Figure 4.4.1: LED-induced ignition of static butane bubbles. $t = 0$ (a), 15 (b), 21 (c), 35 (d), 65 (e), 90 (f), 140 (g), 205 (h), 220 (i), 260 (j) milliseconds. Acquisition rate: 1kHz.

- At t = 6 milliseconds a region emitting light can be seen in the neighbourhood of the laser spot. This region is the flame kernel of the mixture.

- At t = 40 milliseconds the flame kernel has reached nominal diameter of the order of 20 millimiters; a mushroom-like structure has appeared;

- Beyond t = 90 milliseconds, the kernel shape develops vertically, while combustion process becomes weaker and weaker until the flame was eventually extinguished at t = 260 milliseconds.

By contrast, the life time of a flame kernel for air-hydrogen mixtures is of the order of 20 milliseconds, i.e. more than one order of magnitude shorter (Fig. 4.4.2). Compared to air-butane mixtures, the kernel is estimated to start at 1.2 milliseconds from the laser pulse and reaches its maximum size at roughly 3.8 milliseconds. Beyond this point combustion decays until the flame is extinguished at about 20 milliseconds.

In brief, this section has attempted at quantifying the time response of a potential LED actuator based on the evolution of a flame kernel for air-butane and air-hydrogen mixtures. Laser energy deposition was applied to bubbles filled with the two respective mixtures. Results show that air-hydrogen mixture has a response time which is one order of magnitude smaller than air-butane. As already remarked, at this stage of the analysis, the response time was evaluated based on the maximum size of flame kernels, which in the case of hydrogen is below 5 milliseconds from the laser pulse. This preliminary investigation suggests that ignition of air-hydrogen mixtures can potentially be attractive for remote disruption of hairpin vortices in subsonic flows.

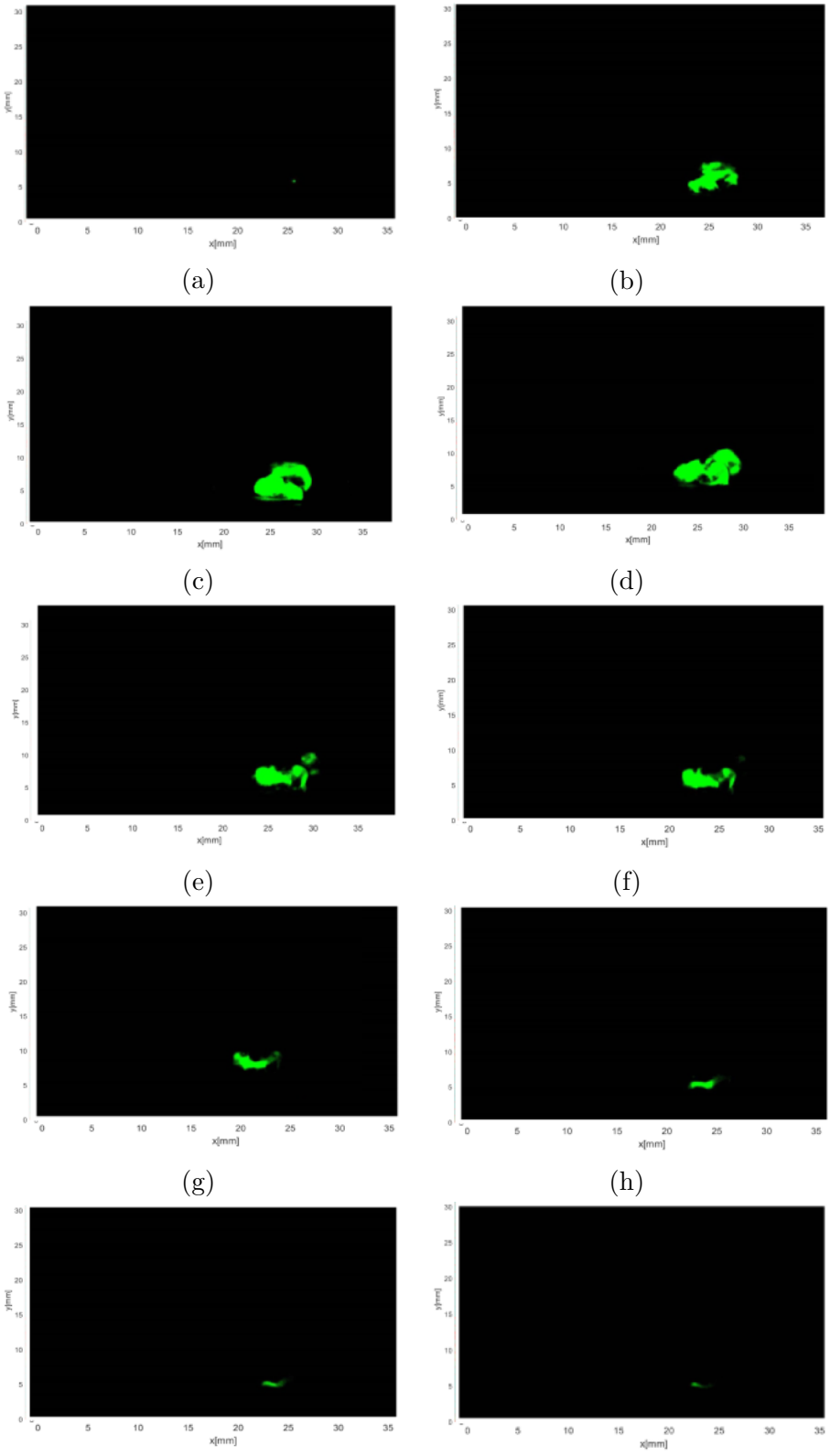


Figure 4.4.2: LED-induced ignition of static air-hydrogen bubbles. $t = 0$ (a), 1.4 (b), 1.8 (c), 3.8 (d), 5.4 (e), 6.2 (f), 8.0 (g), 12.0 (h), 14.0 (i), 20.0 (j) milliseconds. Aquisition rate equal to 5 kHz.

4.5 Quantification of LED-induced flow perturbations

4.5.1 Introduction

As previously mentioned in Sect. 4.1, laser energy deposition is used in this work to induce ignition of flammable bubbles and sublimation of carbon-dioxide particles. Bubbles and light particles are particularly helpful as they can be floating in air without affecting the overall flow field. In this way, a local flow perturbation can be remotely originated from the near wall region in order to disrupt hairpin eddies in a turbulent boundary layer.
Sect. 4.4 demonstrates that ignition of bubbles filled with air-hydrogen mixture is encouraging, since the flame kernel can reach its maximum size within the first few milliseconds from the laser pulse being fired. This result is relevant since this time scale can be potentially appropriate for subsonic air transportation to disrupt the turbulence near-wall cycle (Sect. 4.1, Fig. 4.1.1).

This section goes in deeper detail compared to Sect. 4.4, as PIV measurements are conducted to quantify the local flow expansion produced by energy deposition. Three cases are examined:

(a) LED-induced ignition of air-hydrogen bubbles;

(b) LED-induced ignition of air-butane bubbles;

(c) LED-induced sublimation of carbon-dioxide particles.

Experimental testing is conducted for the case of quiescent air in order to both have an estimation of duration and expansion rate of the flow perturbation, hence, to describe the dynamic response of

the remote flow actuator.

In view of the application of flow control on aircraft wings, the three approaches above have both advantages and disadvantages:

1. **Bubbles filled with air-hydrogen mixtures are convenient due to their buoyancy.** Therefore, the capability of floating in air depends on the low molecular weight[10];

2. **Actuation of flammable bubbles and the use of high-power lasers must adhere to safety regulations.** Laser light and the use of flammable gases onboard can be relatively hazardous;

3. **Carbon-dioxide is abundant in aircraft, especially from the engine burning chamber.** However, a close-loop circuit should be developed so that gas is cooled down to its solidification point (-80^o);

4. **Carbon-dioxide particles are not flammable.** This characteristic makes the method safer compared to flammable bubbles;

5. **Carbon-dioxide particles are relatively heavier than air molecules.** However, this circumstance might not be confirmed at cruise altitudes, where pressure and temperature are lower than sea level.

Having considered the above pro and cons, the main intent in this work is to assess perturbation and time scale for ignition and sublimation, in view of a potential application for turbulent boundary layers.

[10] `http://www.engineeringtoolbox.com/molecular-weight-gas-vapor-d_1156.html`.

4.5.2 Air-hydrogen bubbles

Results from PIV measurements on bubbles filled with air-hydrogen mixture in quiescent air are presented in this section. Due to the practical challenge of reproducing the same exact experimental conditions in each test case and most important the fact that this study focuses on the instantaneous effect of energy deposition in air, flow snapshots are taken into account for each methodology.

Flow visualisation at 2kHz rate (Fig. 4.5.1) shows a stack of bubbles in the proximity of the laser focal point which is disrupted at about 2.0 milliseconds from the initial time the laser is fired. Meanwhile, a sequence of subsequent bursts takes place and ends at about 20.0 milliseconds from the laser pulse, in agreement with the flow visualisation of flame kernels in Fig. 4.4.2.

In comparison with tests presented in Sect. 4.4, this time no filter is mounted on the camera sensor, so that seeding particles can be processed for PIV. This setup, led to a practical challenge of reducing the light intensity to the camera sensor, in order to obtain a more accurate resolution and avoid errors during PIV data processing. Therefore, the author suggests, for a future development of this experiment, the use of fluorescent particles for PIV coupled with a particular filter to block light reflections due to flames and laser beams, while allowing particles being observed for PIV processing. This is believed to be the only way to by-pass the issue in the measurement. It is remarked that PIV results are affected from the experimental setup, which has been prepared at best. However, maps of velocity magnitude shows non-physical regions which are attributed to the strong light reflections during ignition and the lack of an appropriate filter in the setup to reduce these. Having precised

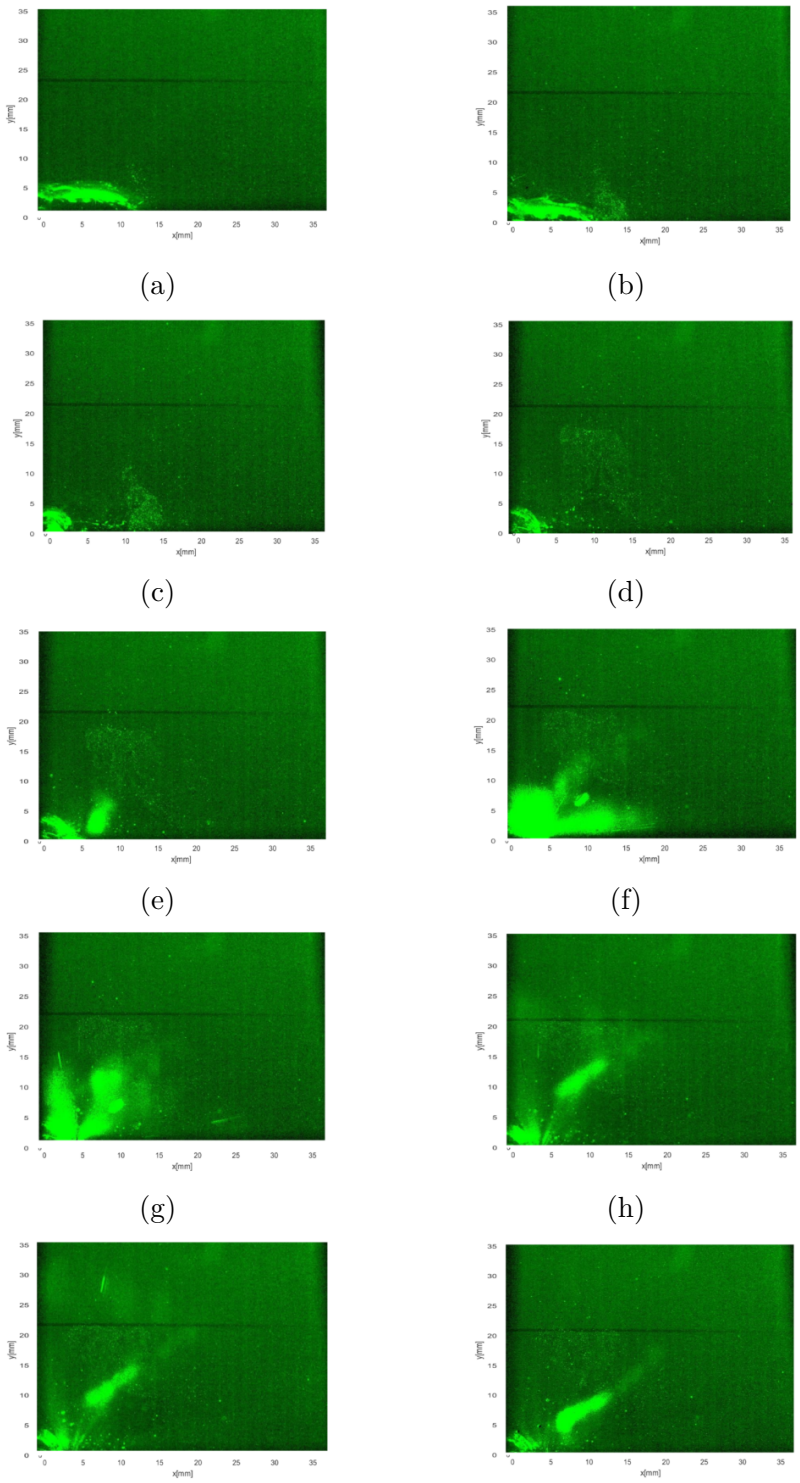


Figure 4.5.1: LED-induced bursting of hydrogen bubbles. t= 0.0 (a), 2.0 (b), 3.0 (c), 11.5 (d), 13.0 (e), 16.5 (f), 17.0 (g), 18.0 (h), 18.5 (i), 20.0 (j) milliseconds. Acquisition rate equal to 2 kHz.

this, instantaneous PIV measurements show evidence of a region of fluid quickly expanding (within the first few milliseconds from the laser pulse), which at this stage suggests the possibility of a vertical fluid ejection persisting for 7.5 milliseconds from the laser pulse (Fig. 4.5.2). This observation seems to be in agreement with the flame expansion in Sect. 4.4. Furthermore, considering the size of the field of view (35×35 square millimiters), the author asserts that the jet produced from the ignition of air-hydrogen bubbles can potentially have speed of the order of 10.0 meters per second (locally in time).

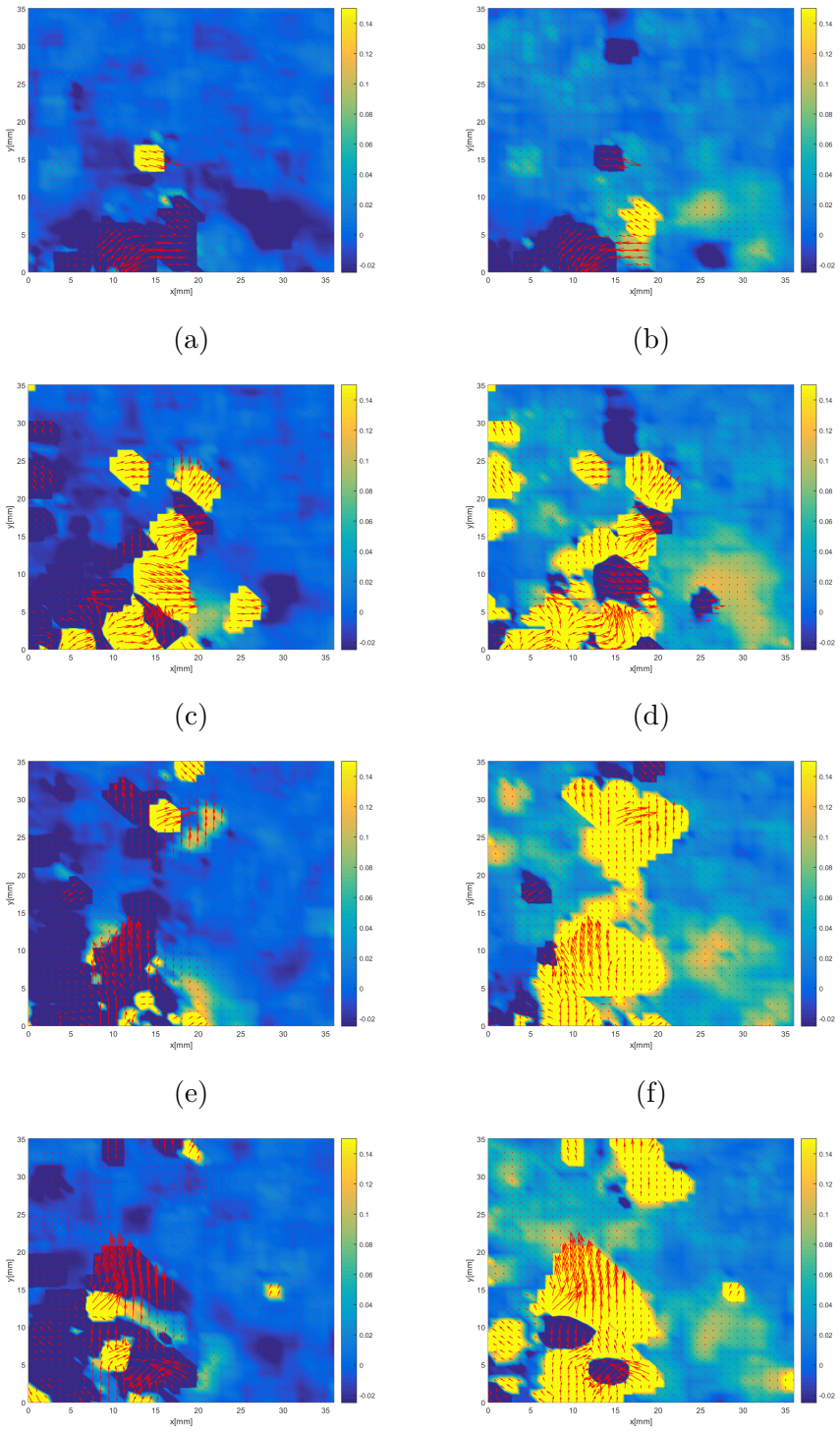


Figure 4.5.2: LED-induced bursting of hydrogen bubbles. Snapshots of instantaneous horizontal (left) and vertical (right) velocity components. t= 0 (a, b), 2.5 (c, d), 5.0 (e, f), 7.5 (g, h) milliseconds.

4.5.3 Air-butane bubbles

Ignition of bubbles filled with air-butane mixture differs from the hydrogen case. In fact, flow visualisation 4.5.3 show evidence of a large flame kernel expanding in all directions. Here again, the author recommends the use of fluorescent particles for PIV tracking in order to prevent errors during PIV processing by blocking light reflections by using a filter, specific for the wavelength of light emitted by flames. Having remarked the above point, flow visualisation seems to suggest that the flame expands in a time slot of approximately 90 milliseconds. Therefore, similar considerations to the hydrogen case lead to suggest a fluid ejection of the order of 0.5 meters per second - i.e. less than 1/20 of the transient for the jet produced by the air-hydrogen mixture. However, the above result is in disagreement with observations of flame kernels in Fig. 4.4.1 where the maximum expansion was achieved within approximately 45 milliseconds from the laser pulse. For these reasons, the author recommends further experimental measurements, in order to establish the effect of ignition of air-butane bubbles. PIV measurements are affected from the lack of a filter to appropriately block the light reflections resulting from the flame kernel. However, maps of velocity components in Fig. 4.5.4 have captured the formation and expansion of the flame border under which there is a region which should not be confused with low-speed velocity. It is rather a region where PIV setup has not achieved any velocity field since light reflection from PIV trackers was challenging. The flame expands across the whole field of view in the vertical direction within approximately 85 milliseconds from the laser pulse.

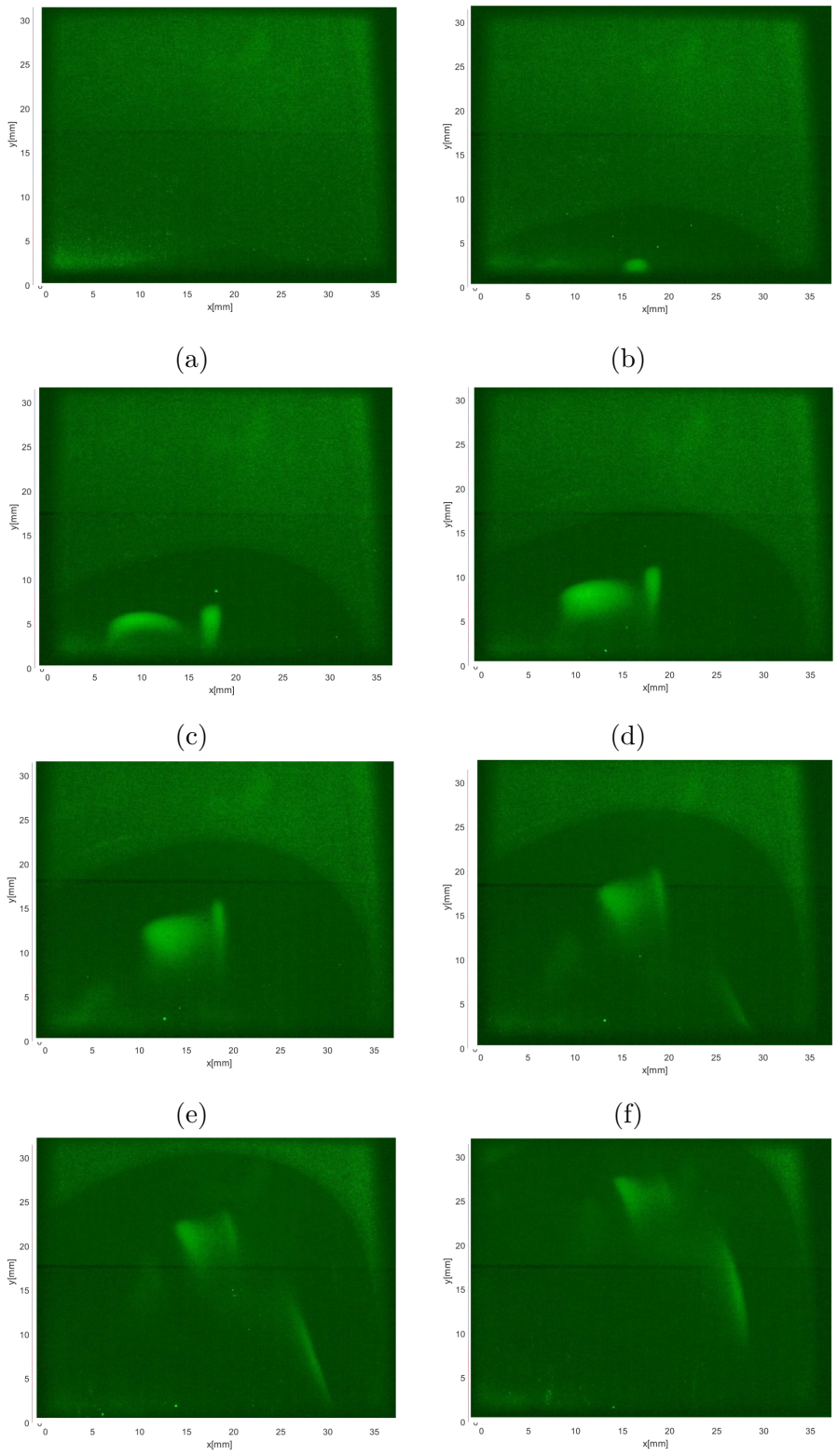
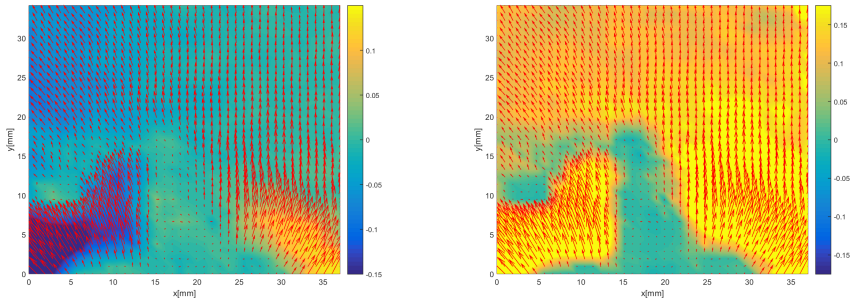
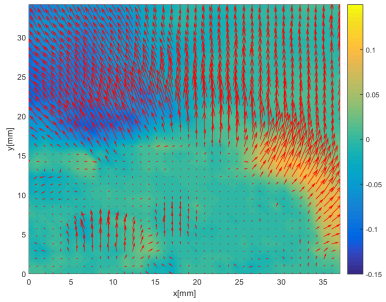


Figure 4.5.3: LED-induced ignition of air-butane bubbles. Flow visualisation. t=0.0 (a), 12.5 (b), 25.0 (c), 37.5 (d), 50.0 (e), 62.5 (f), 75.0 (g), 87.5 (h) milliseconds.

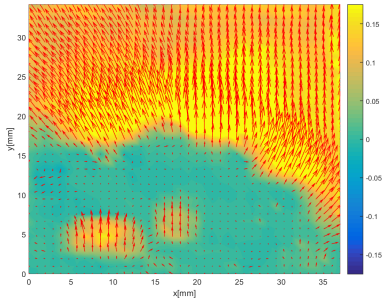


(a)

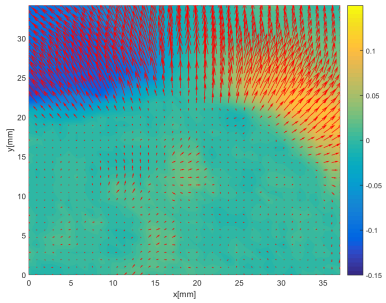
(b)



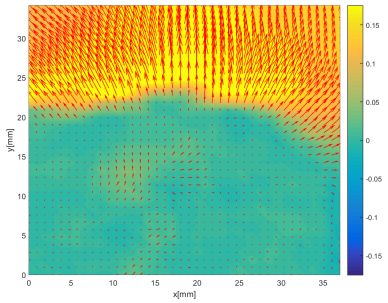
(c)



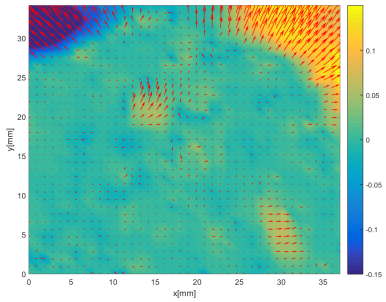
(d)



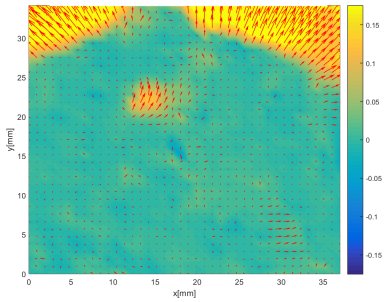
(e)



(f)



(g)



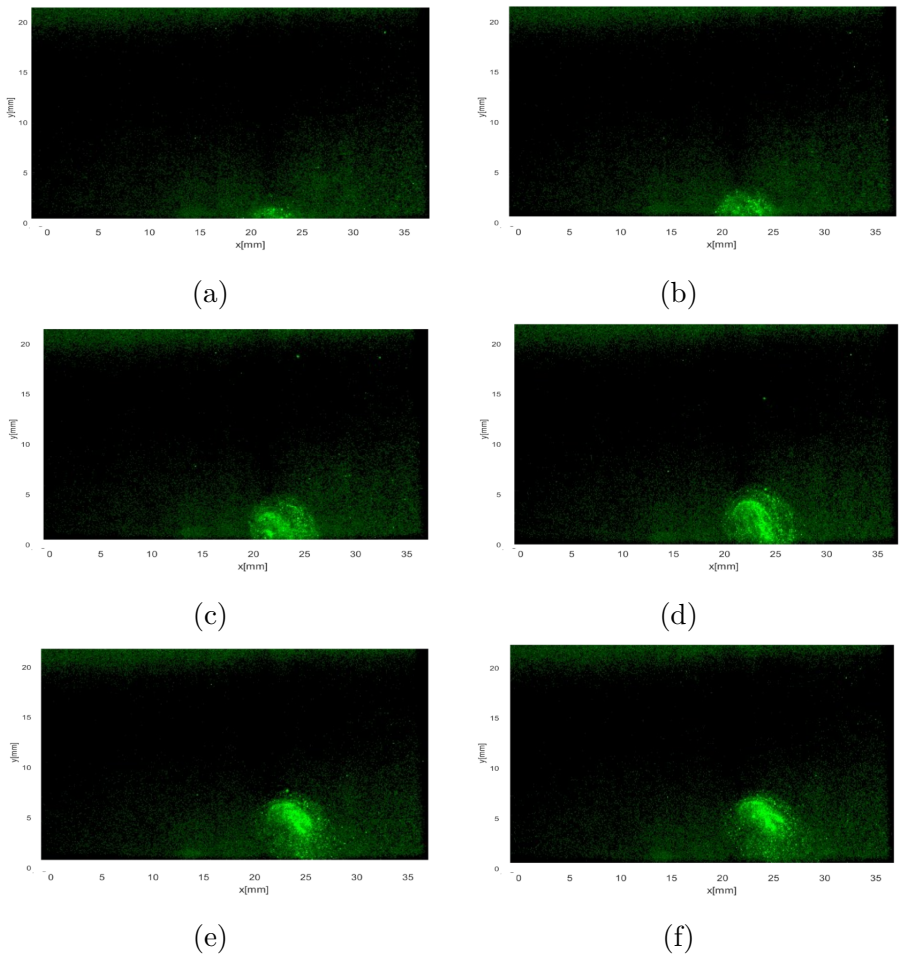
(h)

Figure 4.5.4: LED-induced ignition of butane bubbles. Snapshots of instantaneous horizontal (left) and vertical (right) velocity. t = 20.0 (a, b), 40.0 (c, d), 65.0 (e, f), 85.0 (g, h) milliseconds.

4.5.4 Sublimation of carbon-dioxide particles

Sublimation of carbon-dioxide particles has been captured again through PIV measurements. This time, the main challenge was the light reflection of the PIV laser beam into the dry ice. However, instantaneous PIV measurements have shown a jet whose duration, response and intensity are different from ignition of air-hydrogen and air-butane mixtures. Firstly, flow visualisation (Fig. 4.5.5) shows a region of fluid expanding and reaching its maximum size (5-10 millimiter in diameter) roughly at 40.0 milliseconds from the laser pulse.

Secondly, instantaneous PIV measurements show evidence of a jet whose maximum intensity is of the order of 0.05 meters per second (Figs. 4.5.6 and 4.5.7). In other words, the intensity of jets produced by sublimation is approximately two hundred times lower than the jet produced through ignition of air-hydrogen bubbles.



(a) (b) (c) (d) (e) (f)

Figure 4.5.5: LED-induced sublimation of CO_2 ice. t = 0.0 (a), 5.0 (b), 15.0 (c), 25.0 (d), 40.0 (e), 45.0 (f) milliseconds. Aquisition rate: 1kHz.

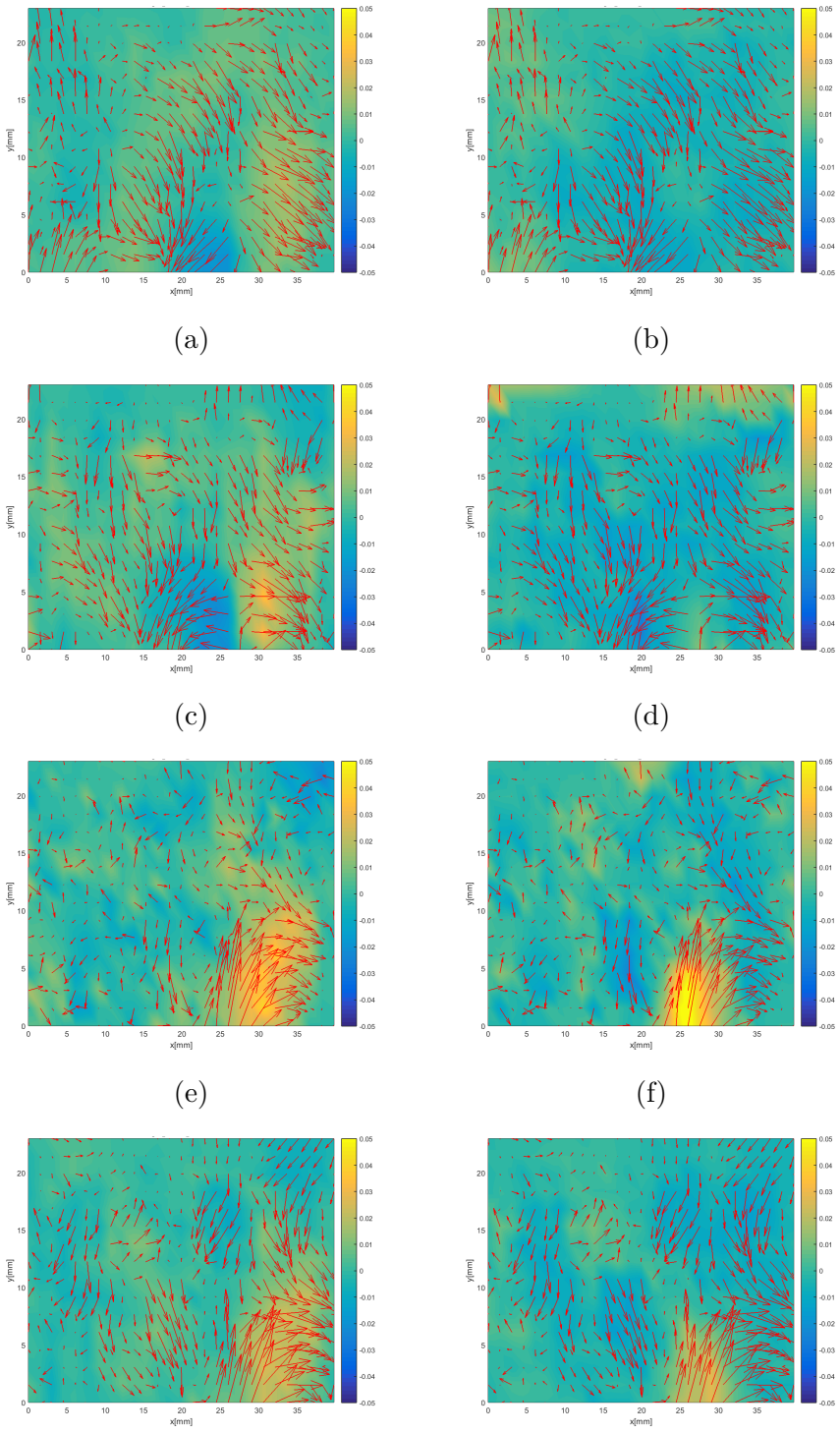
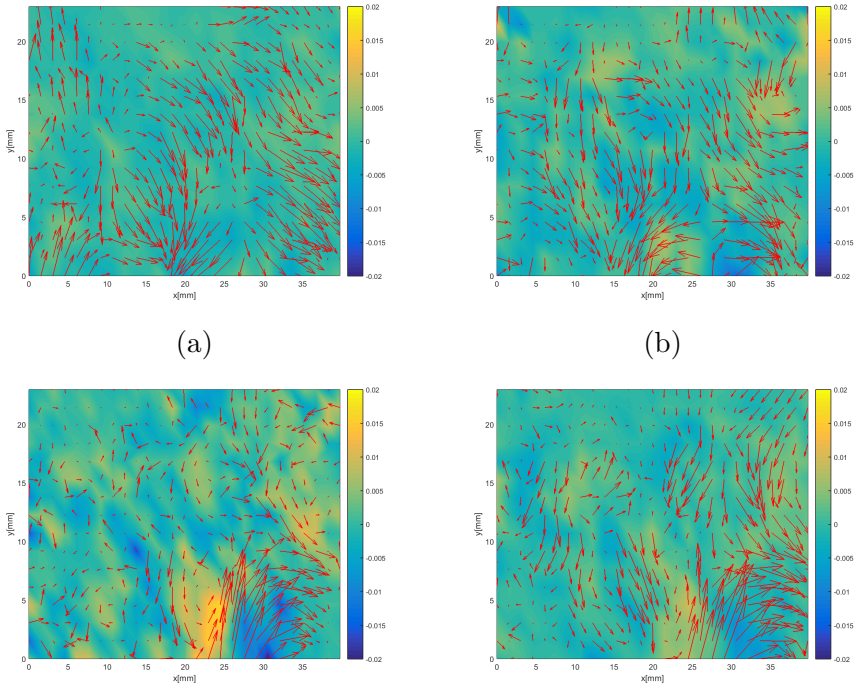


Figure 4.5.6: LED-induced sublimation of dry ice. Snapshots of instantaneous horizontal (left) and vertical (right) velocity. t = 0.0 (a, b), 10.0 (c, d), 20.0 (e, f), 30.0 (g, h) milliseconds.



(a) (b)

(c) (d)

Figure 4.5.7: LED-induced sublimation of dry ice. Snapshots of instantaneous vorticity maps. t = 0.0 (a), 10.0 (b), 20.0 (c), 30.0 (d) milliseconds.

4.6 Summary

Particle image velocimetry was used to quantify the flow expansion produced from: a) ignition of bubbles filled with air-hydrogen and air-butane mixtures and b) sublimation of carbon-dioxide particles. The above phenomena are triggered by focusing a high-power laser beam into a small region - method known as laser energy deposition (LED). This technology has been investigated here for quiescent air and aims at further development where it can be applied to a turbulent boundary layer, in order to disrupt the near-wall cycle through manipulation of hairpin eddies. Moreover, this thechnique can potentially be implemented on aircraft wings for skin friction reduction. Results from measurements presented in this dissertation, encourage further investigation of jets produced through ignition of air-hydrogen bubbles, due to their intensity and small transients. Results are resumed in the following points:

(a) **Ignition of air-hydrogen bubbles can produce jets of intensity potentially in the order of 10 meters per seconds.** These jets can have transient of the order of 2.5 milliseconds from the laser pulse;

(b) **Ignition of air-butane bubbles produces a flame front expanding at about 0.5 meters per second;**

(c) **Sublimation of carbon-dioxide particles can produce jets whose magnitude is of the order of 0.05 meters per second and flow transients roughly equal to 20 milliseconds.** This result might seem not to be relevant, compared to ignition of hydrogen bubbles. However, CO_2 sublimation can be a valid alternative to ignition, since no flammable chemicals

are involved. This can be of interest to better address safety regulations compared to ignition processes.

Although, at this stage of development, this flow actuator cannot fully adhere to aviation safety regulations, its technology is encouraging in order to target hairpin vortices and to interrupt the near-wall cycle. A potential implementation of such a system is commercial aircraft wings in the subsonic regime, as it can certainly be beneficial for turbulent drag reduction.

Chapter 5

Conclusions and future developments

5.1 Concluding remarks

One of the key aspects of this research has been the development of a flow actuator which can potentially be applied for active skin-friction reduction.

We have embarked on a journey to remark the importance of turbulent drag reduction in subsonic aeronautical transportation (Chapt. 1). This concern results from a recent increase of fuel costs and the fact that turbulent skin friction can amount to 45% of the total drag force which aircraft engines must sustain during cruise flight.

In Chapt. 2 we have described the key role of hairpin vortices in the sustenance of the turbulence near-wall cycle, which is responsible of high wall shear stress. This correlation between inner and outer regions has lead us to think about a new concept for flow control where active suppression of hairpin motions can be exploited to disrupt the near-wall cycle and control turbulent drag.

Chapt. 3 and 4 have presented encouraging methodologies to deliver a novel successful strategy for remote flow control. In order to do so, we must be able to:

(a) Identify hairpin vortices from the near-wall region. This requirement is based on the practical idea of a shear stress sensor[1] which can be placed on the leading edge of a wing to read instantaneous maps of velocity fluctuation.

Moreover, since there is evidence in the literature that conglomerates of hairpin loops can flank outer regions of low-momentum fluid (Sect. 2.2.1), image processing and two-dimensional correlation have successfully recognised outer coherent motions by taking into consideration their near-wall imprints. In this perspective, this method can be the ground for active identification of hairpin vortices;

(b) Produce a localised flow perturbation which can disrupt hairpin motions without interfering with the underlying boundary layer. In light of this objective, laser energy deposition (LED) is encouraging, especially when used to trigger the ignition of air-hydrogen bubbles. In fact, PIV measurements led to infer evidence of fluid ejections which can be of the order of 10.0 m/s. Energy deposition can be used to build a flow actuator which can remotely affect the flow field by using directional laser beams that can be adjusted in real time. Such a system (Fig. 4.1.1) does not require to modify the wing aerodynamic shape and is faster than conventional flow actuators, which are affected by flow establishment around

[1] For example, hotfilm flush-mounted sensors (`https://www.dantecdynamics.com/products-and-services/single-sensor-film-probes`).

moving components (e.g. flaps, slats, spoilers).

5.2 Recommendations for future research

In brief, the two methodologies presented in this dissertation have been developed in the perspective of active feed-back control of turbulent skin friction through manipulation of hairpin vortices. Possible developments of this research are proposed below:

1. **The procedure for identification of outer coherent motions based on image processing and pattern recognition (Chapt. 3) can be improved.** In fact, values of parameters for each morphological operation in the sequence described in Sect. 3.2 (e.g. median filter size, area opening cell, etc.) can be calculated through an optimisation cycle by making use of the cross-correlation coefficient for image pairs. In other words, images are compared before and after a morphological operation is performed so that large-scale contours are preserved. In this way, a wider range of applications and flow regimes can effectively be taken in consideration;

2. **Validation and adjustment of the procedure for identification of outer coherent motions (Chapt. 3) through three-dimensional databases.** In this way, hairpin vortices can also be visualised by making use of vortex identification methods, such as swirling strength, λ_2, and Q criteria in order to validate results achieved through image analysis and pattern recognition;

3. **The flow actuator based on laser energy deposition (LED) can be tested in a turbulent flow where hairpins can be simulated artificially (for example by using hemispherical protrusions at the wall).** In this way, the actuators time response can be validated by observing hairpin loops being disrupted while convected downstream;

4. **Finally, a hybrid system making use of both laser energy deposition and image analysis can be tested on a full-scale wing to simulate the actual flow condition experienced by commercial aircraft at cruise flight.** In this experiment, bubbles filled with air-hydrogen mixture can be injected in the flow field. Moreover, algorithms based on the near-wall signal can control the location of the laser focus, which is fundamental to achieve active feed-back control. Arrays of hot-film sensors placed both upstream and downstram of the actuator can measure the wall-normal velocity gradients, hence, determine the shear distributions at the wall. In this way, the dynamic response of the turbulent boundary layer under flow actuation can be estimated, together with the turbulent friction reduction - through disruption of hairpin vortices.

Furthermore, the author would recommend the use of instantaneous PIV to measure the local flow field produced by laser energy deposition. A particular suggestion is to filter all light reflections from laser beams and flames (which is the present study could not be avoided) by using a prescribed filter and fluorescent PIV trackers, so that particles can still be visualised for PIV processing. The above considerations are important to prevent any possible error sources.

Appendices

Appendix A

A.1 Identification of Outer Coherent Motions through Image Processing

A.1.1 Binary Morphological Processing

Binary morphological processing has been applied to two-dimensional maps of stream-wise velocity fluctuations distributed across wall-parallel planes of data. The analysis is performed to smooth contours of large-scale objects while removing smaller scales. To clarify, components resulting from conversion of high and low speed regions of fluid into binary format are named as *objects* or *spots*. The code for image analysis and pattern recognition has been developed in Matlab. The most relevant technical aspects of the code are reported below:

```
1
2           function [outpArr14] =
3           binaryProcess(areaop1,areaop2,
                inputBinMatrix,medfiltpixArr1,...
4           medfiltpixArr2,skelval)
5
```

```
6          %medfiltpixArr1 = size in pixels of the 1
               st applied 2D median filter
7          %medfiltpixArr2 = size in pixels of the 1
               st applied 2D median filter
8          %skelval = skeletisation parameter
9
10         outpArr = medfilt2(inputBinMatrix,
               medfiltpixArr1);
11
12         %Remove white and black spots smaller
               than areaop1
13         outpArr2 = bwareaopen(outpArr,areaop1,8);
14         outpArr3 = imcomplement(outpArr2);
15         outpArr4 = bwareaopen(outpArr3,areaop1,8)
               ;
16         outpArr5 = imcomplement(outpArr4);
17         outpArr6 = bwmorph(outpArr5,'skel',
               skelval);
18         outpArr7 = bwareaopen(outpArr6,areaop1,8)
               ;
19         outpArr8 = bwmorph(outpArr7,'branchpoints
               ');
20
21         %Remove white and black spots smaller
               than areaop1
22         outpArr9 = bwareaopen(outpArr8,areaop1,8)
               ;
```

```
23          outpArr10 = medfilt2(outpArr9,
                medfiltpixArr2);
24          outpArr11 = bwareaopen(outpArr10,areaop2
                ,8);
25          outpArr12 = imcomplement(outpArr11);
26
27          %Remove white and black spots smaller
                than areaop2
28          outpArr13 = bwareaopen(outpArr12,areaop2
                ,8);
29          outpArr14 = imcomplement(outpArr13);
30
31          end
```

As observed above, a function named as *binaryProcess* can perform specific operations, for image analysis and pattern recognition applied to outer coherent motions, which are listed below:

1. Two-dimensional median filter is applied to original fluctuation maps. The size of the filter window is of the order $\lambda_x^+ \times \lambda_z^+ \approx 600 \times 50$;

2. Morphological area opening is implemented to remove both white and black spots, which respectively correspond to negative and positive velocity fluctuations. Objects smaller than 1250 pixels, corresponding to $\lambda_x^+ \times \lambda_z^+ \approx 400 \times 200$, are removed from the image;

3. Morphological skeletonisation and branching have been implemented to reduce the thickness of binary large-scale objects, especially in the viscous sub-layer;

4. Median filtering is applied a second time to finely smooth large-scale objects. For this purpose, a small filter window (15×15 pixels) is used;

5. Morphological area opening is applied a second time to remove objects smaller than 20000 pixels. In fact, at this stage, few large objects are still populating binary images.

The outcome of each operation has been monitored and validated so that the overall image topology is preserved. In this way, large-scale contours can be preserved during image processing to facilitate and optimise the pattern recognition stage.

A.1.2 Identification of Near-wall Regions of Interest (ROI)

This section illustrates a code which has been developed in Matlab to determine near-wall samples for image correlation across wall-parallel planes. In this way, homologous binary objects in the outer region can be determined directly from the viscous sublayer.
The algorithm has made use of the *blob-analysis* toolbox, for which the only input is a binary image.
As a result, some binary contours are identified and characterised on the basis of their morphology and size. This means that contours are classified in terms of perimeter, contour coordinates, centroid, etc. Moreover, each object represent a sub-image, which will be used on the following step, i.e. the image correlation with wall-parallel planes in the logarithmic and outer regions.

```
1 %The BlobAnalysis object computes
    statistics for connected regions in
```

```
2           a binary image;
3           blobAnalysis = vision.BlobAnalysis('
                BoundingBoxOutputPort',...
4           true'AreaOutputPort', true,'
                CentroidOutputPort',...
5           true,'MinimumBlobArea',50);
6
7           %The step method computes and returns
                statistics of the input binary
8           image;
9           [areas,centroids,bbox] = step(
                blobAnalysis,BW);
10
11          % Green boxes drawn around the detected
                regions
12          result = insertShape(BWd,'Rectangle',bbox
                ,'Color','green');
13          result2 = ...
14          insertMarker(result,centroids,'plus','
                Color','red','size',10);
15          numFlows = size(bbox, 1);
16          result2 = insertText(result2, [10
                ...
17          10],numFlows,'BoxOpacity',1,'FontSize'
                ,14);
```

A.1.3 Object Recognition in the Logarithmic and Outer Regions

Object recognition has been performed by using the *normxcorr2* function in Matlab, which can determine the normalised two-dimensional cross correlation between image pairs.

In this case, the image pair is represented by:

(a) **Sub-images in the near-wall regions containing the samples or footprints of outer coherent motions;**

(b) **Wall-parallel planes of binary data in the logarithmic and outer regions.**

A minimum threshold value in the cross-correlation coefficient between image pairs has been set to discard those outer binary objects pairs which are not well-correlated with near-wall samples.

```
1  for i = 1:size(bbox,1)
2  samples{i,1} = imcrop(samplesMatr,bbox(i
       ,:));
3  samples_b{i,1} = samples{i,1};
4  crossc{i,1} = normxcorr2(samples{i,1},
       compareMatr);
5  crossc_max{i,1} = max(crossc{i,1}(:));
6  [ypeak{i,1},xpeak{i,1}] = find(crossc{i
       ,1} == max(crossc{i,1}(:)));
7  yoffSet{i,1} = ypeak{i,1} - size(samples{
       i,1},1);
8  xoffSet{i,1} = xpeak{i,1} - size(samples{
       i,1},2);
```

```
9
10          if crossc_max{i,1} < corrThresh
11                  samples_b{i,1} = [];
12          end
13          end
```

This strategy is tremendously powerful to detect outer coherent motions and eventually hairpin vortices, on the sole basis samples taken in the viscous sub-layer.

References

[Abe et al., 2004] Abe, H., Kawamura, H., and Choi, H. (2004). Very large-scale structures and their effects on the wall shear-stress fluctuations in a turbulent channel flow up to re_τ =640. *Journal of Fluids Engineering*, 126(5):835–843.

[Adelgren, 2003] Adelgren, R. (2003). Localized flow control with energy deposition. Technical report, Graduate School-New Brunswick Rutgers, The State University of New Jersey.

[Adelgren et al., 2005] Adelgren, R., Beutner, T., and Zheltovodov, A. (2005). Control of edney iv interaction by pulsed laser energy deposition. *AIAA*, 43(2).

[Adrian et al., 2000] Adrian, R., Meinhart, C., and Tomkins, C. (2000). Vortex organization in the outer region of the turbulent boundary layer. *Journal of Fluid Mechanics*, 422:1–54. Cambridge University Press.

[Adrian, 2007] Adrian, R. J. (2007). Hairpin vortex organisation in wall turbulence. *Physics of Fluids*, 19.

[Agostini and Leschziner, 2014] Agostini, L. and Leschziner, M. A. (2014). On the influence of outer large-scale structures on the near-wall turbulence in channel flow. *Physics of Fluids*, 26.

[Agostini et al., 2014a] Agostini, L., Touber, E., and Leschziner, M. (2014a). Spanwise oscillatory motion in channel flow: drag reduction mechanisms inferred from dns predicted phase-wise property variations at re=1000. *Journal of Fluid Mechanics*, 743:606–635.

[Agostini et al., 2014b] Agostini, L., Touber, E., and Leschziner, M. (2014b). The turbulence vorticity as a window to the physics of friction-drag reduction by oscillatory wall mmotion. *International Journal of Heat and Fluid Flow.*

[Aubri et al., 1988] Aubri, N., Holmes, P., Lumley, J. L., and Stone, E. (1988). The dynamics of coherent structures in the wall region of a turbulent boundary layer. *Journal of Fluid Mechanics*, 192:115–173.

[Baars et al., 2015] Baars, W. J., Talluru, K. M., Hutchins, N., and Marusic, I. (2015). Wavelets analysis of wall turbulence to study large-scale modulation of small scales. *Experimental Fluids*, 56(188).

[Bandyopadhyay, 1980] Bandyopadhyay, P. (1980). Large structure with a characteristic upstream interface in turbulent boundary layers. *Physics of Fluids*, 23(2326).

[Blackwelder and Eckelmann, 1979] Blackwelder, R. and Eckelmann, H. (1979). Streamwise vortices associated with bursting phenomenon. *Journal of Fluid Mechanics*, 94:577–594.

[Boyle and Thomas, 1988] Boyle, R. and Thomas, R. (1988). *Computer Vision: A First Course*. Blackwell Scientific Publications.

[Choi, 1986] Choi, K.-S. (1986). Drag reduction by manipulation of near-wall turbulence structure. In *Proc. European Meeting on Turbulent Drag Reduction*.

[Choi, 1989] Choi, K. S. (1989). Near-wall structure of a turbulent boundary layer with riblets. *Journal of Fluid Mechanics*, 208:417–458.

[Corino and Brodkey, 1969] Corino, E. and Brodkey, S. (1969). A visual investigation of the wall region in turbulent flow. *J. Fluid Mech.*, 37:1–30.

[Davies, 1990] Davies, E. (1990). *Machine Vision: Theory, Algorithms and Practicalities*. Academic Press.

[Del Alamo and Jimenez, 2003] Del Alamo, J. C. and Jimenez, J. (2003). Spectra of the very large anisotropic scales in turbulent channels. *Physics of Fluids*, 15.

[Dubief and Delcayre, 2000] Dubief, Y. and Delcayre, F. (2000). On coherent-vortex idenfication in turbulence. *Journal of Turbulence*, 1(11).

[Feng et al., 2012] Feng, L. H., Jukes, T. N., Choi, K. S., and Wang, J. J. (2012). Flow control over a naca 0012 airfoil using dielectric-barrier-discharge plasma actuator with a gurney flap. *Exp Fluids*, 52:1533–1546. Springer.

[Frieden, 1976] Frieden, B. (1976). A new restoring algorithm for the preferencial enhancement of edge gradients. *J. Opt. Soc. Amer.*, pages 280–283.

[Ganapathisubramani et al., 2003] Ganapathisubramani, B., Longmire, E. K., and Marusic, I. (2003). Characteristics of vortex packets in turbulent boundary layers. *Journal of Fluid Mechanics*, 478:35–46.

[Ghosh and Mahesh, 2008] Ghosh, S. and Mahesh, K. (2008). Numerical simulation of fluid dynamic effects of laser energy deposition in air. *Journal of Fluid Mechanics*, 605:329–354.

[Glezer and Amitay, 2002] Glezer, A. and Amitay, M. (2002). Synthetic jets. *Annual Review of Fluid Dynamics*, 34:503–529.

[Gonzalez and Woods, 1992] Gonzalez, R. and Woods, R. (1992). *Digital Image Processing*. Addison-Wesley.

[Grant, 1997] Grant, I. (1997). Particle image velocimetry: a review. Technical report, Fluid Loading and Instrumentation Centre, Heriot-Watt University.

[Gupta et al., 1971] Gupta, A. K., Laufer, J., and Kaplan, R. E. (1971). Spatial structure in the viscous sublayer. *Journal of Fluid Mechanics*, 50(493).

[Haralick and Shapiro, 1992] Haralick, R. and Shapiro, L. (1992). *Computer and Robot Vision*. Addison-Wesley.

[Head and Bandyopadhyay, 1981] Head, M. R. and Bandyopadhyay (1981). New aspects of turbulent boundary-layer structure. *Journal Fluid Mechanics*, 107:297–338.

[Hinsch, 1993] Hinsch, K. D. (1993). *Particle Image Velocimetry*, chapter 6. Marcel Dekker Inc.

[Huang et al., 1979] Huang, T., Yang, G., and Tang, G. (1979). A fast two-dimensional median filtering algorithm. *IEEE Transactions on Acoustics Speech and Signal Processing*, ASSP-27.

[Hurst et al., 2014] Hurst, E., Yang, Q., and Chung, Y. (2014). The effect of reynolds number on turbulent drag reduction by streamwise travelling waves. *Journal of Fluid Mechanics*.

[Husssain, 1986] Husssain, A. K. (1986). Coherent structures and turbulence. *Journal of Fluid Mechanics*, 173:303–356.

[Hutchins and Marusic, 2007a] Hutchins, N. and Marusic, I. (2007a). Evidence of very long meandering features in the logarithmic region of turbulent boundary layers. *Journal of Fluid Mechanics*, 579:1–28.

[Hutchins and Marusic, 2007b] Hutchins, N. and Marusic, I. (2007b). Large-scale influences in near-wall turbulence. *Philosophical Transactions of the Royal Society of London A (2007)*, 365:647ï£¡664.

[Hyslip and Vallejo, 1997] Hyslip, J. and Vallejo, L. (1997). Fractal analysis of the roughness and size distributions of granular materials. *Engineering Geology*, pages 231–244.

[Izzo and Coles, 1962] Izzo, W. and Coles, N. (1962). Blood-cell scanner identifies rare-cells. *Electron*, 35:52–55.

[Jeong and Hussain, 1995] Jeong, J. and Hussain, F. (1995). On the identification of a vortex. *Journal of Fluid Mechanics*, 285:69–94.

[Jiang et al., 1998] Jiang, Z., Takayama, K., Moosad, K., Onodera, O., and Sun, M. (1998). Numerical and experimental study of a

micro-blast wave generated by pulsed-laser beam focusing. *Shock Waves*, 8:337:349.

[Jimenez et al., 2004] Jimenez, J., Del Alamo, J., and Flores, O. (2004). The large-scale dynamic of near-wall turbulence. *Journal Fluid Mechanics*, 505:179–199.

[Jimenez and Pinelli, 1999] Jimenez, J. and Pinelli, A. (1999). The autonomous cycle of near-wall turbulence. *Journal of Fluid Mechanics*, 389:335–359.

[Jukes, 2007] Jukes, T. (2007). Wall-normal jet induced from circular dielectric barrier discharge plasma actuators. Progress report, The University of Nottingham.

[Jukes, 2015] Jukes, T. (2015). Smart control of a horizonthal axis wind turbine using dielectric barrier discharge plasma actuators. *Renewable Energy*, 80:644–654.

[Kang et al., 2008] Kang, Y. D., Choi, K. S., and Chun, H. H. (2008). Direct intervention of hairpin structures for turbulent boundary layer control. *Physics of Fluids*, 20(101517).

[Kim and Adrian, 1999] Kim, C. and Adrian, J. (1999). Very large-scale motion in the outer layer. *Physics of Fluids*, 11(2).

[Kim, 1983] Kim, J. (1983). On the structure of wall-bounded turbulent flows. *Physics of Fluids*, 26(2088).

[Kim et al., 1971] Kim, T., Kline, J., and Reynolds, W. (1971). The production of turbulence near a smooth wall in a turbulent boundary layer. *Journal of Fluid Mechanics*, 50.

[Kline et al., 1967] Kline, S., Reynolds, W., Shraub, F., and Runstadler, P. (1967). The structure of turbulent boundary layers. *Jornal of Fluid Mechanics*, 30:741–773.

[Knight and Yan, 2007] Knight, D. and Yan, H. (2007). Fundamental physics and practical applications of electromagnetic local flow control in high speed flows. *Air Force Office of Scientific Research.*

[Kong and Rosenfeld, 1996] Kong, T. and Rosenfeld, A. (1996). *Topological Algorithms for Digital Image Processing.* Elsevier Science Inc.

[Kravchenko et al., 1993] Kravchenko, A. G., Choi, H., and Moin, P. (1993). On the relation of near-wall streamwise vortices to wall skin friction in turbulent boundary layers. *Physics of Fluids*, 5(12):3307–3309.

[Kreplin and Eckelmann, 1979] Kreplin, H. and Eckelmann, H. (1979). Propagation of perturbations in the viscous sublayer and adjacent wall region. *J. Fluid Mech.*, 95:305–322.

[Lam et al., 1992] Lam, L., Lee, S., and Ching, S. (1992). Thinning methodologies - a comprehensive survey. *IEEE Transaction on Pattern Analysis and Machine Intelligence*, 14(9).

[Lee et al., 1974] Lee, M. K., Eckelmann, L. D., and Hanratty, T. J. (1974). Identification of turbulent wall eddies through the phase relation of the components of the fluctuating velocity gradient. *Journal Fluid Mechanics*, 66(17).

[Lighthill, 1963] Lighthill, M. J. (1963). *Laminar Boundary Layers.* Oxford: Clarendon Press.

[Lumley and Blossey, 1998] Lumley, J. and Blossey, P. (1998). Control of turbulence. *Annual Review of Fluid Mechanics*, 30:311–327. University of Nottingham & Malaysia.

[Mandelbrot, 1983] Mandelbrot, B. B. (1983). *The fractal geometry of nature*. Macmillan.

[Mathis et al., 2009] Mathis, R., Hutchins, N., and Marusic, I. (2009). Large-scale amplitude modulation of the small-scale structures in turbulent boundary layers. *J. Fluid Mech.*, 628:311–337.

[Mathis et al., 2011a] Mathis, R., Hutchins, N., and Marusic, I. (2011a). A predictive inner-outer model for streamwise turbulence statistics in wall-bounded flows. *Journal of Fluid Mechanics*, 681:537–566.

[Mathis et al., 2013] Mathis, R., Marusic, I., Chernyshenko, S. I., and Hutchins, N. (2013). Estimating wall-shear stress fluctuations given an outer region input. *Journal of Fluid Mechanics*, vol. 715:pp. 163–180. Cambridge University Press 2013.

[Mathis et al., 2011b] Mathis, R., Marusic, I., Hutchins, N., and Sreenivasan, K. (2011b). The relationship between the velocity skewness and the amplitude modulation of the small scale by the large scale in turbulent boundary layers. *Physics of Fluids*, 23.

[McLachlan, 1988] McLachlan, G. (1988). *Mixture Models*. Marcel Dekker Inc.

[Morrison, 2007] Morrison, J. (2007). The interaction between inner and outer regions of turbulent wall-bounded flow. *Philosophical Transactions of the Royal Society*, 365:683ï£¡698.

[Morsy et al., 1999] Morsy, M., Ko, Y., and Chung, S. (1999). Laser-induced ignition using a conical cavity in ch4ï£¡air mixtures. Technical report, School of Mechanical and Aerospace Engineering, Seoul National University, Seoul 151-742, Korea.

[Nakagawa and Nezu, 1981] Nakagawa, H. and Nezu, I. (1981). Structure of space-time correlations of bursting phenomena in an open-channel flow. *Journal of Fluid Mechanics*, 104(1).

[Ochiai et al., 2016] Ochiai, Y., Kumagai, K., Hoshi, T., Rekimoto, J., Hasegawa, S., and Hayasaki, Y. (2016). Fairy lights in femtoseconds: Aerial and volumetric graphics rendered by focused femtosecond laser combined with computational holographic fields. *ACM Transactions on Graphics (TOG)*, 35(17).

[Oldaker and Tiederman, 1977] Oldaker, D. K. and Tiederman, W. G. (1977). Spatial structure of the viscous sublayer in drag-reducing channel flows. *Physics of Fluids*, 20.

[Orlandi and Jimenez, 1994] Orlandi, J. and Jimenez, P. (1994). On the generation of turbulent wall friction. *Physics of Fluids*, 634(6).

[Pratt, 1978] Pratt, W. (1978). *Digital Image Processing*. Wiley, New York.

[Pratt, 1975] Pratt, W. K. (1975). Median filtering. *Image Processing*.

[Praturi and Brodkey, 1978] Praturi, A. K. and Brodkey, R. S. (1978). A stereoscopic visual study of coherent structures in turbulent shear flow. *Journal of Fluid Mechanics*, 89(02):251–272.

[Preston, 1961] Preston, K. (1961). The cellscan system - a leucocyte patterns analyser. *Proc. West Joint Comput. Conf.*, pages 173–183.

[Reynolds, 2000] Reynolds, D. (2000). *Gaussian Mixture Models*. Lexington.

[Reynolds et al., 2000] Reynolds, D., Quatieri, T., and Dunn, R. (2000). Speaker verification using adapted gaussian mixture models. *Digital Signal Processing*, 10(1):19–41.

[Reynolds and Rose, 1995] Reynolds, D. and Rose, R. (1995). Robust text-independent speaker identification using gaussian mixture models. *IEEE Transactions on Acoustics Speech and Signal Processing*, 3(1):72–83.

[Robinson, 1991] Robinson, S. (1991). Coherent motions in the turbulent boundary layer. *Annual Review of Fluid Mechanics*, 23:601–639.

[Runstadler et al., 1963] Runstadler, P. W., Kline, S. J., and Reynolds, W. C. (1963). An experimental investigation of the flow structure of the turbulent boundary layer. MD 8, Department of Mechanical Engineering, Stanford University.

[Saito et al., 2008] Saito, H., Kimurab, H., Shimadac, S., Naemurad, T., Kayaharae, J., Jarusirisawad, S., Nozick, V., Ishikawa, H., Murakami, T., Aoki, J., Asano, A., Kimura, T., Kakehata, M., Sasaki, F., Yashiro, H., Mori, M., Torizuka, K., and Inod, K. (2008). Laser-plasma scanning 3d display for putting digital contents in free space. *Proc. SPIE, Stereoscopic Displays and Applications XIX*, 6803.

[Santhanakrishnan and Jacob, 2007] Santhanakrishnan, A. and Jacob, J. (2007). Flow control with plasma synthetic jet actuators. *Journal of Physics*, Applied Physics, Institute of Physics Publishing.

[Schoppa and Hussain, 2002] Schoppa, W. and Hussain, F. (2002). Coherent structure generation in near-wall turbulence. *Journal of Fluid Mechanics*, 453:57–108.

[Schraub and Kline, 1965] Schraub, F. A. and Kline, S. J. (1965). A study of the structure of the turbulent boundary layer with and without longitudinal pressure gradients. Technical Report MD-12, Dept. Mech. Eng. Stanford University.

[Schulein and Zheltovodov., 2008] Schulein, E. and Zheltovodov., H. (2008). Experimental and numerical study of shock-wave transformation by laser-induced energy deposition. In *International Conference on Methods of Aerophysical Research (ICMAR)*.

[Smith, 1984] Smith, C. R. (1984). A synthesized model of the near-wall behavior in turbulent boundary layers. Technical report, Lehigh University of Bethlem - Department of Mechanical Engineering and Mechanics.

[Smith and Metzler, 1983] Smith, R. and Metzler, S. (1983). The characteristics of low-speed streaks in the near-wall region of a turbulent boundary layer. *Journal of Fluid Mechanics*, 129:27–54.

[Spur et al., 1999] Spur, G., Uhlmann, E., and Elbing, F. (1999). Dry-ice blasting for cleaning: process, optimisation, and application. *Wear*, pages 402–411.

[Stamhuis, 2006] Stamhuis, E. J. (2006). Basics and principles of particle image velocimetry (piv) for mapping biogenic and biologically relevant flows. *Aquatic Ecology*, 40:463–479.

[Sun and Neuvo, 1992] Sun, T. and Neuvo, Y. (1992). Detail-preserving median based filters in image processing. *Pattern Recognition Letters*, 15:341–347.

[Theodorsen, 1952] Theodorsen, T. (1952). Mechanism of turbulence. In *Proceedings of the Second Midwestern Conference on Fluid Mechanics*, volume 1719. Ohio State University.

[Tilma, 2006] Tilma, T. (2006). Aist develops laser-based 3d display system. Technical report, National Institute of Advanced Industrial Science and Technology.

[Tomkins and Adrian, 2003] Tomkins, C. and Adrian, R. (2003). Spanwise structure and scale growth in turbulent boundary layers. *Journal Fluid Mechanics*, 490:37–74.

[Uhlmann et al., 2006] Uhlmann, E., Hollan, R., Veit, R., and Mernissi, A. E. (2006). A laser assisted dry ice blasting approach for surface cleaning. *LCE*, pages 471–476.

[Vincent, 1993] Vincent, L. (1993). Grayscale area openings and closings, their efficient implementation and applications. *Proc EURASIP Workshop on Mathematical Morphology and its applications to Signal Processings*.

[Vincent, 1994] Vincent, L. (1994). Morphological area openings and closings for grey-scale images. *NATO ASI Series*, 126:197–208.

[Wallace et al., 1972] Wallace, J., Eckelmann, H., and Brodkey, S. (1972). The wall region in turbulent shear flows. *J. Fluid Mech.*, 54:39–48.

[Willmarth and Tu, 1967] Willmarth, W. W. and Tu, B. J. (1967). Structure of turbulence in the boundary layer near the wall. *Physics of Fluids*, pages 134–137.

[Zhou et al., 1996] Zhou, J., Adrian, R. J., and Balachandar, S. (1996). Autogeneration of near-wall vortical structures in channel flow. *Physics of Fluids*, 8(288).

[Zhou et al., 1999] Zhou, J., Adrian, R. J., Balachandar, S., and Kendall, T. M. (1999). Mechanisms for generating coherent packets of hairpin vortices in channel flow. *Journal of Fluid Mechanics*, 387:353–396.